

UNITED STATES AIR FORCE
SUMMER RESEARCH PROGRAM -- 1999
SUMMER RESEARCH EXTENSION PROGRAM FINAL REPORTS

VOLUME 2
PHILLIPS LABORATORY

RESEARCH & DEVELOPMENT LABORATORIES
5800 Uplander Way
Culver City, CA 90220-6608

Program Director, RDL
Gary Moore

Program Manager, AFOSR
Colonel Cervený

Program Manager, RDL
Scott Licoscós

Program Administrator, RDL
Johnetta Thompson

Program Administrator, RDL
Rebecca Kelly-Clemmons

Submitted to:

AIR FORCE OFFICE OF SCIENTIFIC RESEARCH
Bolling Air Force Base
Washington, D.C.
December 1999

20010319 023

AQM01-06-1178

PREFACE

This volume is part of a four-volume set that summarizes the research of participants in the 1999 AFOSR Summer Research Extension Program (SREP). The current volume, Volume 1 of 4, presents the final reports of SREP participants at Armstrong Laboratory.

Reports presented in this volume are arranged alphabetically by author and are numbered consecutively -- e.g., 1-1, 1-2, 1-3; 2-1, 2-2, 2-3, with each series of reports preceded by a 35 page management summary. Reports in the four-volume set are organized as follows:

VOLUME	TITLE
1	Armstrong Research Laboratory
2	Phillips Research Laboratory
3	Rome Research Laboratory
4	Wright Research Laboratory

REPORT DOCUMENTATION PAGE

Public reporting burden for this collection of information is estimated to average 1 hour per response, including the time for reviewing instructions, searching existing data sources, gathering the data, reviewing the collection of information, Send comments regarding this burden estimate or any other aspect of this collection of information, including suggestions for reducing the burden, to Washington Headquarters Services, Directorate for Information Operations and Reports, 1215 Jefferson Davis Highway, Suite 1204, Arlington, VA 22202-4302 and to the Office of Management and Budget, Paperwork Project, Washington, DC 20503.

AFRL-SR-BL-TR-00-

ing and reviewing
for information

1. AGENCY USE ONLY (Leave blank)		2. REPORT DATE December, 1999		3. R 0720	
4. TITLE AND SUBTITLE 1999 Summer Research Program (SRP), Summer Research Extension Program (SREP), Final Report, Volume 2, Phillips Laboratory				5. FUNDING NUMBERS F49620-93-C-0063	
6. AUTHOR(S) Gary Moore					
7. PERFORMING ORGANIZATION NAME(S) AND ADDRESS(ES) Research & Development Laboratories (RDL) 5800 Uplander Way Culver City, CA 90230-6608				8. PERFORMING ORGANIZATION REPORT NUMBER	
9. SPONSORING/MONITORING AGENCY NAME(S) AND ADDRESS(ES) Air Force Office of Scientific Research (AFOSR) 801 N. Randolph St. Arlington, VA 22203-1977				10. SPONSORING/MONITORING AGENCY REPORT NUMBER	
11. SUPPLEMENTARY NOTES					
12a. DISTRIBUTION AVAILABILITY STATEMENT Approved for Public Release				12b. DISTRIBUTION CODE	
13. ABSTRACT (Maximum 200 words) The United States Air Force Summer Research Program (SRP) is designed to introduce university, college, and technical institute faculty members to Air Force research. This is accomplished by the faculty members, graduate students, and high school students being selected on a nationally advertised competitive basis during the summer intersession period to perform research at Air Force Research Laboratory (AFRL) Technical Directorates and Air Force Air Logistics Centers (ALC). AFOSR also offers its research associates (faculty only) an opportunity, under the Summer Research Extension Program (SREP), to continue their AFOSR-sponsored research at their home institutions through the award of research grants. This volume consists of a listing of the participants for the SREP and the technical report from each participant working at the AF Phillips Laboratory.					
14. SUBJECT TERMS Air Force Research, Air Force, Engineering, Laboratories, Reports, Summer, Universities, Faculty, Graduate Student, High School Student				15. NUMBER OF PAGES	
				16. PRICE CODE	
17. SECURITY CLASSIFICATION OF REPORT Unclassified	18. SECURITY CLASSIFICATION OF THIS PAGE Unclassified	19. SECURITY CLASSIFICATION OF ABSTRACT Unclassified	20. LIMITATION OF ABSTRACT UL		

GENERAL INSTRUCTIONS FOR COMPLETING SF 298

The Report Documentation Page (RDP) is used in announcing and cataloging reports. It is important that this information be consistent with the rest of the report, particularly the cover and title page. Instructions for filling in each block of the form follow. It is important to *stay within the lines* to meet *optical scanning requirements*.

Block 1. Agency Use Only (Leave blank).

Block 2. Report Date. Full publication date including day, month, and year, if available (e.g. 1 Jan 88). Must cite at least the year.

Block 3. Type of Report and Dates Covered. State whether report is interim, final, etc. If applicable, enter inclusive report dates (e.g. 10 Jun 87 - 30 Jun 88).

Block 4. Title and Subtitle. A title is taken from the part of the report that provides the most meaningful and complete information. When a report is prepared in more than one volume, repeat the primary title, add volume number, and include subtitle for the specific volume. On classified documents enter the title classification in parentheses.

Block 5. Funding Numbers. To include contract and grant numbers; may include program element number(s), project number(s), task number(s), and work unit number(s). Use the following labels:

C - Contract	PR - Project
G - Grant	TA - Task
PE - Program Element	WU - Work Unit Accession No.

Block 6. Author(s). Name(s) of person(s) responsible for writing the report, performing the research, or credited with the content of the report. If editor or compiler, this should follow the name(s).

Block 7. Performing Organization Name(s) and Address(es). Self-explanatory.

Block 8. Performing Organization Report Number. Enter the unique alphanumeric report number(s) assigned by the organization performing the report.

Block 9. Sponsoring/Monitoring Agency Name(s) and Address(es). Self-explanatory.

Block 10. Sponsoring/Monitoring Agency Report Number. (If known)

Block 11. Supplementary Notes. Enter information not included elsewhere such as: Prepared in cooperation with....; Trans. of....; To be published in.... When a report is revised, include a statement whether the new report supersedes or supplements the older report.

Block 12a. Distribution/Availability Statement. Denotes public availability or limitations. Cite any availability to the public. Enter additional limitations or special markings in all capitals (e.g. NOFORN, REL, ITAR).

DOD - See DoDD 5230.24, "Distribution Statements on Technical Documents."

DOE - See authorities.

NASA - See Handbook NHB 2200.2.

NTIS - Leave blank.

Block 12b. Distribution Code.

DOD - Leave blank.

DOE - Enter DOE distribution categories from the Standard Distribution for Unclassified Scientific and Technical Reports.

Leave blank.

NASA - Leave blank.

NTIS -

Block 13. Abstract. Include a brief (*Maximum 200 words*) factual summary of the most significant information contained in the report.

Block 14. Subject Terms. Keywords or phrases identifying major subjects in the report.

Block 15. Number of Pages. Enter the total number of pages.

Block 16. Price Code. Enter appropriate price code (*NTIS only*).

Blocks 17. - 19. Security Classifications. Self-explanatory. Enter U.S. Security Classification in accordance with U.S. Security Regulations (i.e., UNCLASSIFIED). If form contains classified information, stamp classification on the top and bottom of the page.

Block 20. Limitation of Abstract. This block must be completed to assign a limitation to the abstract. Enter either UL (unlimited) or SAR (same as report). An entry in this block is necessary if the abstract is to be limited. If blank, the abstract is assumed to be unlimited.

1999 SREP Final Technical Report Table of Contents

Armstrong Research Laboratory

Volume 1

	Principle Investigator	Report Title University/Institution	Laboratory & Directorate
1	Dr. Kenneth Graetz	Conflict Resolution in Distributed Meetings:Using Collaboration Technology to Support Battle Staff University of Dayton	AFRL/HEN
2	Dr. Nadini Kannan	Altitude Decompression Sickness: Modeling and Prediction University of Texas at San Antonio	AFRL/HEPR
3	Ms. Vanessa Le	A Study on Stress-Induced Alterations In Blood-BrainBarrier Permeability to Pyridostigmine University of Texas at Austin	AFRL/HEDB
4	Dr. Ramaswamy Ramesh	Modeling and Analysis of DMT Systems: Training Effectiveness, Costs, Resource Management and Acquisition Strategies Research Foundation of SUNY	AFRL/HEA

1999 SREP Final Technical Report Table of Contents

Phillips Research Laboratory

Volume 2

	Principle Investigator	Report Title University/Institution	Laboratory & Directorate
1	Dr. Gurnam Gill	Adaptive signal Processing and its Applications in Space Space based Radar Naval Postgraduate School	AFRL/VSSS
2	Dr. Robert Hinde	Dopant-Induced Infrared Activity in Solid Hydrogen An AB Initio and Quantum Monte Carlo Study University of Tennessee	AFRL/PRSP
3	Dr. Brian Jeffs	Algebraic Methods for Improved Blind Restoration of Adaptive Optics Images of Space Objects Brigham Young University	AFRL/DEHP
4	Dr. Donald Leo	Self-Sensing acoustic Sources For Interior Noise Control in Payload Fairings University of Toledo	AFRL/VSDV
5	Dr. Arfin Lodhi	Investigation into Time-Dependent Power Loses from AMTEC Components Texas Tech University	AFRL/VSDV
6	Dr. John McHugh	Atmospheric Gravity Waves Near the Tropopause University of New Mexico	AFRL/ VSBC
7	Dr. Stanly Steinberg	Lie-Algebraic representations of Product Integrals of Variable Matrices University of New Mexico	AFRL/DEOB
8	Mr. Kenneth Stephens II	Simulation of a Magnetized Target Fusion Concept Using MACH 2 University of North Texas	AFRL/VSDV

1999 SREP Final Technical Report Table of Contents

Rome Research Laboratory

Volume 3

Principle Investigator	Report Title University/Institution	Laboratory & Directorate
1 Dr. Ercument Arvas	Realization of Low Noise MMIC Amplifier as a Microwave -to Optics Link for Radar Syracuse University	AFRL/SNDR
2 Dr. Kaliappan Gopalan	Detection of Acoustic Correlates of Stress from Modulation Characteristics Purdue Research Foundation	AFRL/IFEC
3 Dr. Donald Hung	An Investigation on Accelerating the Ray-Tracing Computations Washington State University	AFRL/IFSA
4 Dr. Adam Lutoborski	Transform Methods for Watermarking Digital Images Syracuse University	AFRL/IFEC
5 Dr. Brajendra Panda	Implementation of Petri Nets Based Multi-source Attack Detection Model University of North Dakota	AFRL/IFGB
6 Dr. Jerry Potter	Algorithms for Data Intensive Knowledge Discovery Kent State University	AFRL/IFGA
7 Dr. Shambhu Upadhyaya	A Distributed concurrent Intrusion Detection and Recovery Scheme based on Assertions SUNY Buffalo	AFRL/IFGA

1999 SREP Final Technical Report Table of Contents

Wright Research Laboratory

Volume 4

Principle Investigator	Report Title University/Institution	Laboratory & Directorate
1 Dr. Farid Ahmed	Image Quality Assessment for ART Applications Using Multiresolutional Information Metrics Pennsylvania State University, Erie	AFRL/SNAT
2 Dr. Gregory Buck	Acoustic Disturbance Source Modeling and Development for Hypersonic Receptivity South Dakota School of Mines	AFRL/VAAA
3 Dr. Kevin Belfield	Synthesis of New Two-Photon Absorbing Dyes, Monomers and Polymers University of Central Florida	AFRL/ML
4 Dr. Patrick Gilcrease	Biocatalysis of Biphenyl and Diphenylacetylene in an Aqueous Organic Biphase Reaction System University of Wyoming	AFRL/MLQ
5 Dr. Jeffrey Johnson	Incorporating Fixed, Adaptive, and Learning Controllers to the Flight Control University of Toledo	AFRL/VACC
6 Dr. Vikram Kapila	Dynamics and control of Spacecraft Formation Flying Polytechnic Institute of New York	AFRL/VACC
7 Dr. Kenneth Kihm	Micro-Scale Flow Field Measurement of the Thin Meniscus of Capillary-Driven Heat Exchanger Devices Using MFW Texas A & M University	AFRL/VAVE
8 Dr. Rongxing Li	Uncertainty Modeling of Target Locations From Multiplatform and Multisensor Data Ohio State	AFRL/SNAR
9 Dr. Chun-Shin Lin	Sensor Fusion w/Passive Millimeter Wave & Laser Radar for Target Detection University of Missouri –	AFRL/MNGS
10 Dr. Chaoqun Liu	Boundary Conditions in Curvilinear Coordinates for Direct Numerical Simulation of Turbulent Flow Louisiana Tech University	AFRL/VAAA

1999 SREP Final Technical Report Table of Contents

Wright Research Laboratory

Volume 4, continued

	Principle Investigator	Report Title University/Institution	Laboratory & Directorate
11	Dr. Carl Mungan	Infrared Spectropolarimetric Directional Reflectance and Emissivity of Metal Surfaces University of Florida	AFRL/MNGS
12	Dr. Amod Ogale	Structural Changes in Mesophase Pitch-Based Carbon Fibers: In SITU & ES SITU Measurements Clemson University	AFRL/MLBC
13	Mr. Ramana Pidaparti	Benchmarking Aerodynamic Panel Methods for Flight Loads in Multidisciplinary Optimization Indiana University	AFRL/VAS
14	Dr. Stephen Sadow	Silicon Carbide Implant Activation & Surface preparation Investigation Mississippi State University	AFRL/PRPE
15	Dr. Paavo Sepri	Computational Study of Unsteady Flow Interactions Between Turbine Blades, Cylinder Wakes, and coolant Injection Florida Institute of Technology	AFRL/PRTT
16	Dr. Hongchi Shi	Developing an efficient Algorithm for Routing Processors of the VGI Parallel Computer for Signal Processing Applications University of Missouri - Columbia	AFRL/MNGI
17	Dr. Mehrdad Soumekh	Signal and Image Processing for FOPEN/GPEN SAR SUNY Buffalo	AFRL/SNRT
18	Mr. Craig Riviello	In-Situ Synthesis of Discontinuously Reinforced Titanium alloy CompoLaboratorys Via Blended Elemental Powder Metallurgy Processing Wright State University	AFRL/MLLM

1999 SUMMER RESEARCH EXTENSION PROGRAM (SREP) MANAGEMENT REPORT

1.0 BACKGROUND

Under the provisions of Air Force Office of Scientific Research (AFOSR) contract F49620-90-C-0076, September 1990, Research & Development Laboratories (RDL), an 8(a) contractor in Culver City, CA, manages AFOSR's Summer Research Program. This report is issued in partial fulfillment of that contract (CLIN 0003AC).

The Summer Research Extension Program (SREP) is one of four programs AFOSR manages under the Summer Research Program. The Summer Faculty Research Program (SFRP) and the Graduate Student Research Program (GSRP) place college-level research associates in Air Force research laboratories around the United States for 8 to 12 weeks of research with Air Force scientists. The High School Apprenticeship Program (HSAP) is the fourth element of the Summer Research Program, allowing promising mathematics and science students to spend two months of their summer vacations working at Air Force laboratories within commuting distance from their homes.

SFRP associates and exceptional GSRP associates are encouraged, at the end of their summer tours, to write proposals to extend their summer research during the following calendar year at their home institutions. AFOSR provides funds adequate to pay for SREP subcontracts. In addition, AFOSR has traditionally provided further funding, when available, to pay for additional SREP proposals, including those submitted by associates from Historically Black Colleges and Universities (HBCUs) and Minority Institutions (MIs). Finally, laboratories may transfer internal funds to AFOSR to fund additional SREPs. Ultimately the laboratories inform RDL of their SREP choices, RDL gets AFOSR approval, and RDL forwards a subcontract to the institution where the SREP associate is employed. The subcontract (see Appendix 1 for a sample) cites the SREP associate as the principal investigator and requires submission of a report at the end of the subcontract period.

Institutions are encouraged to share costs of the SREP research, and many do so. The most common cost-sharing arrangement is reduction in the overhead, fringes, or administrative charges institutions would normally add on to the principal investigator's or research associate's labor. Some institutions also provide other support (e.g., computer run time, administrative assistance, facilities and equipment or research assistants) at reduced or no cost.

When RDL receives the signed subcontract, we fund the effort initially by providing 90% of the subcontract amount to the institution (normally \$18,000 for a \$20,000 SREP). When we receive the end-of-research report, we evaluate it administratively and send a copy to the laboratory for a technical evaluation. When the laboratory notifies us the SREP report is acceptable, we release the remaining funds to the institution.

2.0 THE 1999 SREP PROGRAM

SELECTION DATA: A total of 381 faculty members (SFRP Associates) and 130 graduate students (GSRP associates) applied to participate in the 1998 Summer Research Program. From these applicants 85 SFRPs and 40 GSRPs were selected. The education level of those selected was as follows:

1998 SRP Associates, by Degree			
SFRP		GSRP	
PHD	MS	MS	BS
83	1	3	19

Of the participants in the 1998 Summer Research Program 65 percent of SFRPs and 20 percent of GSRPs submitted proposals for the SREP. Fifty-four proposals from SFRPs and eleven from GSRPs were selected for funding, which equates to a selection rate of 65% of the SFRP proposals and of 20% for GSRP proposals.

1999 SREP: Proposals Submitted vs. Proposals Selected			
	Summer 1998 Participants	Submitted SREP Proposals	SREPs Funded
SFRP	85	54	34
GSRP	40	11	2
TOTAL	125	65	36

The funding was provided as follows:

Contractual slots funded by AFOSR	36
Laboratory funded	<u>0</u>
Total	36

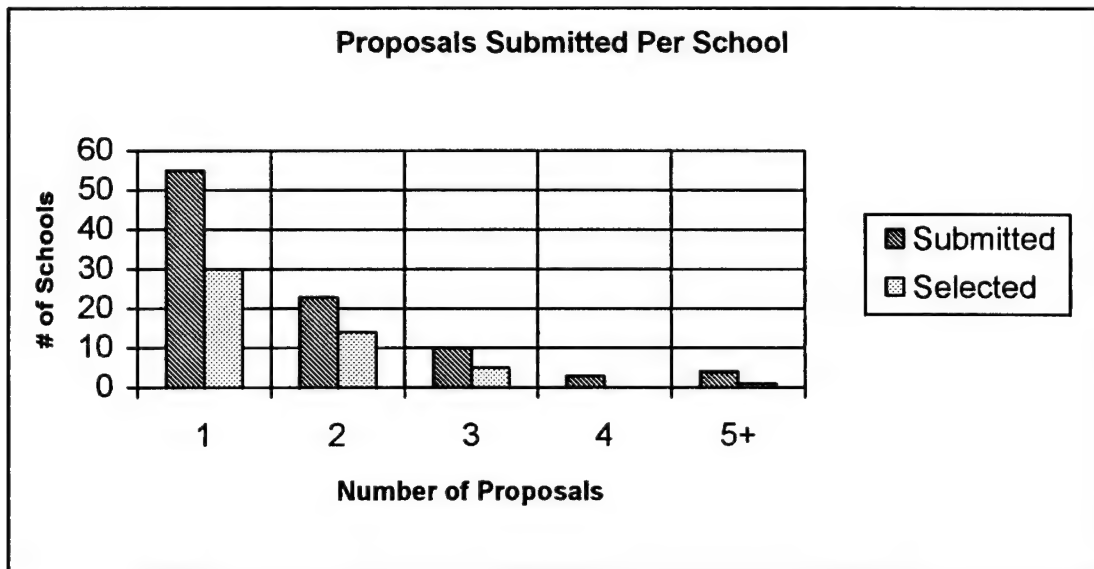
Four HBCU/MI associates from the 1998 summer program submitted SREP proposals; four were selected (none were lab-funded; all were funded by additional AFOSR funds).

Proposals Submitted and Selected, by Laboratory		
	Applied	Selected
Armstrong Research Site	15	3
Air Logistic Centers	1	0
Arnold Engineering Development Center	1	0
Phillips Research Site	10	8
Rome Research Site	12	7
Wilford Hall Medical Center	1	0
Wright Research Site	25	18
TOTAL	65	36

The 212 1998 Summer Research Program participants represented 60 institutions.

Institutions Represented on the 1998 SRP and 1999 SREP		
Number of schools Represented in the Summer 98 Program	Number of schools represented in submitted proposals	Number of schools represented in Funded Proposals
60	36	29

Thirty schools had more than one participant submitting proposals.



The selection rate for the 60 schools submitting 1 proposal (68%) was better than those submitting 2 proposals (61%), 3 proposals (50%), 4 proposals (0%) or 5+ proposals (25%). The 4 schools that submitted 5+ proposals accounted for 30 (15%) of the 65 proposals submitted.

Of the 65 proposals submitted, 35 offered institution cost sharing. Of the funded proposals which offered cost sharing, the minimum cost share was \$1274.00, the maximum was \$38,000.00 with an average cost share of \$12,307.86.

Proposals and Institution Cost Sharing		
	Proposals Submitted	Proposals Funded
With cost sharing	35	30
Without cost sharing	30	6
Total	65	36

The SREP participants were residents of 31 different states. Number of states represented at each laboratory were:

States Represented, by Proposals Submitted/Selected per Laboratory		
	Proposals Submitted	Proposals Funded
Armstrong Research Laboratory	15	3
Air Logistic Centers	1	0
Arnold Engineering Development Center	1	0
Phillips Research Laboratory	10	8
Rome Research Laboratory	12	7
Wilford Hall Medical Center	1	0
Wright Research Laboratory	25	18

Six of the 1999 SREP Principal Investigators also participated in the 1998 SREP.

ADMINISTRATIVE EVALUATION: The administrative quality of the SREP associates' final reports was satisfactory. Most complied with the formatting and other instructions provided to them by RDL. Thirty-six final reports have been received and are included in this report. The subcontracts were funded by \$897,309.00 of Air Force money. Institution cost sharing totaled \$356,928.00.

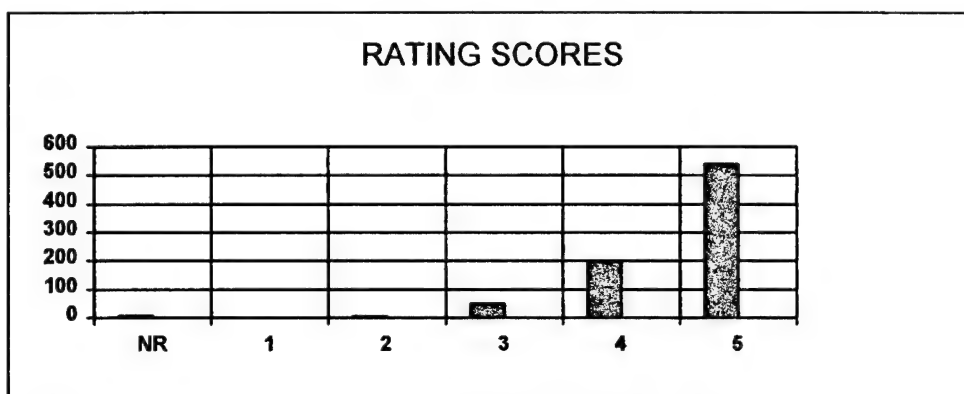
TECHNICAL EVALUATION: The form used for the technical evaluation is provided as Appendix 2. Thirty-two evaluation reports were received. Participants by laboratory versus evaluations submitted is shown below:

	Participants	Evaluations	Percent
Armstrong Laboratory	3	2	95.2
Phillips Laboratory	8	8	100
Rome Laboratory	7	7	100
Wright Laboratory	18	15	91.9
Total	36	32	95.0

Notes:

- 1: Research on four of the final reports was incomplete as of press time so there aren't any technical evaluations on them to process, yet. Percent complete is based upon 20/21 = 95.2%

PROGRAM EVALUATION: Each laboratory focal point evaluated ten areas (see Appendix 2) with a rating from one (lowest) to five (highest). The distribution of ratings was as follows:

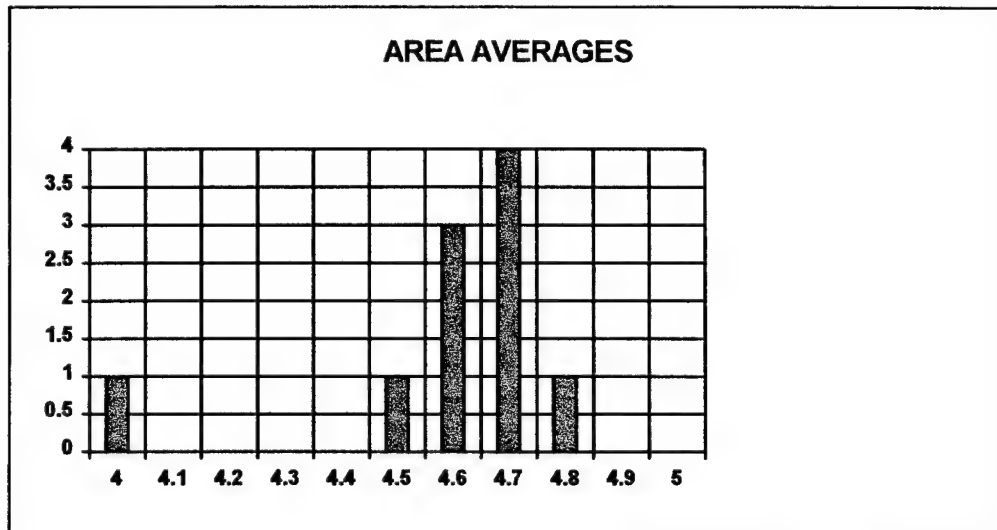


Rating	Not Rated	1	2	3	4	5
# Responses	7	1	7	62 (6%)	226 (25%)	617 (67%)

The 8 low ratings (one 1 and seven 2's) were for question 5 (one 2) "The USAF should continue to pursue the research in this SREP report" and question 10 (one 1 and six 2's) "The one-year period for complete SREP research is about right", in addition over 30% of the threes (20 of 62) were for question ten. The average rating by question was:

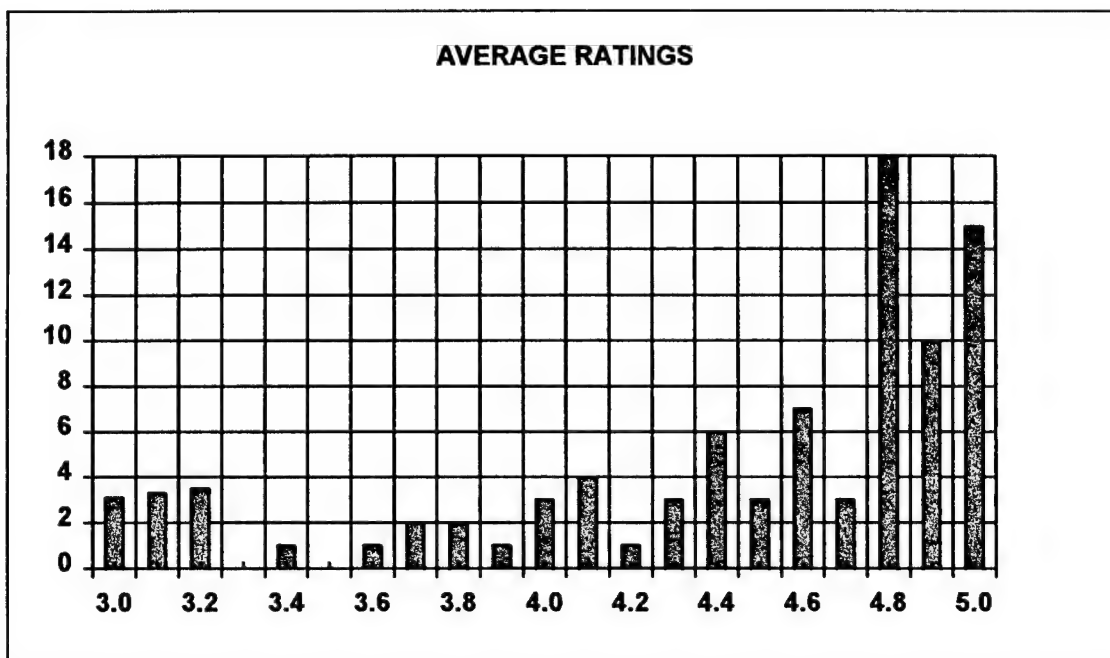
Question	1	2	3	4	5	6	7	8	9	10
Average	4.6	4.6	4.7	4.7	4.6	4.7	4.8	4.5	4.6	4.0

The distribution of the averages was:



Area 10 “the one-year period for complete SREP research is about right” had the lowest average rating (4.1). The overall average across all factors was 4.6 with a small sample standard deviation of 0.2. The average rating for area 10 (4.1) is approximately three sigma lower than the overall average (4.6) indicating that a significant number of the evaluators feel that a period of other than one year should be available for complete SREP research.

The average ratings ranged from 3.4 to 5.0. The overall average for those reports that were evaluated was 4.6. Since the distribution of the ratings is not a normal distribution the average of 4.6 is misleading. In fact over half of the reports received an average rating of 4.8 or higher. The distribution of the average report ratings is as shown:



It is clear from the high ratings that the laboratories place a high value on AFOSR's Summer Research Extension Programs.

3.0 SUBCONTRACTS SUMMARY

Table 1 provides a summary of the SREP subcontracts. The individual reports are published in volumes as shown:

<u>Laboratory</u>	<u>Volume</u>
Armstrong Research Laboratory	1
Phillips Research Laboratory	2
Rome Research Laboratory	3
Wright Research Laboratory	4

SREP SUB-CONTRACT DATA

Report Author Author's University	Author's Degree	Sponsoring Lab	Performance Period	Contract Amount	Univ. Cost Share
Graetz , Kenneth Department of Psychology University of Dayton, Dayton, OH	PhD 99-0803	AL/CF	01/01/99 12/31/99	\$24983.00	\$0.00
			Conflict resolution in distributed Meeting1; Using Collaboration Technology to		
Kannan , Nandini Statistics Univ of Texas at San Antonio, San Antonio, TX	PhD 99-0804	AL/CF	01/01/98 12/31/98	\$22492.00	\$4478.00
			Altitude decompression Sickness: Modeling and Prediction		
Ramesh , Ramaswamy Magement Science/Systems Research Foundation of SUNY, Buffalo, NY	PhD 99-0802	AL/CF	01/01/99 12/31/99	\$24979.00	\$0.00
			Modeling and Analsis of DMT Systems: Training Effectiveness, Costs, Resource Ma		
Le , Vanessa Biochemistry Univ of Texas at Austin, Austin, TX	BS 99-0805	AL/CF	01/01/98 12/31/98	\$25000.00	\$0.00
			a Study on Stress-Induced Alterations In Blood-Brain Barrier Permeability to Pyr		
Gill , Guraam EE Naval Postgraduate School, Monterey, CA	PhD 99-0834	PL/VT	01/01/99 12/31/99	\$25000.00	\$0.00
			Adaptive signal Processing and its Applications in Space based Radar		
Hinde , Robert Physical Chemistry Univ of Tennessee, Knoxville, TN	PhD 99-0801	WL/PO	01/01/98 12/31/98	\$25000.00	\$3976.00
			Dopant-Induced Infrared Activity in Solid Hydrogen An AB Initio and Quantum Mont		
Jeffs , Brian Electrical Engineering Brigham Young University, Provo, UT	PhD 99-0828	PL/LI	01/01/98 12/31/98	\$25000.00	\$19177.00
			Algebraic Methods for Improved blind Restoration of Adaptive Optics Images of Sp		
Leo , Donald Mechanical & Aerospace Virginia Tech, Blacksburg, VA	PhD 99-0835	PL/VT	01/01/99 12/31/99	\$24999.00	\$7416.00
			Self-Sensing Acoustic Sources For Intericr Noise Control in Payload Fairings		
Lodhi , M. Arfin Nuclear Physics Texas Tech University, Lubbock, TX	PhD 99-0832	PL/VT	01/01/99 12/31/99	\$25000.00	\$0.00
			Investigatioin into Time-Dependent Power Losses from AMTEC Components		
McHugh , John Applied Mechanics University of New Hampshire, Durham, NH	PhD 99-0833	PL/VT	01/01/99 12/13/99	\$25000.00	\$7000.00
			Atmcspheric Gravity Waves Near The Tropopause		
Steinberg , Stanly Mathematics University of New Mexico, Albuquerque, NM	PhD 99-0829	PL/LI	01/01/99 12/31/99	\$25000.00	\$0.00
			Lie-Algebraic Representations of Product Integrals of Variable Matrices		
Stephens II , Kenneth University of North Texas, Denton, TX	MA 99-0830	PL/LI	01/01/99 12/31/99	\$25000.00	\$16764.00
			Simulation of a Magnetized Target Fusion Concept Using MACH2		
Arvas , Ercument Electrical Engineering Syracuse University, Syracuse, NY	PhD 99-0808	WL/AA	01/01/99 12/31/99	\$25000.00	\$13000.00
			Realization of Low Noise MMIC Amplifier as a Microwave-to-Optics Link for Radar		
Gopalan , Kaliappan Electrical Engineering Purdue Research Foundation, West Lafayette, IN	PhD 99-0814	RL/TR	01/01/99 12/31/99	\$25000.00	\$38168.00
			Detection of Acoustic Correlates of Stress from Modulation Characteristics		

SREP SUB-CONTRACT DATA

Report Author Author's University	Author's Degree	Sponsoring Lab	Performance Period	Contract Amount	Univ. Cost Share
Hung, Donald Electrical Engineering Washington State University, Richland, WA	PhD 99-0812	RL/IR An Investigation on Accelerating the Ray-Tracing Computations	01/01/99 12/31/99	\$25000.00	\$23008.00
Lutoborski, Adam Applied Mathematics Syracuse University, Syracuse, NY	PhD 99-0811	RL/IR Transform Methods for Watermarking Digital Images	01/01/99 12/31/99	\$25000.00	\$1274.00
Panda, Brajendra Computer Science University of North Dakota, Grand Forks, ND	PhD 99-0810	RL/IR Implementation of Petri Nets Based Multi-source Attack Detection Model	01/01/98 12/31/98	\$24942.00	\$2600.00
Potter, Jerry Computer Science Kent State University, Kent, OH	PhD 99-0809	RL/IR Algorithms for Data Intensive Knowledge Discovery	01/01/99 12/31/99	\$25000.00	\$52767.00
Upadhyaya, Shambhu Elec & Comp Engineering SUNY Buffalo, Buffalo, NY	PhD 99-0813	RL/IR a Distributed concurrent Intrusion Detection And recovery Scheme based on Assert	01/01/98 12/31/98	\$25000.00	\$6430.00
Ahmed, Farid Electrical engineering Penn State Uni-Erie, Erie, PA	PhD 99-0806	WL/AA Image Quality Assessment for ATR Applications Using Multiresolutional Information	10/10/98 12/31/98	\$25000.00	\$2396.00
Belfield, Kevin Chemistry University of Central Florida, Orlando, FL	PhD 99-0816	WL/ML Synthesis of New Two-Photon Absorbing Dyes, Monomers and Polymers	01/01/99 12/31/99	\$25000.00	\$5765.00
Buck, Gregory Mechanical Engineering S Dakota School of Mines/Tech, Rapid City, SD	PhD 99-0818	WL/FI Acoustic Disturbance Source Modeling and Development for Hypersonic Receptivity	01/01/99 12/31/99	\$25000.00	\$7639.00
Gilcrease, Patrick Chemical Engineering University of Wyoming, Laramie, WY	PhD 99-0815	WL/ML Biocatalysis of Biphenyl and Diphenylacetylene in an Aqueous-Organic Biphasic Re	01/01/99 12/31/99	\$25000.00	\$28010.00
Johnson, Jeffrey Electrical Engineering and University of Toledo, Toledo, OH	PhD 99-0823	WL/FI Incorporating Fixed, Adaptive, & Learning Controllers to the Flight Control	01/01/99 12/31/99	\$25000.00	\$10075.00
Kapila, Vikram Aerospace engineering Polytechnic Inst of New York, Brooklyn, NY	PhD 99-0820	WL/FI Dynamics and Control of Spacecraft Formation Flying	01/01/99 12/31/99	\$25000.00	\$17448.00
Kihm, Kenneth Mechanical Engineering Texas Engineering Experiment Station, College	PhD 99-0821	WL/FI Micro-Scale Flow Field Measurement of the Thin Meniscus of Capillary-Driven Heat	01/01/99 12/31/99	\$25000.00	\$10310.00
Li, Rongxing Photogrammetry & Remote Sensing Ohio State University, Columbus, OH	PhD 99-0831	WL/AA Uncertainty Modeling of Target Locations From Multiplatform and Multisensor Data	01/01/98 12/31/98	\$25000.00	\$13183.00
Lin, Chun-Shin Electrical Engineering Univ of Missouri - Columbia, Columbia, MO	PhD 99-0826	WL/MN Sensor Fusion w/Passive Millimeter Wave & Laser Radar for Target Detection	01/01/99 12/31/99	\$25000.00	\$1991.00
Liu, Chaoqun Applied Mathematics Louisiana Tech University, Ruston, LA	PhD 99-0819	WL/FI Boundary Conditions in Curvilinear Coordinates for Direct Numerical Simulation	01/01/99 12/31/99	\$25000.00	\$12521.00

SREP SUB-CONTRACT DATA

Report Author Author's University	Author's Degree	Sponsoring Lab	Performance Period	Contract Amount	Univ. Cost Share
Mungan , Carl Dept of Physics University of Florida, Pensacola, FL	PhD 99-0824	WL/MN	01/01/99 12/31/99 infrared Spectropolarimetric Directional Reflectance and Emissivity of Mental Sur	\$24914.00	\$3276.00
Ogale , Amod Chemical Engineering Clemson University, Clemson, SC	PhD 99-0817	WL/ML	01/01/99 12/31/99 Structural Changes in Mesophase Pitch-Based Carbon Fibers:In SITU &ES SITU Measu	\$25000.00	\$9000.00
Pidaparti , Ramana Aeronautics & Astronautics Indiana U-Purdue at Indianap, Indianapolis, IN	PhD 99-0822	WL/FI	01/01/99 12/31/99 Benchmarking Aerodynamic Panel Methods for Flight Loads in Multidisciplinary Opt	\$25000.00	\$10582.00
Saddow , Stephen Electrical Engineering Mississippi State University, Mississippi State,	PhD 99-0827	WL/PO	01/01/98 12/31/98 Silicon Carbide Implant Activation & Surface preparation Investigation	\$25000.00	\$0.00
Sepri , Paavo Engineering Science Florida Inst of Technology, Melbourne, FL	PhD 99-0836	WL/PO	01/01/99 12/31/99 Computational Study of Unsteady Flow Interactions Between Turbine Blades, Cylind	\$25000.00	\$6519.00
Shi , Hongchi Computer Engineering Univ of Missouri - Columbia, Columbia, MO	PhD 99-0825	WL/MN	01/01/99 12/31/99 Developing an efficient Algorithm for Routing Processors of the VGI Parallel Com	\$25000.00	\$15851.00
Soumekh , Mehrdad Elec/Computer Engineering SUNY Buffalo, Amherst, NY	PhD 99-0807	WL/AA	01/01/99 12/30/99 Signal and Image Processing for FOPEN/GPEN SAR	\$25000.00	\$0.00
Riviello , Craig Mechanical Wright State University, Dayton, OH	BS 99-0837	WL/ML	01/01/99 01/01/99 In-Situ Synthesis of Discontinuously Reinforced Titanium alloy Composites Via Bl	\$25000.00	\$6304.00

APPENDIX 1:

SAMPLE SREP SUBCONTRACT

**AIR FORCE OFFICE OF SCIENTIFIC RESEARCH
1999 SUMMER RESEARCH EXTENSION PROGRAM
SUBCONTRACT 99-0806**

BETWEEN

**Research & Development Laboratories
5800 Uplander Way
Culver City, CA 90230-6608**

AND

**Penn State Erie, The Behrend College
Contracts and Grants Office
Erie, PA 16563**

REFERENCE: Summer Research Extension Program Proposal 98-0029
Start Date: 01/01/99 End Date: 12/31/99
Proposal Amount: \$25,000
Proposal Title: Image Quality Assessment for ATR Applications Using
Multiresolutional Informational Information Metrics

PRINCIPAL INVESTIGATOR: Dr. Farid Ahmed
Penn State Erie, The Behrend College
Erie, PA 16563

- (2) **UNITED STATES AFOSR CONTRACT NUMBER: F49620-93-C-0063**
- (3) **CATALOG OF FEDERAL DOMESTIC ASSISTANCE NUMBER (CFDA): 12.800**
PROJECT TITLE: AIR FORCE DEFENSE RESEARCH SOURCES PROGRAM
- (4) **ATTACHMENTS**
1 **REPORT OF INVENTIONS AND SUBCONTRACT**
2 **CONTRACT CLAUSES**
3 **FINAL REPORT INSTRUCTIONS**

*****SIGN SREP SUBCONTRACT AND RETURN TO RDL*****

**AIR FORCE OFFICE OF SCIENTIFIC RESEARCH
1999 SUMMER RESEARCH EXTENSION PROGRAM
SUBCONTRACT 99-0806**

BETWEEN

**Research & Development Laboratories
5800 Uplander Way
Culver City, CA 90230-6608**

AND

**Penn State Erie, The Behrend College
Contracts and Grants Office
Erie, PA 16563**

REFERENCE: Summer Research Extension Program Proposal 98-0029
Start Date: 01/01/99 End Date: 12/31/99
Proposal Amount: \$25,000
Proposal Title: Image Quality Assessment for ATR Applications Using
Multiresolutional Informational Information Metrics

PRINCIPAL INVESTIGATOR: Dr. Farid Ahmed
Penn State Erie, The Behrend College
Erie, PA 16563

- (2) **UNITED STATES AFOSR CONTRACT NUMBER: F49620-93-C-0063**
- (3) **CATALOG OF FEDERAL DOMESTIC ASSISTANCE NUMBER (CFDA):12.800
PROJECT TITLE: AIR FORCE DEFENSE RESEARCH SOURCES PROGRAM**
- (4) **ATTACHMENTS**
1 **REPORT OF INVENTIONS AND SUBCONTRACT**
2 **CONTRACT CLAUSES**
3 **FINAL REPORT INSTRUCTIONS**

*****SIGN SREP SUBCONTRACT AND RETURN TO RDL*****

1. **BACKGROUND:** Research & Development Laboratories (RDL) is under contract (F49620-93-C-0063) to the United States Air Force to administer the Summer Research Program (SRP), sponsored by the Air Force Office of Scientific Research (AFOSR), Bolling Air Force Base, D.C. Under the SRP, a selected number of college faculty members and graduate students spend part of the summer conducting research in Air Force laboratories. After completion of the summer tour participants may submit, through their home institutions, proposals for follow-on research. The follow-on research is known as the Summer Research Extension Program (SREP). Approximately 61 SREP proposals annually will be selected by the Air Force for funding of up to \$25,000; shared funding by the academic institution is encouraged. SREP efforts selected for funding are administered by RDL through subcontracts with the institutions. This subcontract represents an agreement between RDL and the institution herein designated in Section 5 below.
2. **RDL PAYMENTS:** RDL will provide the following payments to SREP institutions:
 - 80 percent of the negotiated SREP dollar amount at the start of the SREP research period.
 - The remainder of the funds within 30 days after receipt at RDL of the acceptable written final report for the SREP research.
3. **INSTITUTION'S RESPONSIBILITIES:** As a subcontractor to RDL, the institution designated on the title page will:

- a. Assure that the research performed and the resources utilized adhere to those defined in the SREP proposal.
- b. Provide the level and amounts of institutional support specified in the SREP proposal..
- c. Notify RDL as soon as possible, but not later than 30 days, of any changes in 3a or 3b above, or any change to the assignment or amount of participation of the Principal Investigator designated on the title page.
- d. Assure that the research is completed and the final report is delivered to RDL not later than twelve months from the effective date of this subcontract, but no later than December 31, 1998. The effective date of the subcontract is one week after the date that the institution's contracting representative signs this subcontract, but no later than January 15, 1998.
- e. Assure that the final report is submitted in accordance with Attachment 3.
- f. Agree that any release of information relating to this subcontract (news releases, articles, manuscripts, brochures, advertisements, still and motion pictures, speeches, trade associations meetings, symposia, etc.) will include a statement that the project or effort depicted was or is sponsored by: Air Force Office of Scientific Research, Bolling AFB, D.C.
- g. Notify RDL of inventions or patents claimed as the result of this research as specified in Attachment 1.
- h. RDL is required by the prime contract to flow down patent rights and technical data requirements to this subcontract. Attachment 2 to this subcontract

contains a list of contract clauses incorporated by reference in the prime contract.

4. All notices to RDL shall be addressed to:

RDL AFOSR Program Office
5800 Uplander Way
Culver City, CA 90230-6609

5. By their signatures below, the parties agree to provisions of this subcontract.

Abe Sopher
RDL Contracts Manager

Signature of Institution Contracting Official

Typed/Printed Name

Date

Title

Institution

Date/Phone

ATTACHMENT 2
CONTRACT CLAUSES

This contract incorporates by reference the following clauses of the Federal Acquisition Regulations (FAR), with the same force and effect as if they were given in full text. Upon request, the Contracting Officer or RDL will make their full text available (FAR 52.252-2).

FAR CLAUSES

TITLE AND DATE

52.202-1	DEFINITIONS
52.203-3	GRATUITIES
52.203-5	COVENANT AGAINST CONTINGENT FEES
52.203-6	RESTRICTIONS ON SUBCONTRACTOR SALES TO THE GOVERNMENT
52.203-7	ANTI-KICKBACK PROCEDURES
52.203-8	CANCELLATION, RECISSION, AND RECOVERY OF FUNDS FOR ILLEGAL OR IMPROPER ACTIVITY
52.203-10	PRICE OR FEE ADJUSTMENT FOR ILLEGAL OR IMPROPER ACTIVITY
52.203-12	LIMITATION ON PAYMENTS TO INFLUENCE CERTAIN FEDERAL TRANSACTIONS
52.204-2	SECURITY REQUIREMENTS
52.209-6	PROTECTING THE GOVERNMENT'S INTEREST WHEN SUBCONTRACTING WITH CONTRACTORS DEBARRED, SUSPENDED, OR PROPOSED FOR DEBARMENT
52.212-8	DEFENSE PRIORITY AND ALLOCATION REQUIREMENTS
52.215-2	AUDIT AND RECORDS - NEGOTIATION
52.215-10	PRICE REDUCTION FOR DEFECTIVE COST OR PRICING DATA

52.215-12	SUBCONTRACTOR COST OR PRICING DATA
52.215-14	INTEGRITY OF UNIT PRICES
52.215-8	ORDER OF PRECEDENCE
52.215.18	REVERSION OR ADJUSTMENT OF PLANS FOR POSTRETIREMENT BENEFITS OTHER THAN PENSIONS
52.222-3	CONVICT LABOR
52.222-26	EQUAL OPPORTUNITY
52.222-35	AFFIRMATIVE ACTION FOR SPECIAL DISABLED AND VIETNAM ERA VETERANS
52.222-36	AFFIRMATIVE ACTION FOR HANDICAPPED WORKERS
52.222-37	EMPLOYMENT REPORTS ON SPECIAL DISABLED VETERAN AND VETERANS OF THE VIETNAM ERA
52.223-2	CLEAN AIR AND WATER
52.223-6	DRUG-FREE WORKPLACE
52.224-1	PRIVACY ACT NOTIFICATION
52.224-2	PRIVACY ACT
52.225-13	RESTRICTIONS ON CONTRACTING WITH SANCTIONED PERSONS
52.227-1	ALT. I - AUTHORIZATION AND CONSENT
52.227-2	NOTICE AND ASSISTANCE REGARDING PATIENT AND COPYRIGHT INFRINGEMENT

52.227-10	FILING OF PATENT APPLICATIONS - CLASSIFIED SUBJECT MATTER
52.227-11	PATENT RIGHTS - RETENTION BY THE CONTRACTOR (SHORT FORM)
52.228-7	INSURANCE - LIABILITY TO THIRD PERSONS
52.230-5	COST ACCOUNTING STANDARDS - EDUCATIONAL INSTRUCTIONS
52.232-23	ALT. I - ASSIGNMENT OF CLAIMS
52.233-1	DISPUTES
52.233-3	ALT. I - PROTEST AFTER AWARD
52.237-3	CONTINUITY OF SERVICES
52.246-25	LIMITATION OF LIABILITY - SERVICES
52.247-63	PREFERENCE FOR U.S. - FLAG AIR CARRIERS
52.249-5	TERMINATION FOR CONVENIENCE OF THE GOVERNMENT (EDUCATIONAL AND OTHER NONPROFIT INSTITUTIONS)
52.249-14	EXCUSABLE DELAYS
52.251-1	GOVERNMENT SUPPLY SOURCES

DOD FAR CLAUSES**DESCRIPTION**

252.203-7001

SPECIAL PROHIBITION ON EMPLOYMENT

252.215-7000

PRICING ADJUSTMENTS

252.233-7004

DRUG FREE WORKPLACE (APPLIES TO
SUBCONTRACTS WHERE THERE IS
ACCESS TO CLASSIFIED INFORMATION)

252.225-7001

BUY AMERICAN ACT AND BALANCE OF
PAYMENTS PROGRAM

252.225-7002

QUALIFYING COUNTRY SOURCES AS
SUBCONTRACTS

252.227-7013

RIGHTS IN TECHNICAL DATA -
NONCOMMERCIAL ITEMS

252.227-7030

TECHNICAL DATA - WITHHOLDING
PAYMENT

252.227-7037

VALIDATION OF RESTRICTIVE MARKINGS
ON TECHNICAL DATA

252.231-7000

SUPPLEMENTAL COST PRINCIPLES

252.232-7006

REDUCTIONS OR SUSPENSION OF
CONTRACT PAYMENTS UPON FINDING OF
FRAUD

APPENDIX 2:

SAMPLE TECHNICAL EVALUATION FORM

**SUMMER RESEARCH EXTENSION PROGRAM
TECHNICAL EVALUATION**

SREP NO: 99-0828

PRINCIPAL INVESTIGATOR: Dr. Brian Jeffs

Brigham Young University

Circle the rating level number, 1 (low) through 5 (high),
you feel best evaluate each statement and return the
completed form by fax or mail to:

RDL

Attn: SREP Tech Evals

5800 Uplander Way

Culver City, CA 90230-6608

-
- | | |
|---|-----------|
| 1. This SREP report has a high level of technical merit | 1 2 3 4 5 |
| 2. The SREP program is important to accomplishing the lab's mission | 1 2 3 4 5 |
| 3. This SREP report accomplished what the associate's proposal promised | 1 2 3 4 5 |
| 4. This SREP report addresses area(s) important to USAF | 1 2 3 4 5 |
| 5. The USAF should continue to pursue the research in this SREP report | 1 2 3 4 5 |
| 6. The USAF should maintain research relationships with this SREP associate | 1 2 3 4 5 |
| 7. The money spent on this SREP effort was well worth it. | 1 2 3 4 5 |
| 8. This SREP report is well organized and well written | 1 2 3 4 5 |
| 9. I'll be eager to be a focal point for summer and SREP associates in the future | 1 2 3 4 5 |
| 10. The one-year period for complete SREP research is about right. | 1 2 3 4 5 |
-

11. If you could change any one thing about the SREP program, what would you change:

12. What do you definitely NOT change about the SREP program?

PLEASE USE THE BACK FOR ANY OTHER COMMENTS

Laboratory: AFRL/IFEC

Lab Focal Point: Mr. Stanley Wendt

PHONE: (315) 330-7244

Dr. Gurnam Gill's report was not available at the time of publication.

INFRARED ACTIVITY OF LITHIUM-DOPED SOLID PARAHYDROGEN:
A DIFFUSION QUANTUM MONTE CARLO STUDY

Robert J. Hinde
Assistant Professor
Department of Chemistry

The University of Tennessee
Knoxville, TN 37996-1600

Final Report for:
Summer Research Extension Program
Wright Laboratory

Sponsored by:
Air Force Office of Scientific Research
Bolling Air Force Base, DC

and

The University of Tennessee

February 2000

INFRARED ACTIVITY OF LITHIUM-DOPED SOLID PARAHYDROGEN:
A DIFFUSION QUANTUM MONTE CARLO STUDY

Robert J. Hinde
Assistant Professor
Department of Chemistry
The University of Tennessee
Knoxville, TN 37996-1600

Abstract

We have developed computational tools for computing the lineshape and intensity of the $Q_1(0)$ IR spectral features induced in solid p-H₂ crystals by S-state atomic dopants, and have applied these tools to Li-doped solid p-H₂. The integrated absorption coefficient for the H₂ $Q_1(0)$ band for Li-doped solid p-H₂ is computed to be $\tilde{\alpha} = 4.1 \times 10^{-13}$ cm³/s per Li impurity. Our predicted $Q_1(0)$ lineshape contains rich structure which may shed light on the microscopic morphology of Li trapping sites in solid p-H₂.

INFRARED ACTIVITY OF LITHIUM-DOPED SOLID PARAHYDROGEN: A DIFFUSION QUANTUM MONTE CARLO STUDY

Robert J. Hinde

1. Introduction

Atom-doped solid H_2 has recently been identified as an additive which could improve the performance of rocket propulsion systems utilizing a liquid oxygen-liquid hydrogen (LOX/LH₂) propellant [4]. Specific impulse (I_{sp}) is a standard performance metric for rocket propulsion systems, which measures the momentum transferred to the rocket per unit weight of propellant consumed. For the current state-of-the-art LOX/LH₂ propellant system, $I_{sp} = 389$ s [24]. However, if the hydrogen propellant contains Al atoms at a mole concentration of 5%, the theoretical I_{sp} of this propellant system increases by 9% to 425 s; if the hydrogen propellant contains 5% B atoms, the theoretical I_{sp} jumps to 470 s, for an improvement of 21% [4]. Consequently, Fajardo and coworkers at the Air Force Research Laboratory (AFRL) have begun attempts to synthesize gram-scale quantities of atom-doped solid H_2 with impurity concentrations approaching 5%. The success of these attempts would represent a milestone for the Air Force High Energy Density Matter program.

To guide and evaluate these synthetic efforts, the AFRL cryosolids group must be able to measure accurately the concentration of atomic dopants in solid H_2 matrices. Some of the first experimental [9, 10] and theoretical [8] attempts to characterize atom-doped H_2 matrices focused on the optical absorption spectra of the dopant atoms. As an example, Fig. 1 (reprinted from Ref. [9]) shows the absorption spectrum of solid H_2 doped with Li atoms at a concentration of roughly 2×10^{-5} . The strong absorption feature near $\lambda = 670$ nm is associated with the $2s \rightarrow 2p$ electronic transition of the Li dopant atoms.

Although electronic spectroscopy of doped H_2 matrices provides a convenient method for detecting the presence or absence of dopants, it is less suitable for measuring dopant concentrations because atom-doped solid H_2 becomes optically thick in the visible and ultraviolet regions at very low dopant concentrations. For example, Fig. 1 indicates that the transmittance T_{670} at 670 nm for this Li-doped solid H_2 sample is 0.8. A simple analysis based on Beer's Law suggests that T_{670} for a sample of the same thickness but with a Li concentration of 0.05% will be $(0.8)^{25} \approx 0.04$. Hence samples with Li concentrations of 1 to 5% will be optically thick at 670 nm, so that no quantitative concentration information can be obtained from the

absorption spectrum.

Atom-doped solid H_2 matrices also absorb weakly in the infrared (IR) spectral region [11], as Fig. 2 illustrates. As we explain in more detail below, the IR absorption features shown in this figure arise from nominally IR inactive vibrational transitions of individual H_2 molecules in the matrix that become IR active in the presence of dopants. These features are rather weak, so that 1-mm thick samples of doped solid H_2 will remain optically thin (with transmittance values of 0.1 or higher) even at dopant concentrations approaching 5%. Furthermore, Fig. 2 indicates that atom-doped solid H_2 and molecule-doped solid H_2 have distinct IR spectral signatures; this could make it possible to monitor the aggregation of atomic dopants in H_2 matrices using spectroscopic techniques.

The spectra reprinted in Fig. 2 are some of the first published examples of infrared activity induced in solid H_2 matrices by atomic dopants. The integrated absorption coefficients for the atom-induced features shown in this figure are not known experimentally and have not been calculated theoretically. If these absorption coefficients were known, spectra such as those shown in Fig. 2 could obviously provide quantitative measures of the concentration of atomic impurities in doped solid H_2 . Hence a better understanding of these spectra would be of immediate and direct use to the AFRL cryosolids group.

We report here a calculation of the lineshape and absolute intensity for the IR spectral features induced in solid H_2 by the atomic dopant Li. Li-doped solid H_2 has been widely used as a theoretical and experimental model system in the Air Force HEDM program. The intensities of the Li-induced IR features are related to the total space-fixed transition dipole moment vector induced in the solid H_2 matrix upon vibrational excitation of a single H_2 molecule in the vicinity of the Li atom. We have computed this transition moment as the expectation value of the corresponding transition dipole operator over the ground state wavefunction of the doped solid H_2 matrix, using diffusion quantum Monte Carlo (DQMC) simulations to sample the wavefunction of the H_2 matrix and descendant weighting techniques to compute expectation values of the transition dipole operator.

The remainder of this report is organized as follows. Section 2 describes the theoretical basis for understanding the IR activity induced in solid H_2 matrices by S-state atomic dopants. In Section 3, we show how DQMC simulations of solid H_2 can be used to compute the lineshape and intensity of these dopant-induced spectral features. Section 4 summarizes our work on Li-doped solid H_2 .

2. Theoretical background: IR activity induced in solid H_2 by S-state atomic dopants

Here we outline the theoretical basis for understanding the IR activity of solid H_2 matrices doped with S-state atomic impurities. We begin by summarizing some of the properties of pure solid H_2 , which has been the subject of a number of recent reviews [23, 29].

A. Properties of solid hydrogen

In solid H_2 , the rotational and vibrational motions of individual H_2 molecules are essentially unperturbed by the H_2 - H_2 intermolecular interactions; hence the rotational and vibrational quantum numbers j and v of each molecule remain good quantum numbers in solid H_2 [23, 29]. The requirements of quantum statistics dictate that H_2 molecules with a total nuclear spin quantum number $I = 0$ (or a singlet nuclear spin state) must have even j values, while H_2 molecules with $I = 1$ (or a triplet nuclear spin state) must have odd j values. Molecules with $I = 0$ (and even j) are termed parahydrogen or p- H_2 ; molecules with $I = 1$ (and odd j) are termed orthohydrogen or o- H_2 . Solid H_2 matrices consisting of virtually 100% p- H_2 molecules with $j = 0$ can be prepared by passing a flow of H_2 gas over an ortho \rightarrow para conversion catalyst and condensing the resulting p- H_2 molecules [11].

Solid p- H_2 condenses into a hexagonal close packed (hcp) crystal structure with a nearest-neighbor distance of $7.16 a_0$ [23]. The rotational degrees of freedom of each H_2 molecule in this crystal are described by the isotropic spherical harmonic $Y_{00}(\theta, \phi)$; the p- H_2 crystal is thus composed of spherically symmetric objects with multipole moments that are identically zero, and is held together exclusively by dispersion forces. The H_2 molecules in the p- H_2 crystal can be treated as point particles, each with a single vibrational degree of freedom. The translational zero point motion of individual molecules in the solid H_2 matrix is rather large, so that the width of the first peak in the radial distribution function for solid H_2 is approximately 18% of the nearest-neighbor distance, even in the $T = 0$ K limit [23]. Self-diffusion in solid p- H_2 is slow; at $T = 10$ K, a given p- H_2 molecule spends $38 \mu s$ at a given lattice site before "hopping" to a neighboring site [23]. Consequently, it is a good approximation to treat each p- H_2 molecule as permanently associated with a specific crystal lattice site [8].

B. Spectroscopy of pure solid parahydrogen

Consider the $Q_1(0)$ vibrational excitation $(v, j) = (0, 0) \rightarrow (1, 0)$ of a single H_2 molecule in solid p- H_2 .^{*} This transition will be IR active only if the initial and final states of the crystal are connected by a nonzero

^{*} In an isolated H_2 molecule, these two rovibrational states are separated by 4161.2 cm^{-1} of energy; in solid H_2 , the $Q_1(0)$ transition is slightly red-shifted to 4153.0 cm^{-1} by H_2 - H_2 intermolecular interactions [29].

transition dipole moment matrix element. Because each H_2 molecule in the system is spherically symmetric in both the initial and the final state of the crystal, there can be no contribution to the transition moment from dipoles induced on individual H_2 molecules by the permanent electrostatic multipoles of neighboring molecules. Hence the transition moment for this vibrational excitation arises from “overlap induction” or “exchange induction” effects due to the interpenetration of neighboring molecules’ electron distributions, and from the mutual polarization of neighboring molecules due to dispersion interactions.

The total dipole moment of a pair of H_2 molecules with quantum numbers $(v, j) = (0, 0)$ must be zero at any H_2 - H_2 distance: each individual H_2 molecule is spherically symmetric by virtue of its $j = 0$ quantum number, and the $(\text{H}_2)_2$ dimer therefore has inversion symmetry about the dimer’s center of mass. However, if one of the two H_2 molecules is in the $(v, j) = (1, 0)$ state, this inversion symmetry is broken and the pair of molecules will possess a nonzero dipole moment arising from the exchange and dispersion induction mechanisms outlined above. This makes the H_2 vibrational fundamental IR active in $(\text{H}_2)_2$ van der Waals dimers [16, 17] and in the collision-induced absorption spectrum of dense hydrogen gas [19].

In a pure p- H_2 crystal, however, the $Q_1(0)$ transition is IR inactive. Suppose that a particular H_2 molecule in the hcp p- H_2 crystal is excited to the $(v, j) = (1, 0)$ state. In the hcp lattice, the vectors connecting this excited H_2 molecule with its twelve nearest neighbors sum to zero. Hence the *net* dipole moment induced in the crystal by the vibrational excitation of one molecule is zero [28], although the vibrationally excited H_2 molecule induces “pairwise” dipole moments with each of its $v = 0$ neighbors as shown in Fig. 3. This consequence of the hcp lattice symmetry is known as the “cancellation effect” [27, 28]; it causes the $Q_1(0)$ transition to be IR inactive in the pure p- H_2 hcp crystal, as is evident from the bottom spectrum in Fig. 2.

C. Spectroscopy of solid parahydrogen doped with orthohydrogen molecules

Now consider a crystal of solid p- H_2 in which a single p- H_2 molecule has been replaced by an o- H_2 molecule with $j = 1$. The o- H_2 molecule is not spherically symmetric and thus has a nonzero quadrupole moment (along with higher multipole moments). The quadrupole field of the o- H_2 molecule induces dipole moments in nearby p- H_2 molecules; the $Q_1(0)$ transitions of these p- H_2 molecules become IR active by virtue of these induced moments.

To demonstrate this, we compute the transition dipole moment associated with this excitation using arguments presented in Ref. [21], making the simplifying assumption that the centers of mass of the H_2 molecules in the crystal are held fixed. Let \mathbf{E}_n be the electric field of the o- H_2 impurity at the n th p- H_2

molecule; the dipole moment induced in this p-H₂ molecule by the o-H₂ impurity is $\mathbf{m}_n = 4\pi\epsilon_0\alpha\mathbf{E}_n$ where α is the (isotropic) polarizability of the p-H₂ molecule. (We neglect the overlap induced dipole described above; at the nearest-neighbor distance of solid H₂, this dipole is much smaller in magnitude than the dipole induced by the quadrupole field.) If we assume that the total induced dipole \mathbf{M} of the system is simply the sum of these induced moments, then the transition moment associated with the $Q_1(0)$ transition of the k th p-H₂ molecule is

$$\mathbf{M}_{fi}^{(k)} = \left\langle i \left| 4\pi\epsilon_0\alpha \sum_n \mathbf{E}_n \right| f \right\rangle = 4\pi\epsilon_0\alpha_{01}\mathbf{E}_k \quad (1)$$

where $|i\rangle$ and $|f\rangle$ represent the initial and final states of the doped crystal, the superscript (k) indicates that the k th p-H₂ molecule is undergoing excitation, and $\alpha_{01} = \langle v=0 | \alpha | v=1 \rangle$ is the isotropic "transition polarizability" of H₂, which has the value $\alpha_{01} = 0.65$ au [20]. Note that terms in \mathbf{M} with $n \neq k$ do not contribute to $\mathbf{M}_{fi}^{(k)}$ due to the orthogonality of the H₂ vibrational wavefunctions with $v_k = 0$ and $v_k = 1$. Because $\mathbf{M}_{fi}^{(k)} \neq 0$ if $\mathbf{E}_k \neq 0$, the $Q_1(0)$ transition of a p-H₂ molecule near an o-H₂ impurity will be IR active. The top spectrum shown in Fig. 2 is the IR absorption spectrum of a p-H₂ matrix doped with 2% o-H₂; the $Q_1(0)$ transition of the p-H₂ host is clearly visible.

The integrated absorption coefficient of this transition is related to $\mathbf{M}_{fi}^{(k)}$ through [1]

$$\tilde{\alpha} = \frac{2\pi^2}{3\epsilon_0 h} \sum_k |\mathbf{M}_{fi}^{(k)}|^2. \quad (2)$$

Although this sum appears to diverge as the number of p-H₂ molecules $N \rightarrow \infty$, the contribution to $\tilde{\alpha}$ from a p-H₂ molecule which is far away from the o-H₂ impurity is negligible because \mathbf{E}_k decays quickly with increasing distance. Evaluation of $\mathbf{M}_{fi}^{(k)}$ using Eqs. (1) and (2) leads to a theoretical $Q_1(0)$ integrated IR absorption coefficient of $\tilde{\alpha} = 2.0 \times 10^{-14}$ cm³/s per o-H₂ impurity [21]; the corresponding experimental value is 2.2×10^{-14} cm³/s [12]. The small discrepancy between theory and experiment can be rationalized by recalling that we have neglected both the motion of the H₂ molecules and the contributions to the transition dipole moment from overlap induction and from three-body effects.

A similar approach has recently been used to estimate the integrated absorption coefficients of the $S_1(0)$ and $U_1(0)$ transitions in solid p-H₂ doped with o-H₂ impurities [2]; the good agreement between experiment and theory obtained for these transitions underscores the validity of this approach.

D. Spectroscopy of solid parahydrogen doped with S-state atoms

Finally we consider a p-H₂ crystal with N H₂ molecules and a single S-state atomic impurity. As Fig. 2 shows, S-state atoms embedded in p-H₂ induce weak IR activity in the $Q_1(0)$ spectral region. In contrast

to o-H₂ impurities, S-state atoms have no permanent multipole moments; hence the transition moment associated with this IR activity must arise solely from overlap and dispersion effects, and from the fact that the dopant atom breaks the symmetry of the hcp lattice. We now derive an expression for this transition dipole moment.

Let \mathbf{R}_0 denote the position of the atomic impurity and $\{\mathbf{R}_n : n = 1, 2, 3, \dots, N\}$ denote the centers of mass of the H₂ molecules in the crystal. The vibrational quantum number of the H₂ molecule at \mathbf{R}_k will be denoted v_k ; we assume that the rotational quantum number j of each H₂ molecule is zero. (The quantum number j will remain a good quantum number if the dopant-H₂ interaction is isotropic, or very nearly so, at low energies; this is the case for Li dopants [6].) The state of the doped crystal is therefore completely specified by the position vectors $\{\mathbf{R}_0, \mathbf{R}_1, \mathbf{R}_2, \dots, \mathbf{R}_N\}$ and the list of vibrational quantum numbers $\{v_1, v_2, \dots, v_N\}$.

We focus our attention on the $v_1 = 0 \rightarrow 1$ transition of the H₂ molecule at \mathbf{R}_1 . Let $|i\rangle$ denote the initial state of the doped crystal, in which $v_k = 0$ for all k , and let $|f\rangle$ denote the final state of the crystal, in which $v_1 = 1$ and $v_k = 0$ for $k > 1$. We assume that the dipole moment operator for this system can be written as a pairwise sum of overlap-induced dipoles:

$$\mathbf{M}^{(1)} = \sum_{j=0}^{N-1} \sum_{k=j+1}^N \mathbf{m}^{(j,k)} = \sum_{k=1}^N \mathbf{m}^{(0,k)} + \sum_{k=2}^N \mathbf{m}^{(1,k)} \quad (3)$$

where $\mathbf{m}^{(j,k)}$ represents the dipole moment induced by the overlap of the particles at \mathbf{R}_j and \mathbf{R}_k . Note that if the dipole moment is pairwise additive, (p-H₂)₂ pairs in which both molecules remain in the ground state $(v, j) = (0, 0)$ cannot contribute to the dipole moment.

The transition moment for the $Q_1(0)$ transition of the H₂ molecule at \mathbf{R}_1 is $M_{fi}^{(1)} = \langle i | \mathbf{M}^{(1)} | f \rangle$. To evaluate $M_{fi}^{(1)}$, we first integrate over the vibrational coordinates of all N H₂ molecules. Because the $v = 0$ and $v = 1$ vibrational wavefunctions for H₂ are orthogonal, this integration eliminates from $M_{fi}^{(1)}$ all terms which do not depend on the vibrational coordinate of the molecule at \mathbf{R}_1 . Hence we obtain

$$M_{fi}^{(1)} = \int \Psi_i^*(\mathbf{Q}) \left[\mathbf{m}_{01}^{(0,1)} + \sum_{k=2}^N \mathbf{m}_{01}^{(1,k)} \right] \Psi_f(\mathbf{Q}) d\mathbf{Q} \quad (4)$$

where $\mathbf{Q} = \{\mathbf{R}_0, \mathbf{R}_1, \mathbf{R}_2, \dots, \mathbf{R}_N\}$ is the collection of position vectors describing the system. The initial and final spatial wavefunctions of the system (after integrating over the H₂ vibrational coordinates) are $\Psi_i(\mathbf{Q})$ and $\Psi_f(\mathbf{Q})$. The vibrationally averaged pairwise contributions to the transition moment are

$$\mathbf{m}_{01}^{(0,1)} = \langle v_1 = 0 | \mathbf{m}^{(0,1)} | v_1 = 1 \rangle \quad (5)$$

for the dipole arising from overlap between the atomic impurity and the H₂ molecule at \mathbf{R}_1 , and (for $k > 1$)

$$\mathbf{m}_{01}^{(1,k)} = \langle v_1 = 0, v_k = 0 | \mathbf{m}^{(1,k)} | v_1 = 1, v_k = 0 \rangle \quad (6)$$

for the dipole arising from overlap between the H_2 molecules at R_1 and R_k . We emphasize that $m_{01}^{(0,1)}$ and $m_{01}^{(1,k)}$ are *vector* quantities which are oriented along the vectors $R_{0,1} = R_1 - R_0$ and $R_{1,k} = R_k - R_1$ respectively, and which depend on the distances $R_{0,1}$ and $R_{1,k}$.

From Eq. (4) we obtain the total transition dipole moment for vibrational excitation of the H_2 molecule located at R_1 . The contribution to the crystal's integrated absorption coefficient from this excitation is [cf. Eq. (2)]

$$\tilde{\alpha}^{(1)} = \frac{2\pi^2}{3\epsilon_0 h} |M_{fi}^{(1)}|^2. \quad (7)$$

Each H_2 molecule contributes in a similar fashion to the absorption spectrum, so that the total absorption coefficient per atomic impurity is

$$\tilde{\alpha} = \sum_j \tilde{\alpha}^{(j)} = \frac{2\pi^2}{3\epsilon_0 h} \sum_j |M_{fi}^{(j)}|^2. \quad (8)$$

3. Computational approach: DQMC simulations of the H_2 $Q_1(0)$ band

A. Absorption coefficients

The transition moment $M_{fi}^{(j)}$ is an integral over the initial wavefunction $\Psi_i(Q)$ and the final wavefunction $\Psi_f(Q)$ of the doped p- H_2 matrix. Because solid p- H_2 is a quantum crystal, individual H_2 molecules in the crystal undergo large-amplitude anharmonic zero point motion around their nominal lattice sites [23]. In addition, the instantaneous positions of neighboring p- H_2 molecules are highly correlated [8]. Therefore the many-body wavefunctions Ψ_i and Ψ_f characterizing the doped crystal's translational degrees of freedom cannot be obtained in analytic form, and Eq. (4) cannot be evaluated directly. However, we can estimate $M_{fi}^{(j)}$ using Monte Carlo sampling techniques.

Without loss of generality, we can take $\Psi_i(Q)$ to be a real function, so that $\Psi_i(Q) = \Psi_i^*(Q)$. Then Eq. (4) can be rewritten as

$$M_{fi}^{(1)} = \int \Psi_i(Q) \left[m_{01}^{(0,1)} + \sum_{k=2}^N m_{01}^{(1,k)} \right] \Psi_f(Q) dQ = \int f(Q) P(Q) dQ \quad (9)$$

where

$$f(Q) = m_{01}^{(0,1)} + \sum_{k=2}^N m_{01}^{(1,k)} \quad (10)$$

is the instantaneous $Q_1(0)$ transition moment for crystal configuration Q , and $P(Q) = \Psi_i(Q)\Psi_f(Q)$ can be interpreted as a probability density. If we have a method for selecting configurations $\{Q_1, Q_2, Q_3, \dots\}$ from $P(Q)$, then we can approximate the integral $M_{fi}^{(1)}$ as

$$M_{fi}^{(1)} \approx 1/n \sum_{j=1}^n f(Q_j). \quad (11)$$

As the number of sampled configurations $n \rightarrow \infty$, this Monte Carlo approximation converges to the integral's exact value.

There is no computationally efficient method for selecting configurations according to a probability density of the form $\Psi_i(\mathbf{Q})\Psi_f(\mathbf{Q})$ when the wavefunctions Ψ_i and Ψ_f are both unknown. However, if we make the simplifying assumption that $\Psi_i \approx \Psi_f$, then we can replace $P(\mathbf{Q})$ in Eq. (9) with $P(\mathbf{Q}) = |\Psi_i(\mathbf{Q})|^2$; a probability density function with this form can be readily sampled during a DQMC simulation* of the doped p-H₂ crystal using descendant weighted DQMC techniques [5]. This permits us to estimate $\mathbf{M}_{fi}^{(1)}$. In fact, using descendant weighting techniques, we can simultaneously evaluate $\mathbf{M}_{fi}^{(j)}$ for each H₂ molecule $1 \leq j \leq N$ in one DQMC simulation, thereby obtaining all of the information needed to compute $\tilde{\alpha}$ using Eq. (8).

This approach rests on the assumption that $\Psi_i \approx \Psi_f$. The validity of this assumption would be questionable if vibrationally excited p-H₂ could not easily fit into the solid H₂ lattice; in this case, the vibrationally excited molecule would experience substantial repulsive forces, and we would expect the $Q_1(0)$ transition of this molecule to be strongly blue-shifted. However, as Fig. 2 shows, the H₂ $Q_1(0)$ transition in doped solid H₂ is weakly red-shifted from the gas-phase $Q_1(0)$ transition of 4161.2 cm⁻¹; this suggests that the assumption that $\Psi_i \approx \Psi_f$ is reasonable.**

The validity of our approach is demonstrated by our recent calculation [13] of the absorption coefficient for the $Q_1(0) + Q_2(0)$ double vibrational transition in solid p-H₂ observed by Mengel and coworkers [18]. In this transition, a single IR photon excites the vibrational coordinates of two neighboring p-H₂ molecules simultaneously; the intensity of the transition arises from overlap-induced (p-H₂)₂ dipole moments described by Eq. (6). Because these moments vary strongly with distance [19], we must explicitly incorporate the molecules' translational zero-point motion into our calculation of the overall transition moment \mathbf{M}_{fi} .

Using the techniques described in this section, we obtained [13] an absorption coefficient for the

* DQMC simulations sample the ground state wavefunction of the doped p-H₂ crystal, and thus are strictly valid only in the limit $T = 0$ K. The methods outlined in this proposal could also be applied to finite-temperature path integral Monte Carlo studies of solid p-H₂. However, thermal effects on the solid p-H₂ induced $Q_1(0)$ intensity and lineshape are negligible below $T = 10$ K [15], so a simpler DQMC-based approach is sufficient.

** We note that this assumption could be tested by computing the transition moment $\mathbf{M}_{fi}^{(j)}$ using "nested walk" DQMC techniques originally designed for the quantum Monte Carlo evaluation of *electronic* transition dipole moments [3]. However, these techniques are very computationally intensive.

$Q_1(0) + Q_2(0)$ double transition of $\tilde{\alpha} = 1.1 \times 10^{-18} \text{ cm}^3/\text{s}$; the experimental value [18] is $\tilde{\alpha} = (9.3 \pm 0.9) \times 10^{-19} \text{ cm}^3/\text{s}$. If we make the simplifying assumption that the H_2 molecules are fixed at their nominal lattice sites, we instead obtain a theoretical absorption coefficient of $\tilde{\alpha} = 2.5 \times 10^{-20} \text{ cm}^3/\text{s}$, which is nearly 40 times too small. This discrepancy emphasizes that computational methods which account for the quantum behavior of the p- H_2 crystal, such as DQMC, are needed for a quantitative treatment of the IR transitions in solid p- H_2 arising from overlap-induced dipole moments.

B. Lineshapes

The integrated absorption coefficient $\tilde{\alpha}$ in Eq. (8) obtained from the individual transition moments $\mathbf{M}_{fi}^{(j)}$ represents the total absorption intensity (per dopant) of all of the dopant-induced IR spectral features associated with the H_2 $Q_1(0)$ transition. Figure 2 shows that molecular dopants induce multiple absorption features in the H_2 $Q_1(0)$ spectral region, and that both atom- and molecule-induced features apparently have a finite width. The integrated absorption coefficient $\tilde{\alpha}$ of Eq. (8) thus represents an integral over the entire induced $Q_1(0)$ band, which extends across the interval 4140 cm^{-1} to 4170 cm^{-1} .

The multiplicity of features induced by molecular dopants is presumably related to the anisotropy of these dopants; p- H_2 molecules on different "sides" of the dopants may absorb IR radiation of slightly different frequencies. To understand how dopant-induced IR spectra of solid H_2 could be used to monitor the aggregation of dopants in the matrix, we must therefore be able to predict the *lineshape* of the $Q_1(0)$ band as well as its total intensity. We now outline a method for predicting this lineshape using DQMC simulations.

To perform a DQMC simulation of doped solid p- H_2 , we require a potential energy surface for the doped p- H_2 crystal. This surface is a function of the positions of the individual p- H_2 molecules and the dopant, and of the vibrational quantum numbers of the p- H_2 molecules: $V = V(\mathbf{Q}, v_1, v_2, \dots, v_N)$. A DQMC simulation of the crystal under the constraint $v_1 = v_2 = \dots = v_N = 0$ would sample configurations from the initial wavefunction $\Psi_i(\mathbf{Q})$ and, if coupled with descendant weighting techniques, would allow us to compute expectation values over $|\Psi_i(\mathbf{Q})|^2$. The DQMC simulation also generates an estimate of the total energy E_0 of the ground state of the doped crystal under the constraint $v_1 = v_2 = \dots = v_N = 0$.

If we perform a second DQMC simulation of the crystal, this time under the constraint $v_1 = 1$ and $v_2 = v_3 = \dots = v_N = 0$, we obtain the energy $E_1^{(1)}$ of the state of the crystal in which molecule 1 has been excited to the $v = 1$ level. (We assume for the moment that the vibrational excitation remains localized on molecule 1.) The transition energy between the ground state of the doped crystal and this vibrationally

excited state is $\Delta E^{(1)} = E_1^{(1)} - E_0$. According to this picture, the $Q_1(0)$ transition of this p-H₂ molecule would be a sharp peak at this transition energy, with a total intensity given by Eq. (7).

However, if the vibrational coordinate of molecule 1 is only weakly coupled to the translational coordinates \mathbf{Q} , which is to say that $V(\mathbf{Q}, v_1 = 0, v_2, \dots, v_N) \approx V(\mathbf{Q}, v_1 = 1, v_2, \dots, v_N)$, then $\Delta E^{(1)}$ can be approximated using perturbation theory. The ground state energy E_0 satisfies

$$E_0 = \langle \Psi_i | \hat{H} | \Psi_i \rangle = \langle \Psi_i | \hat{T} + V(\mathbf{Q}, v_1 = 0, v_2, \dots, v_N) | \Psi_i \rangle \quad (12)$$

and $E_1^{(1)}$ satisfies

$$E_1^{(1)} = \langle \Psi_f | \hat{H} | \Psi_f \rangle = \langle \Psi_f | \hat{T} + V(\mathbf{Q}, v_1 = 1, v_2, \dots, v_N) | \Psi_f \rangle. \quad (13)$$

But if we define

$$\Delta V^{(1)}(\mathbf{Q}) = V(\mathbf{Q}, v_1 = 1, v_2, \dots, v_N) - V(\mathbf{Q}, v_1 = 0, v_2, \dots, v_N), \quad (14)$$

and if $\Delta V^{(1)}(\mathbf{Q})$ is small at configurations \mathbf{Q} which are accessible to the ground state wavefunction (which implies $\Psi_i \approx \Psi_f$), then from first-order perturbation theory we have

$$E_1^{(1)} \approx E_0 + \langle \Psi_i | \Delta V^{(1)}(\mathbf{Q}) | \Psi_i \rangle \quad \text{or} \quad \Delta E^{(1)} \approx \langle \Psi_i | \Delta V^{(1)}(\mathbf{Q}) | \Psi_i \rangle. \quad (15)$$

This expectation value of $\Delta V^{(1)}$ over $|\Psi_i(\mathbf{Q})|^2$ can be computed using descendant weighting techniques during the same DQMC simulation in which we compute $M_{fi}^{(1)}$. Therefore with a single DQMC simulation, we can compute the transition energies $\Delta E^{(j)}$ and absorption coefficients $\tilde{\alpha}^{(j)}$ for each p-H₂ molecule in the doped crystal.

The simulated spectrum which would result from such a calculation would be a stick spectrum, composed of sharp peaks at the transition energies $\Delta E^{(j)}$ with respective absorption coefficients $\tilde{\alpha}^{(j)}$. The spectra shown in Fig. 2 are clearly not stick spectra; the dopant-induced $Q_1(0)$ features have finite widths. Although vibron hopping in the p-H₂ crystal broadens IR spectral features in solid H₂ [29], recent high-resolution IR studies [7, 15] demonstrate that this effect is relatively weak, and broadens features in the $Q_1(0)$ band only by about 0.1 cm⁻¹. Consequently it is a good approximation to assume that the vibrational excitation remains localized on a single p-H₂ molecule. The widths of the peaks shown in Fig. 2 therefore seem to arise primarily from instrumental broadening; the resolution of the spectrometer used to record these spectra is 1 cm⁻¹. We emphasize that any broadening due to vibron hopping will *not* change the integrated absorption coefficient of the $Q_1(0)$ band; this is a consequence of the principle of spectroscopic stability [27].

4. Studies of Li-doped solid H₂

A. Quantum chemical calculations

The DQMC simulations described above require as input both (1) the potential energy surface $V(\mathbf{Q}, v_1, v_2, \dots, v_N)$ of the doped p-H₂ crystal and (2) induced transition moment functions for Li-p-H₂ and (p-H₂)₂ pairs. We assume that V is pairwise additive, and that the interaction between two $v = 0$ p-H₂ molecules is described by the Silvera-Goldman [22] potential function $V_{\text{SG}}(R)$; this potential includes, in an effective form, three-body contributions to the potential energy which are important in solid H₂. To describe the interaction between a p-H₂ molecule with $v = 0$ and a p-H₂ molecule with $v = 1$, we add to $V_{\text{SG}}(R)$ an incremental contribution obtained from Ref. [19], which is the difference between the $(v_1, v_2) = (0, 0)$ and $(v_1, v_2) = (0, 1)$ potential curves for an isolated gas-phase (p-H₂)₂ dimer.

The Li-(p-H₂) interaction was computed *ab initio* at the counterpoise-corrected CCSD(T) level [26], using aug-cc-pVTZ basis sets on the hydrogen atoms, a truncated cc-pVQZ basis set (which omits g orbitals) on Li, and an uncontracted (3s3p2d) set of bond functions midway between Li and H₂. (Our results did not change significantly when either diffuse functions or tight core-valence functions were added to the Li basis set.) Single point *ab initio* calculations of the Li-H₂ potential energy were performed at 369 geometries using standard Jacobi coordinates; these were averaged over the appropriate H₂ vibrational wavefunction and the isotropic $Y_{00}(\theta, \phi)$ spherical harmonic to obtain Li-(p-H₂) potential curves for a p-H₂ molecule with the vibrational quantum number $v = 0$ or $v = 1$.

The H₂-H₂ induced transition moment function defined in Eq. (6) was taken directly from Ref. [19]. The Li-H₂ induced transition moment function was computed *ab initio* at the CCSD(T) level [26], using d-aug-cc-pVQZ basis sets on the hydrogen atoms and the truncated Li cc-pVQZ basis set described above; no bond functions were employed. Single point *ab initio* dipole moments were obtained at 189 geometries, again using Jacobi coordinates; these dipole moments were averaged over the H₂ vibrational wavefunctions and the isotropic $Y_{00}(\theta, \phi)$ spherical harmonic to obtain the Li-(p-H₂) induced transition moment function defined in Eq. (5).

Figure 4 shows our computed Li-(p-H₂) potential energy and transition moment curves. Vibrational excitation of the p-H₂ molecule strengthens the long-range Li-(p-H₂) attractive dispersion interactions and deepens the potential slightly. A Numerov-Cooley analysis of the Li-(p-H₂) bound states shows that the $v = 0$ and $v = 1$ Li-(p-H₂) curves each support one van der Waals bound state; the energies of these van der Waals complexes are $E = -3.94 \text{ cm}^{-1}$ for $v = 0$ p-H₂ and $E = -5.12 \text{ cm}^{-1}$ for $v = 1$ p-H₂. The first-order

perturbation theory argument outlined previously predicts that the van der Waals bond should be 1.10 cm^{-1} stronger in the $v = 1$ complex. This is in good agreement with the Numerov–Cooley results, which show that vibrational excitation of the p-H₂ molecule strengthens the bond by 1.18 cm^{-1} .

B. DQMC simulations of Li-induced spectral features

We performed DQMC simulations of Li-doped solid p-H₂ using a protocol similar to that employed by Cheng and Whaley [8]. We began with a DQMC simulation “box” containing 180 p-H₂ molecules arranged on the hcp lattice. One p-H₂ molecule was removed from the simulation box and replaced by a Li atom. We then applied periodic boundary conditions in three dimensions and conducted a series of DQMC simulations, using the trial wavefunction Ψ_{tr} defined in Ref. [8] to reduce the statistical fluctuations inherent in DQMC methods and increase the efficiency of our simulations. This trial function consists of a product of Gaussians localizing each particle near its nominal lattice site and two-body Jastrow functions correlating the instantaneous positions of neighboring particles.

Our DQMC simulations are conducted using an imaginary time step of $50 i \text{ au}$ and typically consist of 1000 to 2500 time steps, beginning from a previously equilibrated ensemble of 250 or 500 configurations. During the simulations, we used descendant weighting techniques to evaluate the transition moment $M_{fi}^{(j)}$ and transition energy $\Delta E^{(j)}$ for the twelve p-H₂ molecules which are nearest neighbors to the Li impurity. We note that descendant weighting methods effectively eliminate any trial function bias in the computation of expectation values [5], and are therefore superior to “mixed” estimators of observables which have been widely used in previous studies of solid H₂ [8]. During the first 90% of each DQMC simulation, we accumulated expectation values via descendant weighting.

From ten independent DQMC simulations, we obtained an estimate for the total $Q_1(0)$ transition moment of $M_{fi} = (2.25 \pm 0.14) \times 10^{-3} \text{ au}$ which corresponds to a $Q_1(0)$ integrated absorption coefficient of $\tilde{\alpha} = 4.1 \times 10^{-13} \text{ cm}^3/\text{s}$ per Li impurity. To place this absorption coefficient in context, the $Q_1(0)$ integrated absorption coefficient for the transition induced in solid p-H₂ by the permanent quadrupole moment of o-H₂ impurities (shown in the top spectrum of Fig. 2) is $\tilde{\alpha} = 2.2 \times 10^{-14} \text{ cm}^3/\text{s}$ per o-H₂ impurity. The Li-induced features are thus roughly 18 times stronger than those induced by o-H₂. (Note that the top spectrum of Fig. 2 was taken at an o-H₂ concentration of 2%.)

Figure 5 shows our simulated absorption spectrum for a 1-mm thick sample of solid p-H₂ doped with Li at a concentration of 1000 ppm [14]. This spectrum was obtained from the theoretical transition energies $\Delta E^{(j)}$ and absorption coefficients $\tilde{\alpha}^{(j)}$ of the twelve p-H₂ molecules surrounding the Li dopant; the computed

stick spectrum was convolved with a Gaussian of width 1 cm^{-1} to simulate instrumental broadening. We also show in Fig. 5 the experimental absorption spectrum [11] for Na-doped solid p-H₂, which we have chosen as a chemically similar system for which an experimental lineshape is available.

The comparison between our simulated spectrum for Li-doped p-H₂ and the experimental results for Na-doped p-H₂ is striking. Apart from an overall shift, both spectra have very similar lineshapes. Perhaps most surprising is the fact that the lineshapes are clearly asymmetric, suggesting that either the dopants move to one side of the trapping site or the trapping site undergoes a symmetry-lowering structural transformation. If the Li and Na dopants remained symmetrically distributed in the vacancy created by removing one p-H₂ molecule from the hcp lattice, we would expect to see at most two features in the $Q_1(0)$ band: one from p-H₂ molecules in the same hcp crystal plane as the dopant, and one from p-H₂ molecules in adjacent crystal planes. The experimental spectrum consists of at least three features, however.

The $Q_1(0)$ features induced by Na dopants are red-shifted from our theoretical Li-induced features by about 6 cm^{-1} . The overall shift is controlled by the change ΔV in the potential surface induced upon excitation of a single H₂ molecule [Eq. (14)], which is dominated by the increase in attractive dopant-(p-H₂) dispersion interactions which accompanies H₂ vibrational excitation. If we naively assume that these dispersion interactions vary with the dopant's polarizability, we would expect the Na-induced features to be more highly red-shifted than the Li-induced features.

5. Summary

We have developed computational tools for computing the lineshape and intensity of the $Q_1(0)$ IR spectral features induced in solid p-H₂ crystals by S-state atomic dopants, and have applied these tools to the model HEDM system of Li in solid p-H₂. The integrated absorption coefficient for the H₂ $Q_1(0)$ band for Li-doped solid p-H₂ is computed to be $\tilde{\alpha} = 4.1 \times 10^{-13}\text{ cm}^3/\text{s}$ per Li impurity. Our predicted $Q_1(0)$ lineshape (Fig. 5) contains rich structure which may shed light on the microscopic morphology of Li trapping sites in solid p-H₂; this lineshape agrees very well with the experimental $Q_1(0)$ lineshape [11] for the chemically related system of Na-doped solid p-H₂.

6. References

- [1] P. W. Atkins and R. S. Friedman, *Molecular Quantum Mechanics* (Oxford, New York, 1997).
- [2] T. K. Balasubramanian, R. D'Souza, R. D'Cunha, and K. N. Rao, *J. Mol. Spectrosc.* **153**, 741 (1992).

- [3] R. N. Barnett, P. J. Reynolds, and W. A. Lester, Jr., J. Chem. Phys. **96**, 2141 (1992).
- [4] P. G. Carrick, USAF Technical Report PL-TR-93-3014 (1993).
- [5] J. Casulleras and J. Boronat, Phys. Rev. B **52**, 3654 (1995).
- [6] G. Chaban and M. S. Gordon, J. Phys. Chem. **100**, 95 (1996).
- [7] M.-C. Chan, M. Okumura, C. M. Gabrys, L.-W. Xu, B. D. Rehfuss, and T. Oka, Phys. Rev. Lett. **66**, 2060 (1991).
- [8] E. Cheng and K. B. Whaley, J. Chem. Phys. **104**, 3155 (1996).
- [9] M. E. Fajardo, J. Chem. Phys. **98**, 110 (1993).
- [10] M. E. Fajardo, S. Tam, T. L. Thompson, and M. E. Cordonnier, Chem. Phys. **189**, 351 (1994).
- [11] M. E. Fajardo and S. Tam, J. Chem. Phys. **108**, 4237 (1998).
- [12] H. P. Gush, W. F. J. Hare, E. J. Allin, and H. L. Welsh, Can. J. Phys. **38**, 176 (1960).
- [13] "On the absorption intensity of the $Q_1(0) + Q_1(0)$ and $Q_1(0) + Q_2(0)$ double vibrational transitions in solid parahydrogen", R. J. Hinde, Phys. Rev. B (accepted for publication, 1999).
- [14] R. J. Hinde, unpublished work (October 1999).
- [15] K. E. Kerr, T. Momose, D. P. Weliky, C. M. Gabrys, and T. Oka, Phys. Rev. Lett. **72**, 3957 (1994).
- [16] A. R. W. McKellar and H. L. Welsh, Can. J. Phys. **52**, 1082 (1974).
- [17] A. R. W. McKellar, J. Chem. Phys. **92**, 3261 (1990).
- [18] M. Mengel, B. P. Winnewisser, and M. Winnewisser, J. Mol. Spectrosc. **188**, 221 (1998).
- [19] W. Meyer, A. Borysow, and L. Frommhold, Phys. Rev. A **40**, 6931 (1989).
- [20] J. D. Poll and J. Van Kranendonk, Can. J. Phys. **40**, 163 (1962).
- [21] V. F. Sears and J. Van Kranendonk, Can. J. Phys. **42**, 980 (1964).

- [22] I. Silvera and V. V. Goldman, *J. Chem. Phys.* **69**, 4209 (1978).
- [23] I. F. Silvera, *Rev. Mod. Phys.* **52**, 393 (1980).
- [24] G. P. Sutton, *Rocket Propulsion Elements* (Wiley-Interscience, New York, 1986).
- [25] S. Tam, M. Macler, and M. E. Fajardo, *J. Chem. Phys.* **106**, 8955 (1997).
- [26] B. K. Taylor and R. J. Hinde, unpublished work (August 1999).
- [27] J. Van Kranendonk, *Can. J. Phys.* **38**, 240 (1960).
- [28] J. Van Kranendonk and H. P. Gush, *Phys. Lett.* **1**, 22 (1962).
- [29] J. Van Kranendonk, *Solid Hydrogen* (Plenum, New York, 1983).

7. Figure captions:

Fig. 1. Visible transmission spectrum of Li-doped solid H_2 . The dashed line is the spectrum of a sample of Li in solid H_2 at a concentration of approximately 20 ppm and at $T = 3.4$ K; the dotted-dashed line is the spectrum of pure solid H_2 at $T = 3.4$ K. The solid curve is the difference spectrum. The sample thickness is estimated to be roughly $10\ \mu\text{m}$. Reprinted from Ref. [9].

Fig. 2. Infrared absorption peaks induced in solid p-H_2 samples by various atomic and molecular dopants. The temperature of each sample is $T = 2$ K; the sample thicknesses range from 1 to 3 mm. Except for o-H_2 dopants (top spectrum), the estimated dopant concentrations range from 100 to 1000 ppm. Reprinted from Ref. [11].

Fig. 3. Illustration of the cancellation effect in hcp solid p-H_2 . The open circles represent $v = 0$ p-H_2 molecules; the filled circle represents a $v = 1$ p-H_2 molecule. The vibrationally excited molecule induces pairwise dipole moments with its neighbors (arrows), but these moments sum to zero due to the symmetry of the hcp crystal lattice.

Fig. 4. *Ab initio* Li-(p-H_2) potential energy curves (upper panel) and $Q_1(0)$ transition moment (lower panel); see the text for computational details. In the upper panel, the solid line indicates $v = 0$ p-H_2 and the dashed line indicates $v = 1$ p-H_2 .

Fig. 5. Theoretical spectrum for the Li-induced H_2 $Q_1(0)$ band in Li-doped solid p- H_2 (lower spectrum) compared with the experimental spectrum for the Na-induced H_2 $Q_1(0)$ band in Na-doped solid p- H_2 (upper spectrum, taken from Ref. [11]). The simulated Li-induced spectrum corresponds to a 1-mm thick sample of Li-doped solid H_2 with a Li concentration of 1000 ppm; the absorbance scale for this spectrum is absolute. The experimental Na-induced spectrum is for a sample about 1-mm thick with an estimated Na concentration of 100 to 1000 ppm; the absorbance scale for this spectrum is *not* the same as for the simulated Li-induced spectrum.

Fig. 1

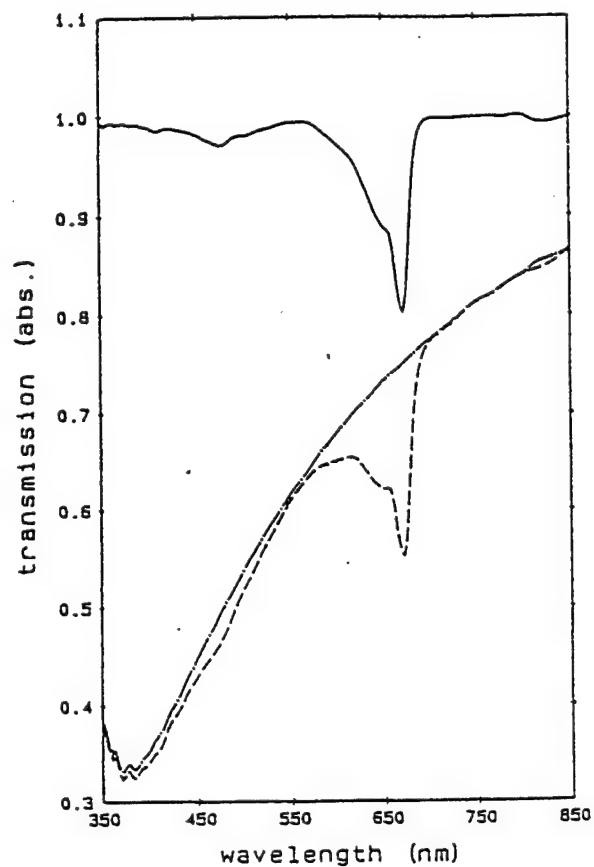


Fig. 2

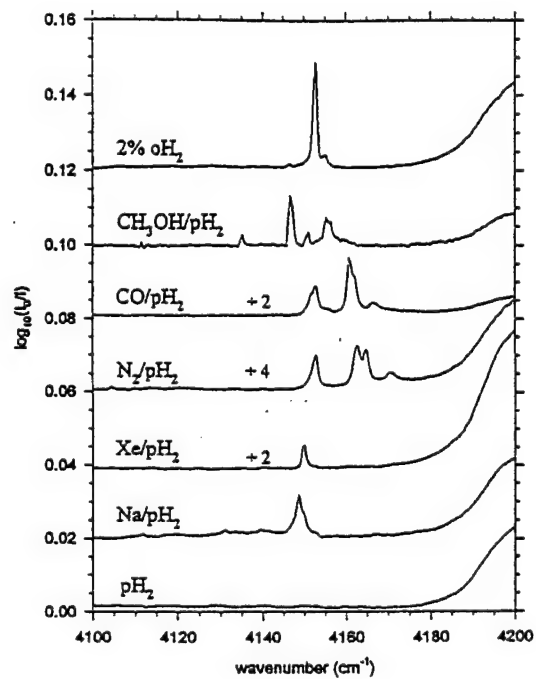


Fig. 3

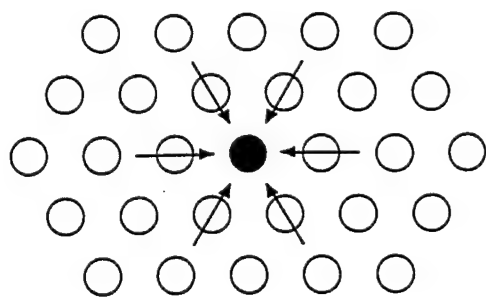


Fig. 4

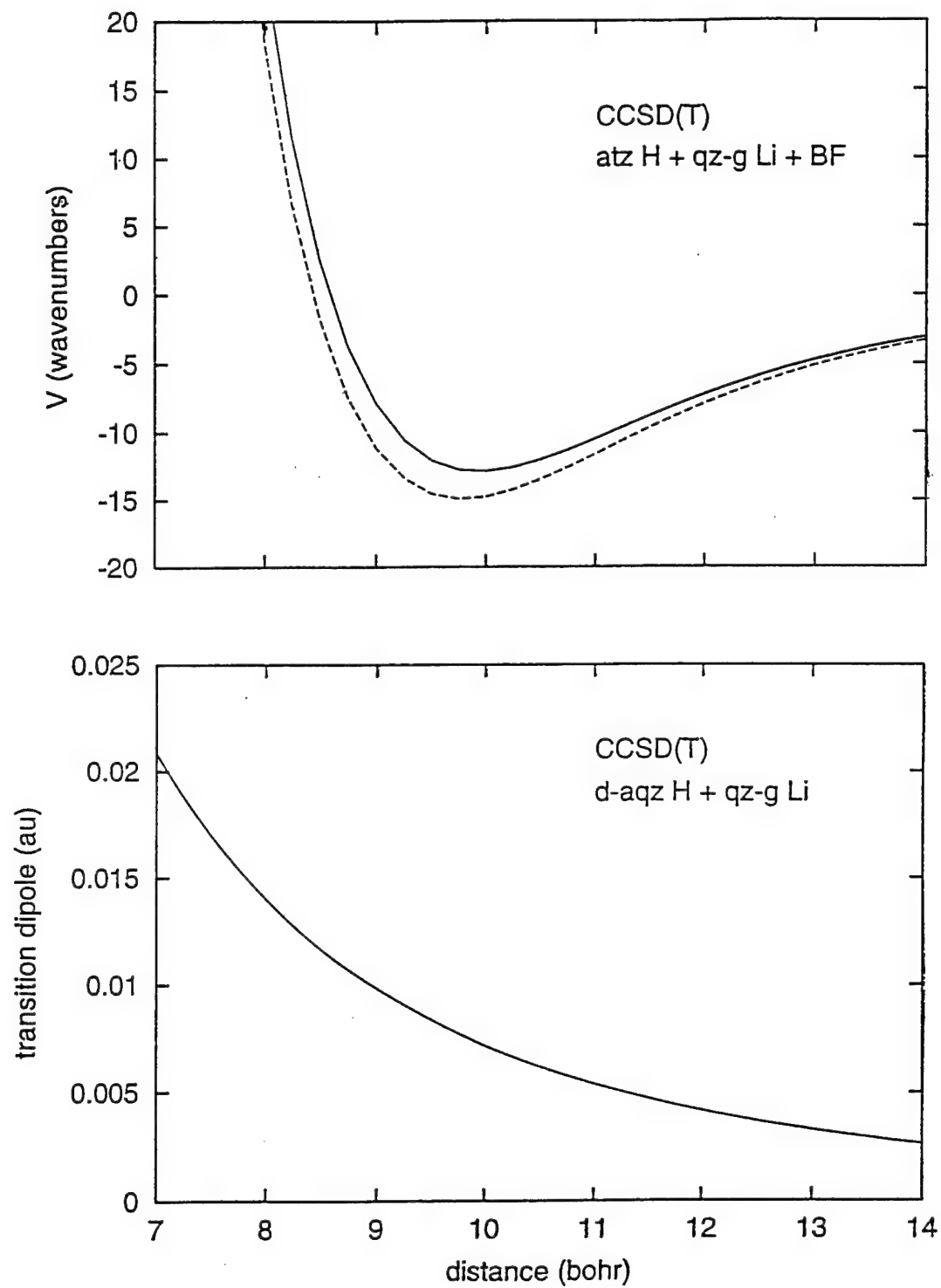
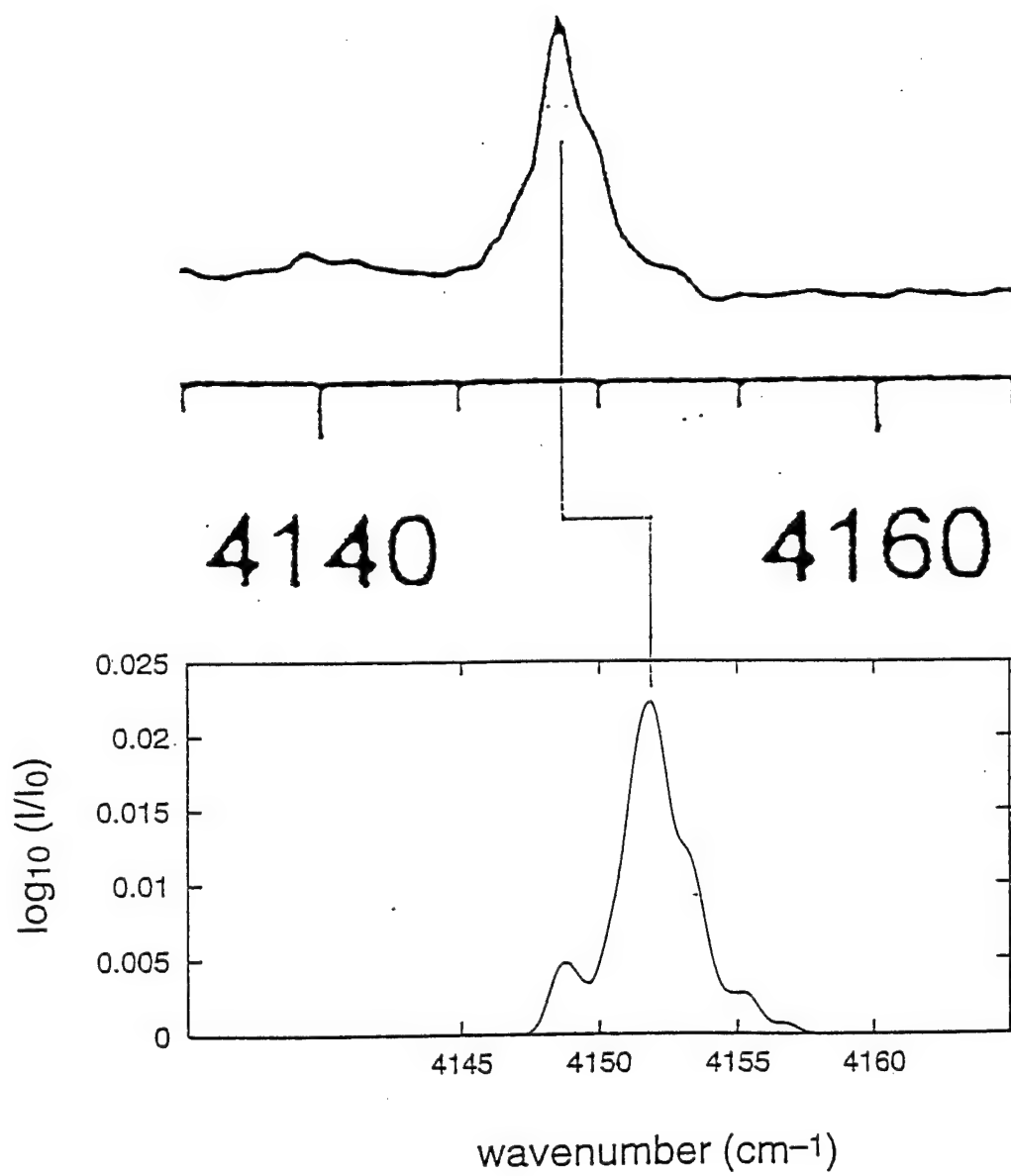


Fig. 5



ALGEBRAIC METHODS FOR IMPROVED BLIND RESTORATION OF ADAPTIVE OPTICS IMAGES OF SPACE OBJECTS

Brian D. Jeffs
Associate Professor
Department of Electrical and Computer Engineering

Brigham Young University
459 CB, Provo, UT 84602, USA.
E-mail: bjeffs@ee.byu.edu

Final Report for the
Summer Research Extension Program
Subcontract No. 99-0828, Contract No. F49620-93-C-0063

Sponsored by:
Air Force Office of Scientific Research
Bolling Air Force Base, DC

and

AFRL

December 1999

ALGEBRAIC METHODS FOR IMPROVED BLIND RESTORATION OF ADAPTIVE OPTICS IMAGES OF SPACE OBJECTS

Brian D. Jeffs

Associate Professor

Department of Electrical and Computer Engineering
Brigham Young University

Abstract

Blind point-source image restoration refers to the problem of high resolution recovery of point-like sources which are blurred by an unknown point spread function (psf) and corrupted by noise. Applications include astronomical star field localization, airborne target image localization, magnetoencephalogram brain current imaging, and seismic deconvolution. Both single and multiple frame observation cases are addressed, with an emphasis on adaptive optics (AO) telescope data sets. This final report describes two methods for solving this problem which were developed under AFOSR SREP grant support. First, it will be shown that with suitable constraints, the problem can be cast in the language of subspace decomposition as used in blind signal copy algorithms for digital wireless communications. Assuming a separable psf, we propose a deterministic, non-iterative ESPRIT-like solution to the restoration problem. This algorithm is then extended to apply to non-separable psf's by approximating them as a series expansion of a few separable components.

The second algorithm introduced in this report is a Bayesian method for blind restoration of images of sparse, point-like objects. The proposed method uses maximum *a posteriori* estimation techniques to recover both the unknown object and blur. Markov random field (MRF) models are used to represent prior information about both the sparse, point-like structure of the object, and the smoothed random structure of the blur. As compared with general purpose blind algorithms, incorporating a sparse point source MRF model enables much higher resolution restorations, improves point localization, and aids in overcoming the convolutional ambiguity in the blind problem

Contents

1	Introduction	4
2	Subspace Decomposition Methods for Blind Point Source Restoration	5
2.1	Restoration with Separable Blur	6
2.1.1	The Optimal Solution	8
2.1.2	A Suboptimal Solution	8
2.2	Non-Separable Blurring Functions	9
2.3	Results for the Subspace Approach	12
3	Bayesian Methods for Blind Point Source Image Restoration	13
3.1	Problem Formulation	15
3.2	Results for Bayesian Blind Point Source Restoration	19
4	Conclusions	21
4.1	Additional Accomplishments Supported by the SREP Grant	23

ALGEBRAIC METHODS FOR IMPROVED BLIND RESTORATION OF ADAPTIVE OPTICS IMAGES OF SPACE OBJECTS

Brian D. Jeffs¹

1 Introduction

This document is the final report of progress made during calendar year 1999 under the AFOSR Summer Research Extension Program, Subcontract No. 98-0813. Participants include Dr. Brian D. Jeffs of Brigham Young University as principal investigator, and graduate students Brent Chipman and Lisha Li. This work was accomplished in collaboration with Dr. Robert Q. Fugate and Dr. Julian C. Christou of the Starfire Optical Range, Air Force Research Laboratories, Kirtland Air Force Base, New Mexico.

The focus of this research program is algorithm development for blind image restoration of multiframe adaptive optics (AO) telescope images. In particular, methods of primary interest are those algorithms capable of removing residual blur from point-source images acquired using the SOR ground based 1.5m and 3.5m AO telescope systems. Previous AFOSR supported work with Starfire Optical Range emphasized blind restoration of AO images of satellites. The restoration algorithms used imaging models which exploited the known man-made structure of the true satellite image in order to achieve higher resolution restorations which better recovered the sharp edges and geometric structures of satellites. The work reported here extends these ideas to the case of blurred point-like images, such as AO images of star fields where separately resolving and localizing distinct stars which have been blurred together is the goal. These blind restorations are achieved by exploiting the known point-like image structure into the restoration algorithm, so that point-like results are favored. Two new methods for this class of image restoration problems were developed, and are reported here. The first method yields a closed-

¹Sponsored by the Air Force Office of Scientific Research, Bolling Air Force Base, DC. The author acknowledges the contributions to this work from Dr. Julian C. Christou and Dr. Robert Fugate, Starfire Optical Range, Air Force Research Laboratory. Also, Mr. Brent Chipman contributed much to this work while a graduate student at Brigham Young University.

form algebraic solution based on subspace decomposition techniques. The second method is based on Bayesian estimation theory with a statistical model for the sparse image field employed as prior information.

2 Subspace Decomposition Methods for Blind Point Source Restoration

In this section we assume one frame of blurred observation data is available with no knowledge of the blurring psf. The underlying true image is assumed to be sparse, consisting of a relatively small number of discrete point-like objects (e.g. stars) with unknown intensity, and position. We will also assume the unknown blur is severe enough to in some cases eliminate distinct intensity peaks associated with adjacent points.

Array processing algorithms, like ESPRIT [1] and MUSIC, have been used to solve related problems because they inherently deal with point sources. Recently the MUSIC algorithm was used to restore point-source images with known blur [2]. In this paper, we propose an ESPRIT-like algorithm for restoration with unknown blur. The method is non-iterative, deterministic, and operates on a single image frame with unknown blur. This formulation requires the fairly stringent constraint that the blurring psf be separable along perpendicular axes. This type of blur, however, is not unrealizable. Long exposure atmospheric turbulence blur has been shown to be approximately circularly Gaussian, which is always separable.

An application of particular interest to us is blind restoration of adaptive optics (AO) telescope images of star fields. The AO system removes much of the atmospheric-turbulence-induced blurring, but a residual random, unknown blur remains. The general structure of the blur is known to be Lorentzian [3], which is well approximated by the sum of two Gaussian blurs. With this motivation we study images blurred by non-separable psf's which can be approximated with a finite series expansion sum of separable blurs. A method is introduced for separately estimating the x and y positions of the point sources in the non-separable case.

The assumed model for the input image, a point-like scene with d sources, is

$$f(x, y) = \sum_{k=1}^d a_k \delta(x - x_k) \delta(y - y_k). \quad (1)$$

The k^{th} point source has amplitude a_k and position (x_k, y_k) . The observed image is given by

$$g(x, y) = h(x, y) * f(x, y) + \eta(x, y). \quad (2)$$

Here the symbol ‘ $*$ ’ signifies two dimensional convolution, $h(x, y)$ is the spatial domain psf, and $\eta(x, y)$ is additive noise. The problem at hand is to estimate point-source position pairs, (x_k, y_k) , and their associated amplitudes.

2.1 Restoration with Separable Blur

For a separable blur, $h(x, y) = h_x(x)h_y(y)$. Assuming that the output data is available in a sampled representation, $g[m, n]$, the two-dimensional discrete Fourier transform of the output can be written as $g(\xi, \zeta)$, where ξ and ζ represent the x and y spatial frequency variables respectively. Sampling this 2-D DFT with N spatial frequency samples along each axis, $\xi_i = \zeta_i = \frac{2\pi(i-1)}{N}$ with $i = 1 \cdots N$, leads to a matrix representation of the frequency domain data: $\mathbf{G}_{i,j} = g(\xi_j, \zeta_i)$. Incorporating equations (1) and 2) into this sampled frequency domain model yields the following matrix representation,

$$\begin{aligned} \mathbf{G} &= \mathbf{H}_y \mathbf{V}(\mathbf{y}) \mathbf{A} \mathbf{V}^T(\mathbf{x}) \mathbf{H}_x^T, \text{ where} \\ \mathbf{H}_y &= \text{Diag}\{[h_y(\zeta_1), \dots, h_y(\zeta_N)]^T\}, \\ \mathbf{V}(\mathbf{y}) &= [\mathbf{v}(y_1) \cdots \mathbf{v}(y_d)], \\ \mathbf{v}(y_k) &= [e^{-j\zeta_1 y_k} \dots e^{-j\zeta_N y_k}]^T, \\ \mathbf{A} &= \text{Diag}\{[a_1, \dots, a_d]^T\}. \end{aligned} \quad (3)$$

and where $\text{Diag}\{\mathbf{x}\}$ indicates a diagonal matrix formed from vector \mathbf{x} . \mathbf{H}_x , $\mathbf{V}(\mathbf{x})$, and $\mathbf{v}(x_k)$ are defined similarly. Note that the k^{th} element of \mathbf{x} , x_k , is linked to corresponding element y_k of \mathbf{y} in specifying x and y positions of a single source point.

Following the development of Swindlehurst and Gunther (which they used for blind resolution of overlapping echoes in digital communications) [4], we compute the singular value decomposition $\mathbf{G} = \mathbf{U}\mathbf{S}\mathbf{V}^H$, where \mathbf{U} and \mathbf{V} are $N \times d$ and \mathbf{S} is $d \times d$. In the noiseless case, signal subspace matrices are defined as

$$\mathbf{E}_y = \mathbf{U}\mathbf{S}^{1/2}, \text{ and } \mathbf{E}_x = \bar{\mathbf{V}}\mathbf{S}^{1/2}, \quad (4)$$

where $\bar{\mathbf{V}} = \text{conj}(\mathbf{V})$. These matrices can be related to the model in the following fashion

$$\begin{aligned} \mathbf{E}_y &= \mathbf{H}_y \mathbf{V}(\mathbf{y}) \mathbf{A}^{1/2} \mathbf{T} \\ \mathbf{E}_x &= \mathbf{H}_x \mathbf{V}(\mathbf{x}) \mathbf{A}^{1/2} (\mathbf{T}^T)^{-1}, \end{aligned} \quad (5)$$

where \mathbf{T} is some unknown full rank matrix. Let us define $\mathbf{V}_1(\mathbf{x})$ as the first $N - \delta$ rows of $\mathbf{V}(\mathbf{x})$ and $\mathbf{V}_2(\mathbf{x})$ as the last $N - \delta$ rows of $\mathbf{V}(\mathbf{x})$. This is equivalent to selecting two shifted sensor sub-arrays in ESPRIT based direction of arrival estimation. Since the \mathbf{V} matrices are Vandermonde, $\mathbf{V}_2(\mathbf{x}) = \mathbf{V}_1(\mathbf{x})\Phi_x$ where

$$\Phi_x = \text{Diag} \left[1, e^{-j2\pi\delta x_2/N}, \dots, e^{-j2\pi\delta x_d/N} \right]. \quad (6)$$

Similarly defining 1 and 2 matrices for \mathbf{H}_x , \mathbf{H}_y , \mathbf{E}_x , \mathbf{E}_y , and $\mathbf{V}(\mathbf{y})$ leads to the following relations:

$$\begin{aligned} \mathbf{H}_{y,1}\mathbf{E}_{y,2} &= \mathbf{H}_{y,2}\mathbf{E}_{y,1}\Psi_y, \\ \Psi_y &= \mathbf{T}^{-1}\Phi_y\mathbf{T}, \end{aligned} \quad (7)$$

$$\begin{aligned} \mathbf{H}_{x,1}\mathbf{E}_{x,2} &= \mathbf{H}_{x,2}\mathbf{E}_{x,1}\Psi_x^T, \\ \Psi_x &= \mathbf{T}^{-1}\Phi_x\mathbf{T}. \end{aligned} \quad (8)$$

This observation implies two equivalent constraints on the solution. First, Ψ_x and Ψ_y must have an equivalent set of eigenvectors and second, Ψ_x and Ψ_y must commute.

2.1.1 The Optimal Solution

An optimal solution to this problem (in the least squares sense) can be defined as the solution to a constrained minimization problem. First, the following definitions are made

$$\Delta_y = \mathbf{H}_{y,2}^{-1} \mathbf{H}_{y,1}, \text{ and } \Delta_x = \mathbf{H}_{x,2}^{-1} \mathbf{H}_{x,1}. \quad (9)$$

The solution is

$$\begin{aligned} \hat{\Delta}_y, \hat{\Delta}_x, \hat{\Psi}_y, \hat{\Psi}_x = \\ \arg \min_{\Delta_{y,x}, \Psi_{y,x}} \left\| \begin{bmatrix} \Delta_y \mathbf{E}_{y,2} \\ \Delta_x \mathbf{E}_{x,2} \end{bmatrix} - \begin{bmatrix} \mathbf{E}_{y,1} \Psi_y \\ \mathbf{E}_{x,1} \Psi_x^T \end{bmatrix} \right\|_F^2 \end{aligned} \quad (10)$$

subject to the constraint

$$\text{eig}\{\Psi_y\} = \text{eig}\{\Psi_x\}, \text{ or } \Psi_x \Psi_y - \Psi_y \Psi_x = 0, \quad (11)$$

where $\text{eig}\{A\}$ denotes the matrix of eigenvectors of A . Once the Ψ_x and Ψ_y matrices are known, the position estimates are given by

$$x_i = \frac{N \angle \lambda_{x,i}}{2\pi\delta}, \quad y_i = \frac{N \angle \lambda_{y,i}}{2\pi\delta} \quad (12)$$

where $\lambda_{x,i}$ and $\lambda_{y,i}$ are the i^{th} eigenvalues of Ψ_x and Ψ_y respectively.

2.1.2 A Suboptimal Solution

Though the solution presented above is optimal, it is difficult to compute the joint minimization of equation (10). The following suboptimal approach performs the minimizations sequentially. Ignoring the constraint, it is easy to solve for Ψ_y and Δ_y [4],

$$\hat{\delta}_y = \arg \min_{\delta_y} \delta_y^H \left[\mathbf{P}_{E_{y,1}}^\perp \odot (\mathbf{E}_{y,2} \mathbf{E}_{y,2}^H)^T \right] \delta_y \quad (13)$$

where $\delta = \text{diag}(\Delta)$ is the vector extracted from the diagonal of Δ , \mathbf{P} denotes a projection matrix with respect to the subscript, and \odot denotes a Schur matrix product. Using $\hat{\Delta} = \text{Diag} \hat{\delta}$ yields

$$\hat{\Psi}_y = (\mathbf{E}_{y,1}^H \mathbf{E}_{y,1})^{-1} \mathbf{E}_{y,1}^H \hat{\Delta}_y \mathbf{E}_{y,2}. \quad (14)$$

The estimate for \mathbf{T} is $\hat{\mathbf{T}} = \text{eig}\{\hat{\Psi}_y\}^{-1}$. Δ_x and Φ_x are then estimated as

$$\hat{\Delta}_x, \hat{\Phi}_x = \arg \min_{\Delta_x, \Phi_x} \left\| \Delta_x \mathbf{E}_{x,2} \hat{\mathbf{T}}^T - \mathbf{E}_{x,1} \hat{\mathbf{T}}^T \Phi_x \right\|_F^2 \quad (15)$$

With a little algebra and calculus, it can be shown [5] that equation (15) is equivalent to

$$\begin{aligned} \hat{\delta}_x &= \mathbf{C}^{-1} \mathbf{D} \phi_x, \text{ and} \\ \hat{\phi}_x &= \arg \min_{\phi_x} \phi_x^H (\mathbf{E} - \mathbf{D}^H \mathbf{C}^{-1} \mathbf{D}) \phi_x \end{aligned} \quad (16)$$

where $\phi_x = \text{diag}(\Phi_x)$, $\delta_x = \text{diag}(\Delta_x)$, $\mathbf{E} = \mathbf{I} \odot \mathbf{R}^H \mathbf{R}$, $\mathbf{C} = \mathbf{I} \odot (\mathbf{Q} \mathbf{Q}^H)^T$, $\mathbf{D} = \mathbf{R} \odot \bar{\mathbf{Q}}$, $\mathbf{Q} \stackrel{\text{def}}{=} \mathbf{E}_{x,2} (\hat{\mathbf{T}})^T$, and $\mathbf{R} \stackrel{\text{def}}{=} \mathbf{E}_{x,1} (\hat{\mathbf{T}})^T$. It is easy to solve for ϕ_x with a singular value decomposition. x_i positions are computed directly from $\hat{\phi}_x$ using equation (6), and $\hat{\delta}_x$ is used to estimate \mathbf{H}_x . The point source y positions are similarly computed by switching the roles of x and y in the derivation above.

2.2 Non-Separable Blurring Functions

When $h(x, y)$ is not separable, the above method fails, which limits use of the algorithm to a specific class of images. This section introduces a method that works with non-separable blurs. Suppose we have a point-source image that is blurred by a psf with exactly p separable components, i.e. $h(x, y) = \sum_{i=1}^p h_{yi}(x) h_{xi}(y)$. Note that for sampled images, such a finite series expansion of the blur into separable components is always possible by letting $h_{yi}(m)$ and $h_{xi}(n)$ be the Fourier basis functions. The received image can be modeled as

$$g(x, y) = \sum_{k=1}^d \sum_{i=1}^p a_k h_{xi}(x - x_k) h_{yi}(y - y_k) \quad (17)$$

Taking a 1-D DFT of the columns and taking N samples as before yields

$$\mathbf{G}_y = \sum_{i=1}^p \mathbf{H}_{yi} \mathbf{V}(\mathbf{y}) \mathbf{A}_{yi} + \mathbf{N}_y. \quad (18)$$

Each of the separable components are of rank d , so the total rank in the noise free \mathbf{G}_y must be $q < pd$. Letting \mathbf{E} be the first q singular vectors from the SVD of \mathbf{G}_y leads to

$$[\mathbf{H}_{y1} \mathbf{V}(\mathbf{y}) | \cdots | \mathbf{H}_{yp} \mathbf{V}(\mathbf{y})] \in \text{span}\{\mathbf{E}\}. \quad (19)$$

Thus for each i there exists a $q \times d$ matrix \mathbf{T}_i such that

$$\mathbf{E} \mathbf{T}_i = \mathbf{H}_{yi} \mathbf{V}(\mathbf{y}). \quad (20)$$

This can be recast into the least squares problem

$$\hat{\mathbf{H}}_{yi}, \hat{\mathbf{T}}_i, \hat{\mathbf{y}} = \arg \min_{\mathbf{H}, \mathbf{T}, \mathbf{y}} \|\mathbf{H}_{yi} \mathbf{V}(\mathbf{y}) - \mathbf{E} \mathbf{T}_i\|_F^2. \quad (21)$$

Using the sub-optimal sequential estimation approach to solve for \mathbf{T}_i first gives

$$\hat{\mathbf{T}}_i = (\mathbf{E} \mathbf{E}^H)^{-1} \mathbf{E}^H \hat{\mathbf{H}}_{yi} \mathbf{V}(\mathbf{y}). \quad (22)$$

Reinserting this solution into equation (21) yields

$$\hat{\mathbf{H}}_{yi}, \hat{\mathbf{y}} = \arg \min_{\mathbf{H}, \mathbf{y}} \left\| \mathbf{P}_E^\perp \mathbf{H}_{yi} \mathbf{V}(\mathbf{y}) \right\|_F^2, \quad (23)$$

which can be expanded in exactly the same manner as the previous section's solution for δ to obtain

$$\hat{\mathbf{h}}_{yi}, \hat{\mathbf{y}} = \arg \max_{\mathbf{h}, \mathbf{y}} \mathbf{h}_{yi}^H \boldsymbol{\Theta}(\mathbf{y}) \mathbf{h}_{yi}, \quad (24)$$

where

$$\boldsymbol{\Theta}(\mathbf{y}) = (\mathbf{E} \mathbf{E}^H) \odot (\mathbf{V}(\mathbf{y}) \mathbf{V}^H(\mathbf{y}))^T. \quad (25)$$

If the vectors \mathbf{h}_{yi} are constrained to be of unit magnitude, the maximum value of the quadratic form in equation (24) will be λ_{max} , the maximum eigenvalue of $\Theta(\mathbf{y})$. Thus, regardless of the values of the true \mathbf{h}_{yi} vectors, the solution for positions can be expressed independent of the unknown blur with the following reformulation

$$\hat{\mathbf{y}} = \arg \max_{\mathbf{y}} \{ \max \text{eigval} (\Theta(\mathbf{y})) \} . \quad (26)$$

This appears to be a daunting equation to solve numerically. At first glance it seems as though there is no hope without an exhaustive search over the d dimensional parameter space in \mathbf{y} , (i.e. compute $\Theta(\mathbf{y})$ for all possible configurations of d points positioned along the y axis, calculating eigenvalues at each step.) It is possible however to solve the problem with at most 2 scans over a one dimensional parameter space by exploiting underlying structure.

While equation (20) holds for the vector \mathbf{y} consisting of all d of the y positions for point sources, it also holds for a shorter \mathbf{y} containing at least two elements (points). Correspondingly, equation (26) will achieve maxima for any size vector \mathbf{y} as long as all the specified positions match some subset of points in truth image $f(x, y)$. In particular, if only two points are chosen, the largest eigenvalue of $\Theta(\mathbf{y})$ will achieve a local maximum whenever the two y parameters are separated by any distance which exists between some actual point-source pair. We note that in any truly blind restoration, only relative distance between features can be recovered. Absolute position is irrelevant because global shifts with respect to a reference frame can also be interpreted as arising from a non-centralized blur psf.

For example, consider an image with 5 points located at positions $y = \{10, 20, 25, 37, 39\}$. The set of all pairwise differences in position is $\{2, 5, 10, 12, 14, 15, 17, 19, 27, 29\}$. Defining a two point position vector as $\mathbf{y} = [0, y]^T$, turns equation (26) into the following 1-D optimization problem in y

$$f(y) = \max \text{eigval}(\Theta(\mathbf{y})). \quad (27)$$

The plot of f as a function of y is called the *difference scan*, which will manifest peaks at each legitimate difference. It is possible to reduce the computation by appealing to a lemma found in [4] whereby we can reduce the matrix $\Theta(\mathbf{y})$ to a size of $q \times q$, which is smaller than an $N \times N$.

Armed with the difference scan, we can obtain a solution for the position estimates. The two

points that are separated by the maximum difference are uniquely determined. To prove this property, assume there are two sets of point pairs, (y_1, y_2) and (y_3, y_4) , which are separated by the same (maximum) distance, D_{max} . For this condition

$$y_2 - y_1 = D_{max}, \text{ and } y_4 - y_3 = D_{max}. \quad (28)$$

If $y_1 \leq y_3 \leq y_2$ then clearly $y_4 - y_1 > D_{max}$ which violates the premise that D_{max} was the maximum difference. The other possible relative position cases lead to a similar conclusion. Therefore, the local peak in equation (27) corresponding to the largest y value localizes the unique point pair distance D_{max} . With this first pair separation uniquely determined, each other position can be uniquely determined between them. Now, define the single parameter point triple

$$\mathbf{y} = [0, D_{max}, y]^T, \quad (29)$$

and the solution spectrum, $f(y)$, will have unique peaks at all correct positions, including 0 and D_{max} , when scanning the single scalar parameter y .

2.3 Results for the Subspace Approach

The first example shown in Figure 1 is for the separable blur method. The observed image contains six stars convolved with a circularly symmetric Gaussian blurring function with a standard deviation of 3.5 pixels. Two sets of stars are very much blurred together. The top left frame shows the blurred data with white Gaussian noise added at a level of 40 dB peak SNR. The top right frame shows the position estimates as asterisks, and the correct positions as diamonds. These results are obtained with the y positions estimated without regard to the constraint of equation (11). The bottom left image shows the converse case, where estimates of the x positions do not include the constraint. Note that position estimates are quite accurate (average error less than two pixels), which is remarkable given the noise level and complete lack of knowledge about the blur, $h(x, y)$, other than that it is separable.

The second example shown in Figure 2 illustrates the non-separable method. The same input image is used, except this time the blur is a non-separable Lorentzian function. The top left frame shows the blurred image, while the top right shows the input image itself. Note that the

this truth image corresponds to a smaller window centered on the blurred points in the observed image, and is thus presented at a lower resolution scale. The bottom two graphs are the solution spectra for the y and x positions respectively. We see that the peaks of the spectra indeed correspond to the actual positions represented in the input image.

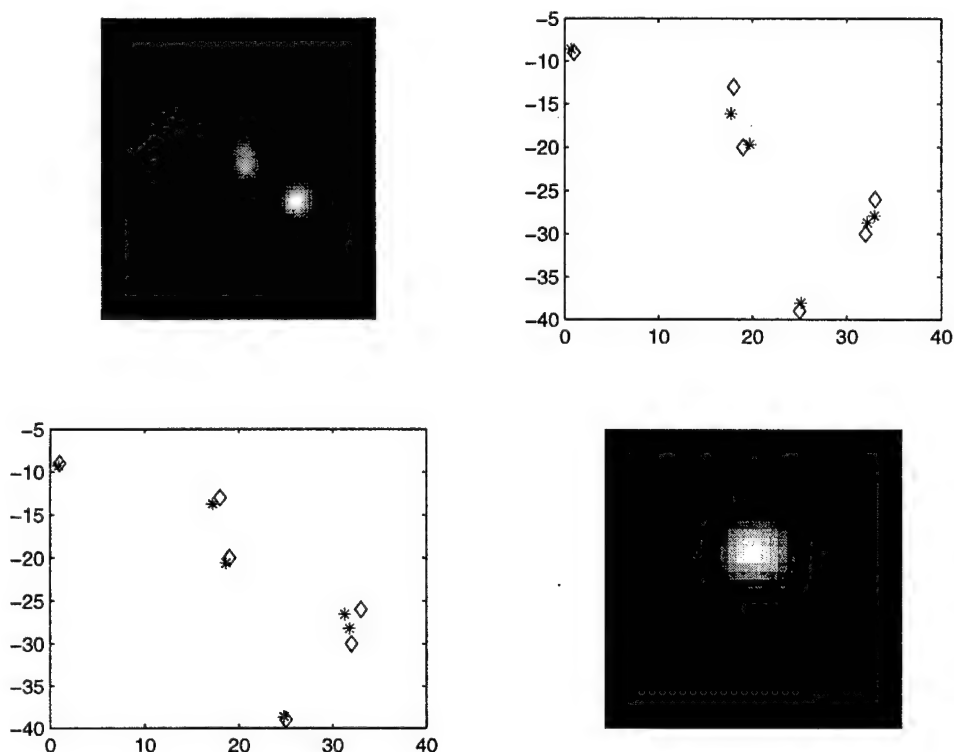


Figure 1: Six star example at PSNR=40 dB. Top left: Blurred, noisy output. Top right: Position estimates with y fixed. Bottom left: Position estimates with x fixed. Bottom right: Blur estimate.

3 Bayesian Methods for Blind Point Source Image Restoration

In this section we present a Bayesian estimation theory based approach for solving the blind multiframe point-source image restoration problem. We assume one or more frames of blurred observation data are available with no knowledge of the blurring psf, and that blur psf's may be different from frame to frame if multiple observations are available

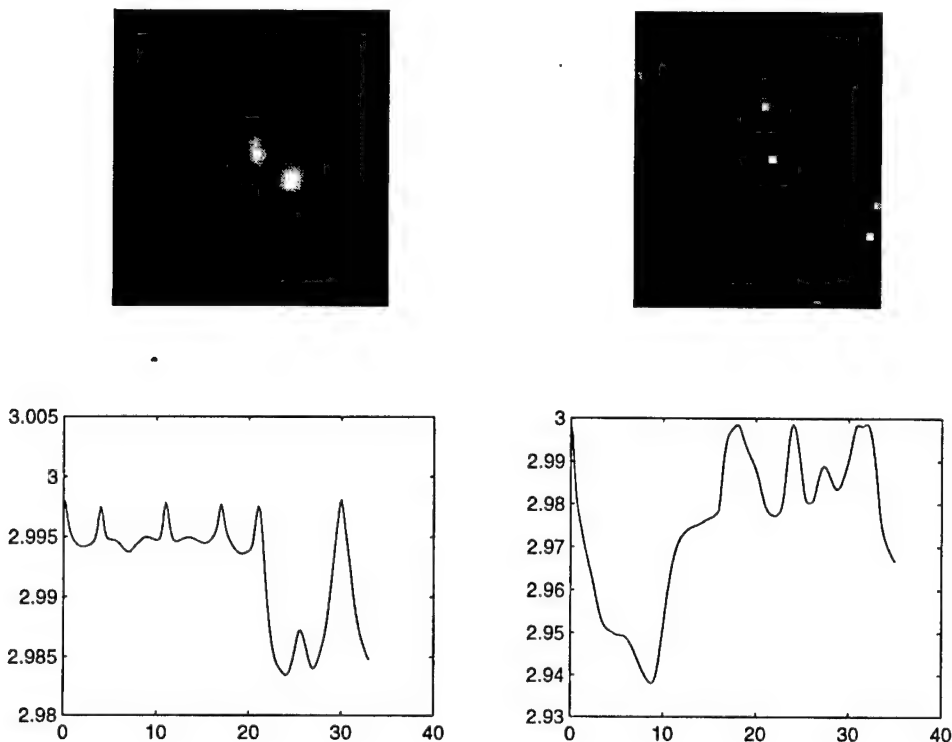


Figure 2: Six star example 200 dB. Top left: Blurred, noisy image. Top right: Truth image. Bottom left: y positions solution spectrum. Bottom right: x position solution spectrum.

An application of particular interest to us is blind restoration of adaptive optics (AO) telescope image sequences of star fields. The AO system removes much of the atmospheric turbulence induced blurring, but a residual random, unknown blur remains that changes from frame to frame in an image sequence over a period of milliseconds. Though the gross structure of the blur is known on average [6], the specific form of each individual blur cannot be easily ascertained, and is thus best modeled with the MRF approach, proposed in this paper. Identifying individual stars in dense star clusters, forming accurate photometry estimates, and computing star-positions to sub-pixel accuracy are primary goals. For example, precise measurement of relative positions can help identify the “wobble” associated with stars orbited by massive planets. This situation lends itself well to the blind restoration technique presented in this paper.

Bayesian maximum a posteriori (MAP) estimation has been shown to be effective in blind restoration. In particular, Jeffs, Hong, and Christou [7] have recently demonstrated the effectiveness of generalized Gauss Markov random fields (GGMRF) in blind restoration of extended

objects. Here both the source and blur were modeled as GGMRF's which have a parametric form allowing a great variety of image representations, including hard edged fields typical of real images and smooth fields typical of blurring point spread functions. However, the GGMRF model is not well suited to point-like sparse images. A Markov random field model which favors sparse solutions is essential if high resolution restorations and accurate point localizations are to be achieved, particularly in the blind case. The ability to exploit known structure in the problem and impose a sparse form on the solution is essential in overcoming convolutional ambiguity in the blind problem. Blind restoration is a highly ill-posed inverse problem, and algorithms which incorporate known image structure in solutions will invariably perform better.

Phillips and Leahy [8], have presented an MRF model that exploits the sparse nature of point source input images in the context of MEG-based imaging. Their model involves a dual field representation: first, a binary activity process determines which pixels have non-zero amplitudes, then a Gaussian amplitude process represents active point intensity levels. We demonstrate that this model can be effectively extended to the *blind* point source restoration case. In fact, the prior information provided by this sparse model image prior pdf is the key to overcoming inherent ambiguity when blur psf's are unknown.

3.1 Problem Formulation

We adopt the following image observation model for both single and multiple frame data representation

$$\begin{aligned}\bar{\mathbf{g}} &= \mathcal{H}\mathbf{f} + \bar{\boldsymbol{\eta}} \\ \bar{\mathbf{g}} &= [\mathbf{g}_1, \mathbf{g}_2, \dots, \mathbf{g}_M]^T, \bar{\boldsymbol{\eta}} = [\boldsymbol{\eta}_1, \boldsymbol{\eta}_2, \dots, \boldsymbol{\eta}_M]^T \\ \mathcal{H} &= [\mathbf{H}_1^T, \dots, \mathbf{H}_M^T]^T\end{aligned}\tag{30}$$

where M is the number of frames, \mathbf{g}_i , \mathbf{f} , and $\boldsymbol{\eta}_i$ are vectors formed by column scanning the 2-D images of the i^{th} observation frame, the true image, and the i^{th} noise frame respectively. \mathbf{H}_i , is the doubly block Toeplitz convolution matrix formed from the i^{th} frame psf, h_i . $\bar{\mathbf{g}}$ is the extended vector formed by concatenating all M column scanned observation frames, and \mathcal{H} represents all M distinct frame blur psf's as a single system matrix. This formulation also

works for the single frame case by setting $M = 1$.

Assuming \mathbf{f} and \mathcal{H} are statistically independent, the blind MAP restoration problem may be stated as

$$\hat{\mathbf{f}}, \hat{\mathcal{H}} = \arg \max_{\mathbf{f}, \mathcal{H}} p_{g|f,h}(\bar{\mathbf{g}}|\mathbf{f}, \mathcal{H}) p_f(\mathbf{f}) p_h(\mathcal{H}) \quad (31)$$

We will assume that $p_{\eta}(\bar{\eta})$ is zero mean, i.i.d. Gaussian. This implies that $p_{g|f,h}(\bar{\mathbf{g}}|\mathbf{f}, \mathcal{H})$ is i.i.d. Gaussian with a mean of $\mathcal{H}\mathbf{f}$.

In order to model \mathbf{f} as a sparse MRF, we follow the development of Phillips and Leahy by defining

$$\mathbf{f} = \mathbf{X}\mathbf{z} \quad (32)$$

where \mathbf{X} is a diagonal matrix with elements of either 0 or 1. The vector \mathbf{z} is vector of amplitudes. The vector $\mathbf{x} = \text{diag}\{X\}$, represents an indicator process that determines whether or not a particular pixel is active. In the solution of equation (31) we make the replacement

$$p_f(\mathbf{f}) = p_{x,z}(\mathbf{x}, \mathbf{z}) = p_x(\mathbf{x}) p_z(\mathbf{z}) \quad (33)$$

where we assume the indicator process and the amplitude process are independent. The indicator function can be modeled as a binary Markov random field whose probability density function follows a Gibb's distribution,

$$p(\mathbf{x}) = \frac{1}{K} \exp(-V(\mathbf{x})), \quad x_i \in \{0, 1\} \quad (34)$$

where K is a normalizing constant and the Gibbs distribution potential function, $V(\mathbf{x})$, is given by

$$V(\mathbf{x}) = \sum_i \alpha_i x_i + \beta_i C_i\{x_i, x_j, j \in \mathcal{N}_i\} \quad (35)$$

where α_i and β_i are weighting constants and C_i is a clustering function that operates on pixels in the neighborhood \mathcal{N}_i [8]. Arguing that there is no reason to suspect any clustering *a priori* of adjacent pixels in star images (clusters may exist, but individual stars would be separated by

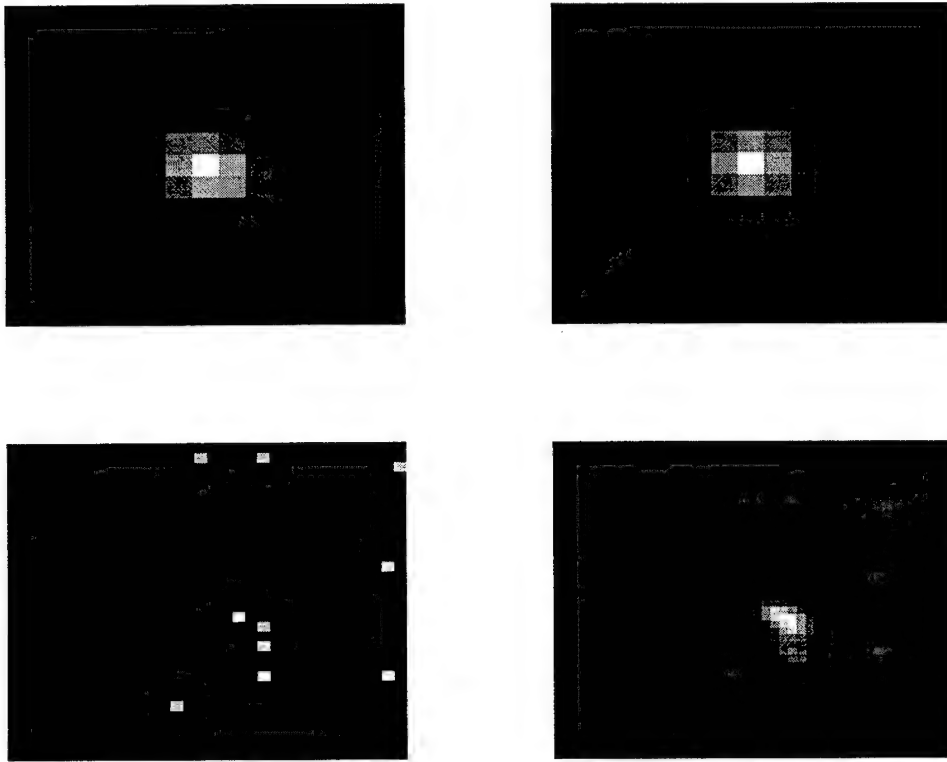


Figure 3: Image to be restored. Top left: Actual blur psf formed as an elliptical Lorentzian function on a GGMRF residual halo producing a realistic AO low-pass “mottled” halo field. Top right: Circularly symmetric Lorentzian blur model to be used as the reference mean, μ_h . Bottom left: Actual truth image. Bottom right: Observed blurred, noisy output data.

some black space, which is different from the Phillips-Leahy clustering model), we have omitted the clustering term and focused on the first term in equation (35) which enforces sparseness in the final image.

The density function for the amplitudes is assumed to be Gaussian in the Phillips-Leahy approach. They are dealing with MEG processing in which the amplitudes can be either positive or negative and thus introduce a zero mean Gaussian. In star images, where we deal only with intensities, negative amplitudes are unacceptable. This can be enforced by adding a mean to the Gaussian, m_z . Another method is to simply draw the amplitudes from a uniform distribution over some positive range and let the noise term in Equation (31) dictate the final values.

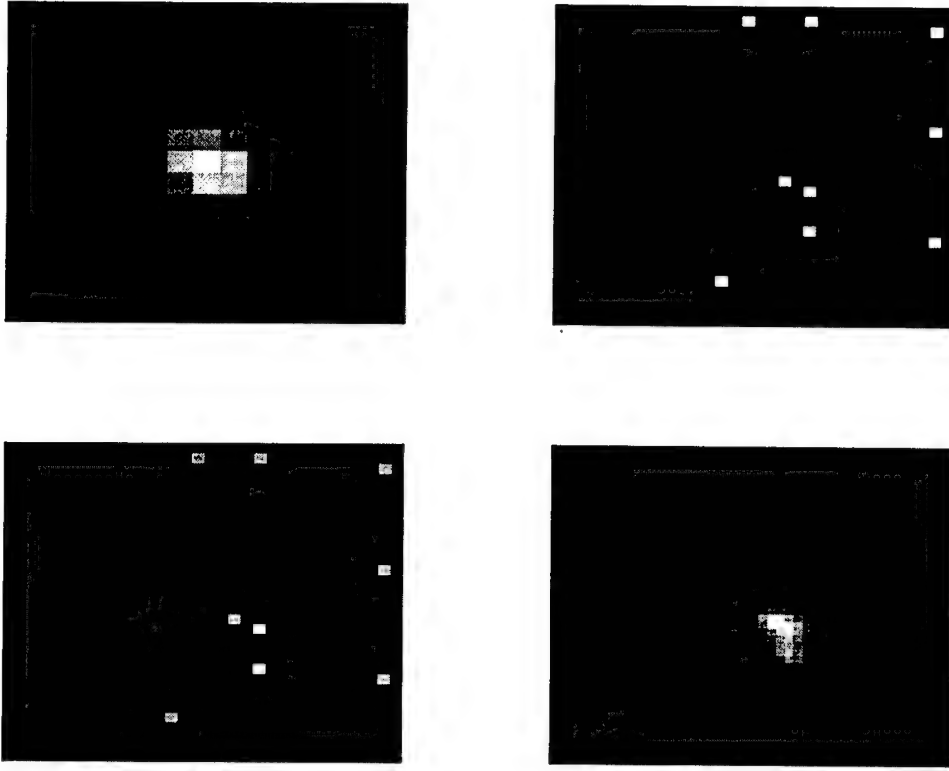


Figure 4: Restoration results. Top left: Estimated blur. Top right: Restored activity matrix. Bottom left: Restored input image. Bottom right: Restored image blurred with restored blur psf. Compare with Figure 3.

The blur pdf is modeled as a GGMRF with density

$$p_h(\mathcal{H}) = \frac{1}{Z_h} \exp \left\{ -\alpha \sum_{s \in S_h} d_s |h_s - \mu_{h,s}|^q - \right. \quad (36)$$

$$\left. \alpha \sum_{\langle s,t \rangle \in C_h} c_{s,t} |(h_s - \mu_{h,s}) - (h_t - \mu_{h,t})|^q \right\}$$

where C_h is the set of all cliques for the blur neighborhood system, q is the blur GGMRF shape parameter, S_h is the set of all points in the blur lattice over all frames and $c_{s,t}$ and d_s are neighborhood influence weights.

It has been shown in previous publications, for example [7], that $q > 2$ does a good job modeling smooth features such as those found in a typical blur psf. The mean, $\mu_{h,s}$, allows the restoration to maintain fidelity with prior knowledge about the blur. For example, in astronom-

ical imaging isolated stars in a nearby field can be averaged to give a reference mean.

Combining the density functions we can re-express equation (31) by taking the logarithm of both sides and dropping the additive constants

$$\begin{aligned} \hat{\mathbf{x}}, \hat{\mathbf{z}}, \hat{\mathcal{H}} = \arg \min_{\mathbf{x}, \mathbf{z}, \mathcal{H}} & \sum_{i=1}^M \|\mathbf{g}_i - \mathbf{H}_i \mathbf{X} \mathbf{z}\|^2 + \\ & \gamma \sum_j x_j + \lambda \|\mathbf{z} - \mu_{\mathbf{z}}\|^2 \\ & + \alpha \sum_{s \in S_h} d_s |h_s - \mu_{h,s}|^q + \\ & \alpha \sum_{\langle s,t \rangle \in C_h} c_{s,t} |(h_s - \mu_{s,t}) - (h_t - \mu_{h,t})|^q \end{aligned} \quad (37)$$

Here λ, γ, α control the relative influence as regularizing terms that the activity matrix, amplitudes, and blur have on the solution.

Equation (37) represents a very complicated nonlinear minimization problem. The approach taken to solve it is simulated annealing [9, 10], specifically the Metropolis algorithm [11]. λ, γ, α are set manually and adjusted for best restoration performance.

3.2 Results for Bayesian Blind Point Source Restoration

In this section we present examples of the new blind algorithm using simulated adaptive optics telescope data. In Figure (3), the actual data for the first example is presented. This shows a blur with region of support that is 15×15 pixels. The blur is a rotated Lorentzian function with an elongated axis. This has been shown to be an excellent model for AO residual blur [6]. The reference mean used for the blur is a circularly symmetric Lorentzian shape, with different radius than either axis of the actual blur. The truth image is also shown consisting of ten isolated points. The bottom right image shows the resulting blurred, noise corrupted output. The noise is zero-mean white Gaussian noise at a level of 32 dB peak SNR.

Note that only one observed frame is used in this restoration example. This is actually a more difficult problem than the case of multiple frames with different blurs for each frame. In the multiframe case, the diversity provided by distinct, unknown blurs aids in the blind restoration because only the true image is common to all frames.

Figure (4) shows the results of the algorithm described above. The blur has been estimated

quite accurately. The main axis is quite clearly defined in the restoration and the extent of the restored blur matches the actual blur very well. The source restoration matches the actual image to a high degree. However, two points in the L-shaped structure of the original source were blurred into a single point in the solution and some positions are inaccurate by a single pixel.

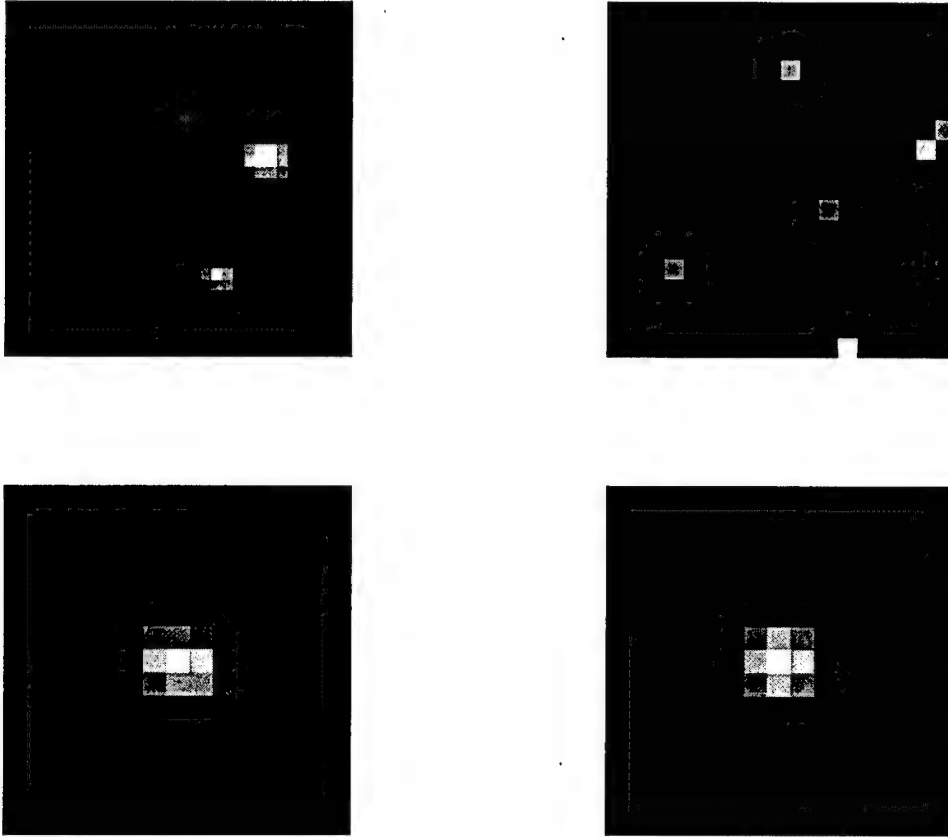


Figure 5: Second example. Top left: Observed blurred, noisy output data. Top right: Actual truth image. Bottom left: Actual blur psf. Bottom right: Circularly symmetric Lorentzian reference mean.

The actual data for the second example is found in Figure (5). Here we have a similar blur with a input image. Figures (6) and (7) show two different restorations on the data. In each of the restorations, the blur is only slightly elongated suggesting too much weight on the blur self term (i.e. on μ_h). Each of the input image restorations are fairly good. The first misses a point to the bottom right of the input image and some other positions are off by about a pixel. The second get all points but in the upper portion of the input image, one of the points is split.

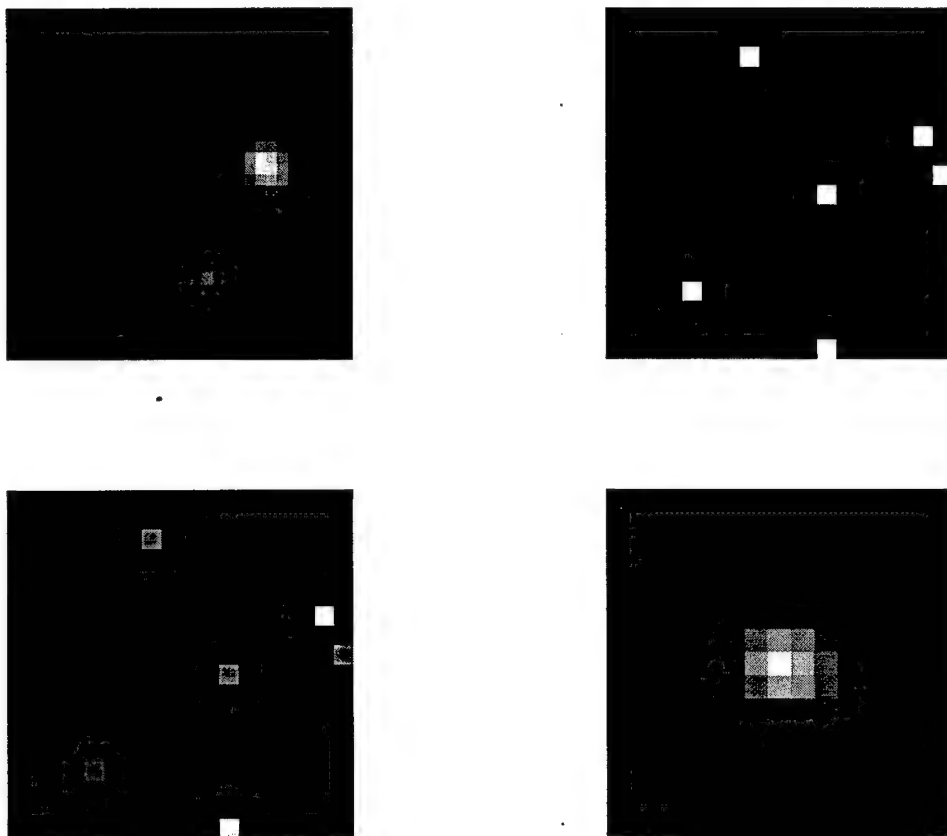


Figure 6: Second example, first restoration. Top left: Restored image blurred with restored blur psf. Top right: Restored activity matrix. Bottom left: Restored input image. Bottom right: Restored blur psf.

This is likely due to very circular restoration of the blur. These problems would likely be solved with better weights on the various priors.

4 Conclusions

This report has detailed the progress made under support from 1999 AFOSR Summer Research Extension Program for research in multiframe blind restoration of space objects images from adaptive optics systems. This effort has been very fruitful, and some very promising new technologies have been identified. It is expected that this research effort will lead to higher resolution restorations of AO images with less computational burden than other blind algorithms.

We have presented two methods of blind point-source image restoration based on determin-

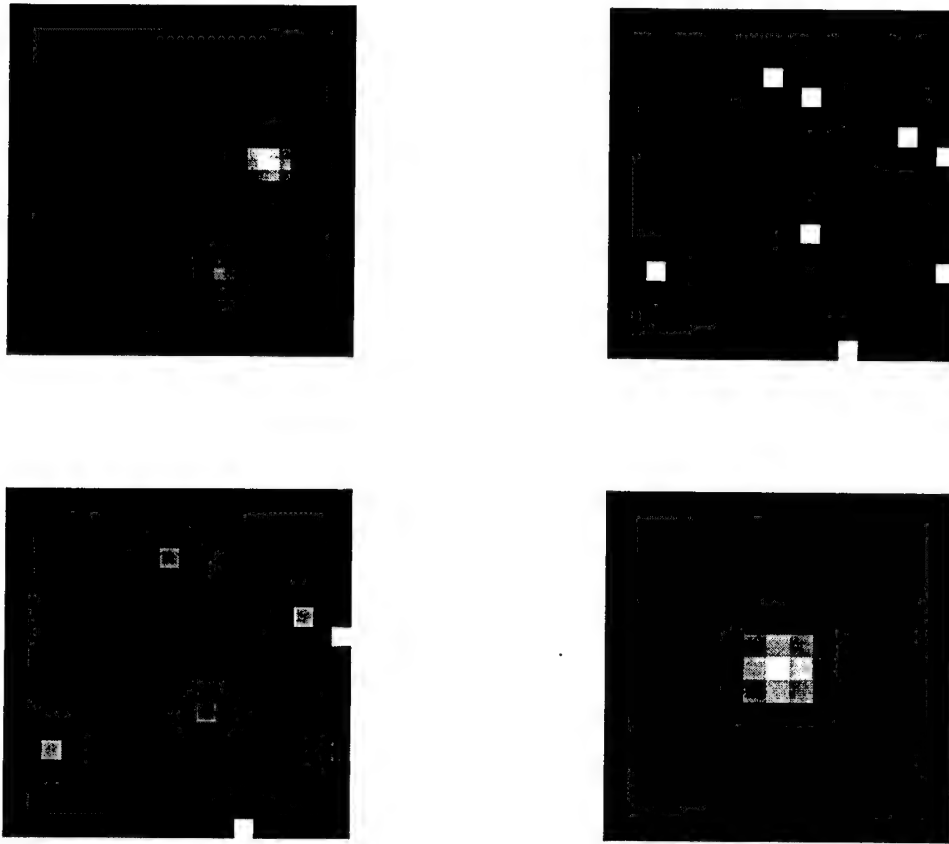


Figure 7: Second example, second restoration. Top left: Restored image blurred with restored blur psf. Top right: Restored activity matrix. Bottom left: Restored input image. Bottom right: Restored blur psf.

istic, subspace decomposition algorithms, and a third method using sparse statistical models as the basis of a Bayesian estimation approach. For the subspace approach, the underlying point-source image is recovered from a single observation frame without any prior knowledge about the blurring function (in the case of the non-separable algorithm). If it is known that the blur psf is separable, then an even more computationally efficient algorithm is available. Other known point source restoration methods are iterative, or require knowledge of the blur, or require multiple observation frames with distinct blur; or are based on statistical signal models, or involve lengthy simulated annealing optimization codes [2, 5, 12, 13]. We believe the new methods presented here are superior, first in elegance and second in speed. We know of no other deterministic blind method which is optimized for point-source images. The new methods

involve extension and adaptation of digital communications algorithms, originally developed for resolving overlapping multipath echoes, so that they can be used in 2-D blind imaging problems. Future work should include further attention to the issue of linking the separate x and y spectrum scanned position estimates in the non-separable algorithm. Methods of extracting blur psf and point amplitude estimates from the non-separable algorithm are also under study.

The Bayesian approach was also shown to be a viable tool in solving the blind point source image restoration problem. The restoration examples shown above demonstrate the power of the model described in this report to emphasize the sparse character of a source image. Though GGMRFs have been shown to work well for restoring extended objects, the model does not allow the user to explicitly enforce point-like structure on the solution. The specific point-source prior of Phillips and Leahy in conjunction with the GGMRF prior for the psf leads to blind restoration solutions which are truly sparse and are an excellent estimate of the truth. We have demonstrated that the Phillips - Leahy MRF model for point sources is well suited, with minor modifications, to *blind* star field image restoration. Previously this model had been used only with known blurring or system functions.

4.1 Additional Accomplishments Supported by the SREP Grant

This section summarizes accomplishments resulting from the AFOSR Summer Faculty Research Extension Program support of my research collaboration with Starfire Optical Range at Kirtland Air Force Base. These activities are in addition to the research progress reported above, and include work completed from the end of 1998 until the present.

List of Additional Accomplishments:

- Technical Papers Resulting From SOR Work:
 1. Brent A. Chipman and Brian D. Jeffs, "Blind Multiframe Point Source Image Restoration Using MAP Estimation," *Conference Record, Thirty-Third Asilomar Conference on Signals, Systems, and Computers*, Nov. 1999, Pacific Grove CA.
 2. Brent A. Chipman and Brian D. Jeffs, "Blind Point-Source Image Restoration Using Subspace Techniques," to appear in *Proceedings of IEEE International Conference*

on Acoustics, Speech, and Signal Processing, ICASSP-2000, Istanbul Turkey, June 2000.

- Master's thesis resulting from this funded research: Brent Chipman, *Methods of Blind Point Source Restoration*, Brigham Young University, Dec. 1999.
- Student support: This research program has had a profound effect on two of my graduate students. Brent Chipman has recently graduated with a Master's degree, and a fine thesis reporting his work in AO image post processing. Also, Lisha Li has recently started Ph.D. dissertation work based on this research program.
- Ongoing work: includes a collaborative research effort with Julian Christou and Stuart Jefferies of the University of Arizona. We are currently preparing a proposal for AFOSR for continued work in advanced algorithms for blind restoration of AO images of satellites.

I expect that my research in this fruitful area and collaboration with Starfire Optical Range will continue for a number of years.

References

- [1] R. Roy and T. Kailath, "Esprit - estimation of signal parameters via rotational invariance", *IEEE Transactions on Acoustics, Speech, and Signal Processing*, vol. 37, no. 7, pp. 984-995, July 1989.
- [2] Metin Gunsay and Brian D. Jeffs, "Point-source localization in blurred images by a frequency-domain eigenvector-based method", *IEEE Transactions on Image Processing*, vol. 4, no. 12, pp. 1602-1612, December 1995.
- [3] B. Jeffs, S. Hong, and J. Christou, "Generalized gauss markov model for space objects in blind restoration of adaptive optics telescope images", in *Proceedings of the International Conference for Image Processing*, Nagasaki, October 1998, vol. 2, pp. 737-741.
- [4] A. Swindlehurst and J. Gunther, "Methods for blind equalization and resolution of overlapping echoes of unknown shape", *IEEE Transactions on Signal Processing*, vol. 47, no. 5, pp. 1245-1254, April 1999.
- [5] Brent A. Chipman, "Methods of blind point source restoration", Master's thesis, Brigham Young University, 1999.
- [6] J.D. Drummond, "Sizes, shapes and rotational poles of ceres and vesta from adaptive optics images", *Bulletin of the American Astronomical Society*, vol. 27, pp. 16, 1996.
- [7] Brian Jeffs, Sheila Hong, and Julian Christou, "A generalizaed gauss markov random model for space objects in blind restoration of adaptive optics telecope images", *Proceedings of the International Conference on Image Processing*, vol. 4, pp. 1885-1888, 1998.

- [8] J. Phillips, R. Leahy, and J. Mosher, "Meg-based imaging of focal neuronal current sources", *IEEE Transactions on Medical Imaging*, vol. 16, no. 3, pp. 338–348, June 1997.
- [9] S. Geman and D. Geman, "Stochastic relaxation, gibbs distributions, and the bayesian restoration of images", *IEEE Transactions on Pattern Analysis and Machine Intelligence*, pp. 721–741, November 1984.
- [10] S. Kirkpatrick, J. Gelatt, and M Vecchi, "Optimization by simulated annealing", *Science*, vol. 220, pp. 671–680, May 1983.
- [11] N. Metropolis, A. Rosenbluth, M Rosenbluth, A. Teller, and E. Teller, "Equation of state calculations by fast computer machines", *Journal of Chemical Physics*, vol. 21, pp. 1087–1092, 1953.
- [12] J. Phillips, R. Leahy, and J. Mosher, "Meg-based imaging of focal neuronal current sources", *IEEE Transactions on Medical Imaging*, vol. 16, no. 3, pp. 338–348, June 1997.
- [13] S.M. Jefferies and J.C. Christou, "Restoration of astrononmical images by iterative blind deconvolution", *Astrophysical Journal*, vol. 415, pp. 862–874, Oct. 1993.

LIGHTWEIGHT ACOUSTIC SOURCES FOR
INTERIOR NOISE CONTROL OF
LAUNCH VEHICLE PAYLOAD FAIRINGS

Donald J. Leo
Assistant Professor
Mechanical Engineering Department

Virginia Polytechnic Institute and State University
Mechanical Engineering Department
Blacksburg, VA 24061-0261

Final Report for:
Summer Extension Research Program
Air Force Research Lab - Phillips Site
Albuquerque, New Mexico

Sponsored by:
Air Force Office of Scientific Research
Bolling Air Force Base, DC
and
Air Force Research Lab - Phillips Site

February 2000

LIGHTWEIGHT ACOUSTIC SOURCES FOR
INTERIOR NOISE CONTROL OF
LAUNCH VEHICLE PAYLOAD FAIRINGS

Donald J. Leo
Assistant Professor
Center for Intelligent Material Systems and Structures
Mechanical Engineering Department
Virginia Polytechnic Institute and State University

Abstract

A model of a piezoceramic transducer coupled to a cylindrical cavity is derived for the purpose of studying active damping of interior noise. The model is nondimensionalized to determine the critical parameters that affect the structural-acoustic coupling of the transducer. The nondimensional model yields four critical parameters: the mass ratio of the acoustic piston to the beam flexure; the actuator-to-flexure stiffness ratio; the acoustic-to-flexure stiffness ratio; and the frequency response of the acoustic load. Nondimensional expressions for these parameters are derived as a means of relating the transducer design to the structural-acoustic response. Numerical analysis indicates that minimizing the mass ratio and making the stiffness ratios approximately unity results in sufficient structural-acoustic coupling. Simulations of velocity feedback demonstrate the feasibility of the concept. Applications for this work include the development of lightweight transducers for problems such as interior noise in launch vehicle payload fairings.

Introduction

Interior noise control is important for a number of aerospace applications. Previous research has focused on understanding the fundamental mechanisms of sound transmission into enclosed spaces [1, 2]. Experimental results have been presented for simple structures such as rectangular enclosures and cylinders, and for more complicated geometries that model the structural-acoustics of aircraft.

The motivation for this work is interior noise control for launch vehicle payload fairings. One of the critical features of this aerospace application is the need for lightweight transducers for active control of sound. Although weight is a primary design parameter for all applications, it is especially important in launch vehicle noise control because of the cost associated with placing payloads into orbit. Current cost estimates for launch vehicles are approximately \$10,000 per pound of payload capacity. Weight added to the vehicle for the purpose of active noise control will reduce the payload capacity of the vehicle. Therefore the feasibility of active noise control for payload fairings is strongly coupled to the development of lightweight transducers for controlling the interior noise.

Most of the experimental work in interior noise control has utilized speakers as the acoustic control source. Speakers are a mature technology that provide the necessary stroke and acoustic power for noise control applications. A conventional speaker utilizes an electromagnetic actuator as the driving element, a cone as the acoustic element, and some measure of stiffness for mechanical stability. The moving mass of the speaker and the mechanical stiffness create a mechanical resonance that varies depending on the speaker design. Typical

values for this resonance are 20-50 Hz for bass speakers and 200-300 Hz for smaller designs.

Although speakers offer many advantages for noise control, they also have drawbacks that are inherent in the speaker design. The mechanical resonance of the speaker introduces actuator dynamics that can be problematic for feedback control. The phase lag associated with the resonance can cause stability problems and reduce achievable performance. Eliminating problems due to mechanical resonance was the basis for the work of Clark and Lane in the development of a 'constant volume velocity source' [3] They developed a technique for estimating the velocity of an electromagnetic speaker for the purpose of reducing the phase lag associated with mechanical resonance. They applied their technique to the control of ducts and the fuselage of a small aircraft. Another drawback of conventional speaker technology is the sheer weight of the transducer. The magnets required for the the driving element are the heaviest component of the device. This is particularly problematic for low-frequency applications that require large strokes.

The purpose of this work is to investigate the use of piezoceramic actuators as driving elements for noise control transducers. The objective is to develop a lightweight transducer that overcomes problems due to mechanical resonance. Sound absorption will be accomplished with feedback control utilizing the piezoceramic transducers. The control algorithms will be simple and robust to maximize reliability.

The rationale for this work is a recent paper by Leo and Limpert on the development of a self-sensing technique for acoustic attenuation [4]. They developed and implemented an algorithm that estimated the back pressure of an electromagnetic speaker using a measure

of the electrical impedance. The technique was effective in frequency ranges in which the electrical impedance was coupled to the acoustic resonances of the enclosed space. Outside this range the algorithm was overly sensitive to small errors in the implementation of the estimated electromechanical impedance.

This work highlighted the importance of coupling the transducer to the acoustic field. Subsequent analyses indicated that if the transducer was coupled to the acoustic field then there was no compelling reason to perform self-sensing; it was sufficient to utilize the transducer as a collocated control element for active damping.

Therefore this work will concentrate on identifying the critical parameters for developing an acoustic source utilizing piezoceramic transducers for acoustic feedback control. The next section will discuss the fundamental concept and a simplified model will be developed in the subsequent section. A discussion of the critical design parameters will be presented and several numerical analyses will be performed to demonstrate the coupling of the transducer to the acoustic field.

Transducer Modeling

Figure 1a is a schematic of the transducer concept. The transducer consists of an acoustic piston and a housing which is similar to a conventional speaker. The piston is angled to maximize the stiffness per unit area of the acoustic source. The actuation elements are a set of piezoceramic bimorphs attached to the bottom of the piston and cantilevered on the housing. A single actuator and bimorph is called a flexure. The set of flexures provide the

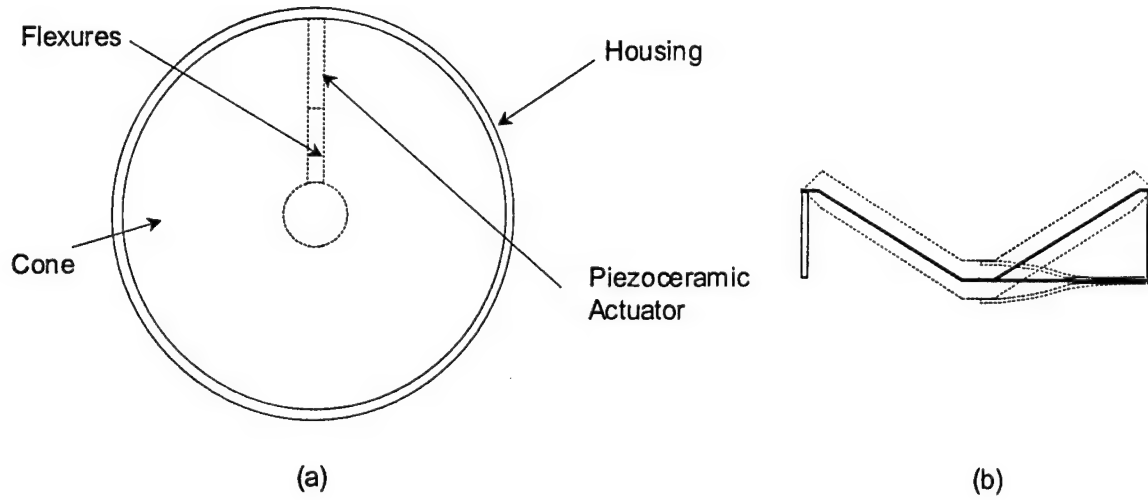


Figure 1: Transducer concept illustrating the flexure and actuation mechanisms: (a) top view, (b) side view illustrating the assumptions of pure translation.

mechanical stiffness of the acoustic source.

The goal of this work is to investigate the critical parameters of the transducer design. To this end, we will model the structural-acoustic coupling of a single flexure for a particular acoustic load. This will allow us to develop a set of nondimensional parameters that couple the electromechanical parameters of the flexures to the resonances of the acoustic cavity.

Figure 1b is a simplified model of the transducer flexure. For this work we assume that each flexure is cantilevered to the housing. Thus the displacement and rotation is zero where the flexure is attached to the housing. Another assumption is that the cone undergoes pure translation and no rotation. Thus the rotation of each flexure is zero where the flexure is attached to the cone. The mass of the cone is modeled as a concentrated mass at the end of each flexure.

The simplified transducer model will be separated into three parts: a beam model for the flexure, a one-dimensional strain model for the sensors and actuators, and an impedance model for the acoustic load. For this work, the acoustic loads is assumed to be a cylindrical tube with a rigid termination. The beam model will be developed through an energy formulation and the actuator and acoustic loads will be modeled as nonconservative work terms acting on the flexure.

Flexure Model

Each flexure is modeled independently using the assumed modes method. The flexure is assumed to be a thin, flexible beam that satisfies the Euler-Bernoulli assumptions. The transverse displacement of the beam is denoted $w(x, t)$. The kinetic and potential energy terms for the beam are

$$T = \frac{1}{2} \int_0^L \rho A \left\{ \frac{\partial w(x, t)}{\partial t} \right\}^2 dx + \frac{1}{2} m_p \left\{ \frac{\partial w(x_c, t)}{\partial t} \right\}^2 \quad (1)$$

$$V = \frac{1}{2} \int_0^L EI \left\{ \frac{\partial^2 w(x, t)}{\partial x^2} \right\}^2 dx$$

where ρ , A , E , and I are the density, cross sectional area, modulus, and cross sectional inertia of the beam, respectively. The concentrated mass m_p models the mass of the rigid piston. Piston inertia and the static load due to the piston are neglected. The nonconservative work due to piezoceramic actuation is expressed as

$$W_{nc} = m_a(t) \left\{ \frac{\partial w(x_2, t)}{\partial x} - \frac{\partial w(x_1, t)}{\partial x} \right\} - p(t) A_p w(x, t) \quad (2)$$

where m_a is the moment applied by the actuator, p is the uniform back pressure applied to the piston, and A_p is the piston area. Assuming that the displacement w is separable in

space and time and expressed as a linear combination of *admissible functions* $\phi(x)$:

$$w(x, t) = \sum_{i=1}^N \phi_i(x) q_i(t) \quad (3)$$

where the admissible functions satisfy the geometric boundary conditions of the structure.

we can write the kinetic energy expression in matrix form

$$\begin{aligned} T &= \frac{\rho AL}{2} \dot{q}(t)^T M_b \dot{q}(t) + \frac{1}{2} \dot{q}(t)^T M_c \dot{q}(t) \\ V &= \frac{EI/L^2}{2} q(t)^T K_b q(t) \end{aligned} \quad (4)$$

where,

$$\begin{aligned} M_{b_{ij}} &= \int_0^1 \phi_i(\xi) \phi_j(\xi) d\xi \\ M_{p_{ij}} &= \mu \phi_i(\xi_c) \phi_j(\xi_c) \\ K_{b_{ij}} &= \int_0^1 \frac{d^2 \phi_i(\xi)}{d\xi^2} \frac{d^2 \phi_j(\xi)}{d\xi^2} d\xi \end{aligned} \quad (5)$$

and $\xi = x/L$ is a nondimensional length and $\mu = \frac{m_p}{\rho AL}$. The nonconservative work terms can also be written as a matrix expression

$$W_{nc} = \frac{m_a(t)}{L} B_a^T q(t) - p(t) A_p B_p^T q(t) \quad (6)$$

where

$$B_a = \left[\frac{d\phi_1(\xi_2)}{d\xi} - \frac{d\phi_1(\xi_1)}{d\xi} \dots \frac{d\phi_N(\xi_2)}{d\xi} - \frac{d\phi_N(\xi_1)}{d\xi} \right]^T \quad (7)$$

and,

$$B_p = [\phi_1(1) \dots \phi_N(1)]^T \quad (8)$$

The equations of motion are derived using the Lagrangian formulation:

$$\rho AL \{M_b + \mu M_p\} \ddot{q} + \frac{EI}{L^3} K_b q = \frac{1}{L} B_a m_a - A_p B_p p. \quad (9)$$

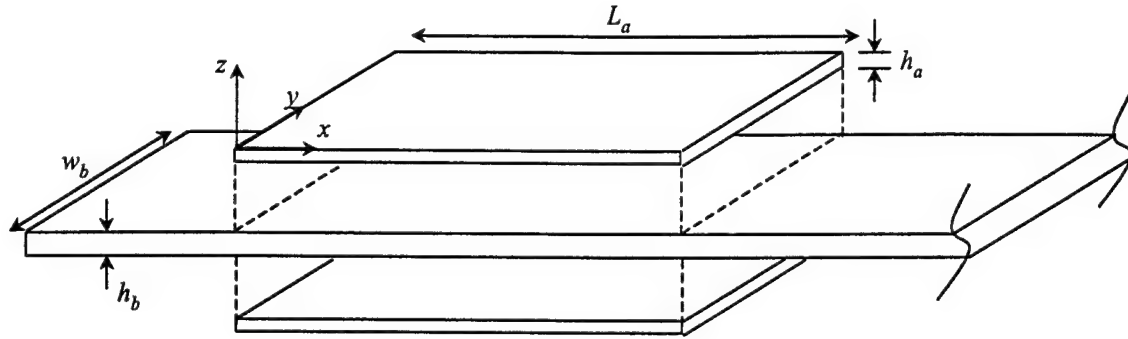


Figure 2: Geometry of the beam and surface-bonded piezoceramic.

The (t) notation has been dropped for convenience. For this work we will be concerned with the steady-state response of the absorber, therefore we transform equation (9) into the frequency domain:

$$\left[\frac{EI}{\rho AL^4} K_b - \omega^2 (M_b + \mu M_p) \right] Q(\omega) = \frac{1}{\rho AL^2} B_a M_a(\omega) - \frac{A_p B_p}{\rho AL} P(\omega) \quad (10)$$

Actuator Model

The actuators are modeled with the one-dimensional constitutive relationships for a piezoceramic material:

$$\begin{aligned} D_3 &= \epsilon_{33} E_3 + d_{32} T_2 \\ \epsilon &= d_{32} E_3 + Y_{22} T_2 \end{aligned} \quad (11)$$

where ϵ_{33} , d_{32} , and Y_{22} are material properties of the ceramic, D_3 is the electric displacement, E_3 is the electric field applied in the z direction, and ϵ and T_2 are the strain and stress, respectively. The applied electric field E_3 is simply the applied voltage divided by the thickness of the piezoceramic, h_a . The applied stress is equivalent to the actuator force

divided by the side area of the ceramic, $\frac{f_a}{w_b h_a}$. Integrating the expression for the electric displacement over x and y yields an expression for the induced charge, q_a , and displacement, x_a , of the piezoceramic:

$$\begin{aligned} Q &= CV + x_o f_a \\ x_a &= x_o V + \frac{1}{k_a} f_a. \end{aligned} \tag{12}$$

The moment induced by the piezoceramic actuators can be written as

$$m_a = 2f_a \frac{h_b + h_a}{2} = [x_o k_a V - k_a x_a] (h_b + h_a) \tag{13}$$

Assuming small deformations and hence small rotation angles, we can write the extension of the actuator as

$$x_a = \frac{h_b + h_a}{2L} B_a^T q \tag{14}$$

Equations (13) and (14) can be combined to yield an expression for the moment applied by the piezoceramic actuator pair. Transforming the expression into the frequency domain yields

$$M_a(\omega) = x_o k_a (h_b + h_a) V(\omega) - k_a \frac{(h_b + h_a)^2}{2L} B_a^T Q(\omega) \tag{15}$$

Acoustic Impedance Model

The final component of the absorber model is an expression for the acoustic load applied to the piston. We will utilize frequency-dependent impedance models as a means of related the piston motion to the sound pressure. The use of impedance models makes it straightforward to vary the type of acoustic load presented to the piston. A general impedance model of the

acoustic load is

$$\frac{P(\omega)}{U(\omega)} = Z_a(\omega), \quad (16)$$

where U is the volume velocity of the piston. Assuming that the volume velocity is equal to $A_p \dot{w}(1, t)$ due to the fact that the displacement of the piston is equivalent to the tip displacement of the beam, we can write

$$A_p P(\omega) = j\omega A_p^2 Z_a(\omega) B_p^T Q(\omega). \quad (17)$$

For this work we will assume that the absorber is connected to a cylindrical tube with a rigid end termination. Under this assumption, the acoustic impedance is $Z_a(\omega) = -j(\rho_a c / A_p) \cot(\omega l / c)$, where ρ_a is the density of air, c is the speed of sound, and l is the length of the tube. This function can be approximated in the frequency domain as

$$Z_a(\omega) = \frac{1}{j\omega} \frac{\rho_a c^2}{A_p l} \frac{\prod_{i=1}^N (1 - \omega^2 / \omega_{zi}^2)}{\prod_{i=1}^N (1 - \omega^2 / \omega_{pi}^2)} = \frac{1}{j\omega} \frac{\rho_a c^2}{A_p l} k_t(\omega). \quad (18)$$

For a cylindrical tube with a rigid termination:

$$\begin{aligned} \omega_{zi} &= (2i - 1) \frac{\pi c}{2l} & i &= 1, 2, \dots \\ \omega_{pi} &= i \frac{\pi c}{l} & i &= 1, 2, \dots \end{aligned} \quad (19)$$

Combining equations (17) and (19) yields an expression for the force applied to the piston as a result of flexure motion:

$$A_p P(\omega) = \frac{\rho_a c^2 A_p}{l} k_t(\omega) B_p^T Q(\omega). \quad (20)$$

The term $k_t(\omega)$ is a frequency dependent stiffness that will vary depending on the type of acoustic load that is presented to the absorber.

Table 1: Nondimensional parameters for the absorber analysis.

	Symbol	Representation
mass ratio	μ	$m_p/\rho AL$
actuator-to-flexure stiffness ratio	κ_a	$6 \frac{E_a}{E} \frac{L}{L_a} \frac{(1+h_b/h_a)^2}{(h_b/h_a)^3}$
tube-to-flexure stiffness ratio	κ_t	$\frac{\rho_a c^2 A_p/l}{EI/L^3}$
structure-to-acoustic time scale	γ	$\sqrt{\frac{c^2/l^2}{EI/\rho AL^4}}$
tube stiffness	$k_t(\sigma)$	$\frac{\prod_{i=1}^N \left(1 - \frac{4}{\gamma^2 \pi^2 (2i-1)^2} \sigma^2\right)}{\prod_{i=1}^N \left(1 - \frac{1}{\gamma^2 \pi^2 i^2} \sigma^2\right)}$

Nondimensional Analysis

Equations (10), (15), and (20) are combined into the transducer equations of motion and nondimensionalized for the parametric analysis. The equations are nondimensionalized by introducing the following change of variables:

$$\sigma = \omega \sqrt{\rho AL^4/EI} \quad \eta = q/L \quad (21)$$

The resulting nondimensional equations are

$$\left[K_b + \kappa_a B_a B_a^T + \kappa_t k_t(\sigma) B_p B_p^T - \sigma^2 (M_b + \mu M_p) \right] \eta(\sigma) = 2\kappa_a \frac{x_o}{h_a} \frac{1}{1 + h_b/h_a} B_a V(\sigma). \quad (22)$$

The terms κ_a , κ_t , and $k_t(\sigma)$ are defined in Table 1. Defining

$$H(\sigma) = K_b + \kappa_a B_a B_a^T + \kappa_t k_t(\sigma) B_p B_p^T - \sigma^2 (M_b + \mu M_p), \quad (23)$$

we can write

$$\begin{aligned} \frac{X_a(\sigma)}{x_o V(\sigma)} &= \kappa_a B_a^T H(\sigma)^{-1} B_a \\ \frac{X_p(\sigma)}{x_o V(\sigma)} \frac{h_a + h_b}{2L} &= \kappa_a B_p^T H(\sigma)^{-1} B_a. \end{aligned} \quad (24)$$

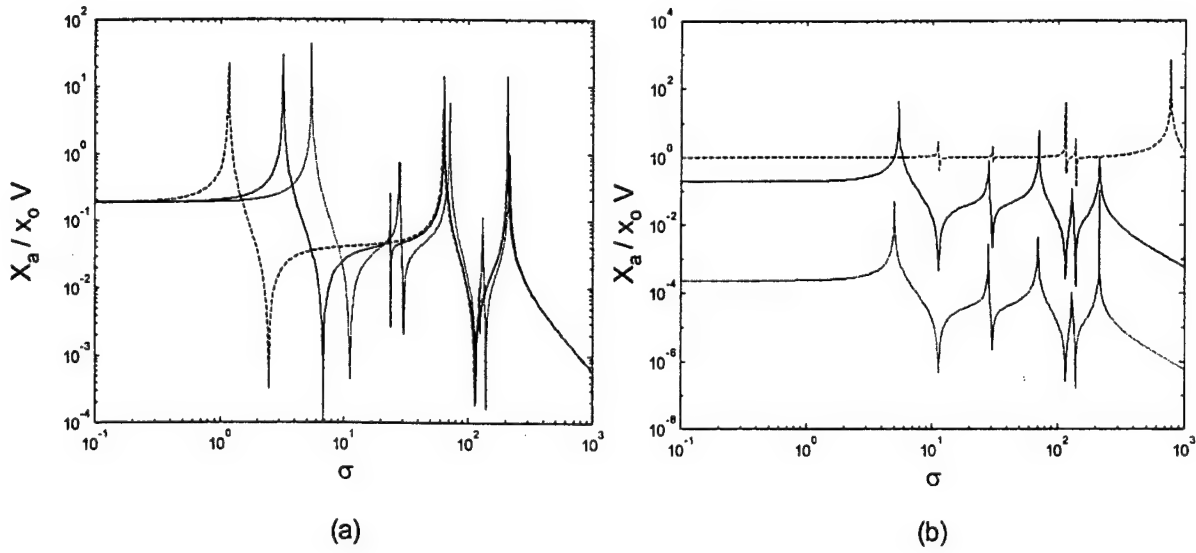


Figure 3: (a) Magnitude of $\frac{X_a(\sigma)}{x_0 V(\sigma)}$ for three values of μ : 1/10 (dotted), 1 (solid), and 10 (dashed); (b) magnitude of $\frac{X_a(\sigma)}{x_0 V(\sigma)}$ for three values of κ_a : 1/1000 (dotted), 1 (solid), 1000 (dashed).

The expressions in equation (24) represent the transfer functions between the applied voltage and the actuator motion, x_a , and the tip motion of the flexure, x_p .

Equation 22 illustrates that the response of the transducer is a function of the mass ratio, the actuator-to-flexure stiffness, the tube stiffness, and the tube-to-flexure stiffness ratio. The tube stiffness is a function of the number of terms in the acoustic expansion and the structure-to-acoustic time scale. The effect of varying these four parameters is studied with a numerical model of the transducer. The numerical model utilizes a five-mode expansion of a clamped-sliding beam and a ten-mode expansion of the acoustic impedance. The mode shapes and natural frequencies of a clamped-sliding beam can be found in Inman. For brevity they will not be repeated here.

The four parameters μ , κ_a , κ_t , and $k_t(\sigma)$ were studied with the numerical model to understand their effect on the transducer response. Figure 3a is a plot of $|X_a/x_oV|$ as a function of the mass ratio μ . As expected, increasing the mass ratio from 1/10 to 10 increases the ratio between the second elastic mode of structure and the fundamental natural frequency. For the case when $\mu = 1/10$ the frequency ratio is approximately 5.2, which is the frequency ratio a bare beam with clamped-sliding boundary conditions. As the tip mass is increased to 10 the frequency ratio becomes closer to 20 and the flexure begins to exhibit the dynamics of a single-mode system.

A similar analysis is performed for the actuator-to-structure stiffness ratio. When the stiffness ratio is much less than 1, the magnitude of the actuator motion is almost four orders of magnitude smaller than the free extension of the actuator (x_oV). Increasing the stiffness ratio to unity increases the actuator displacement considerably without a significant effect on the pole-zero spacing in the frequency response $|X_a/x_oV|$. In the case when $\kappa_a \gg 1$, the average displacement of the actuator is approximately equal to the free displacement x_oV , but the mismatch between the actuator stiffness and the flexure stiffness creates a pole-zero cancellation in the frequency response. This pole-zero cancellation is due to the negligible resistance of the beam to actuator motion.

These analyses illustrate variation in the mass ratio and actuator-to-structure stiffness ratio without any coupling to the acoustic field. Structural-acoustic coupling is introduced by setting $\kappa_t > 0$ and varying the tube-to-flexure stiffness ratio. Figure 4a illustrates the change in the frequency response $|X_a/x_oV|$ as a function of κ_t . When $\kappa_t \ll 1$ there is

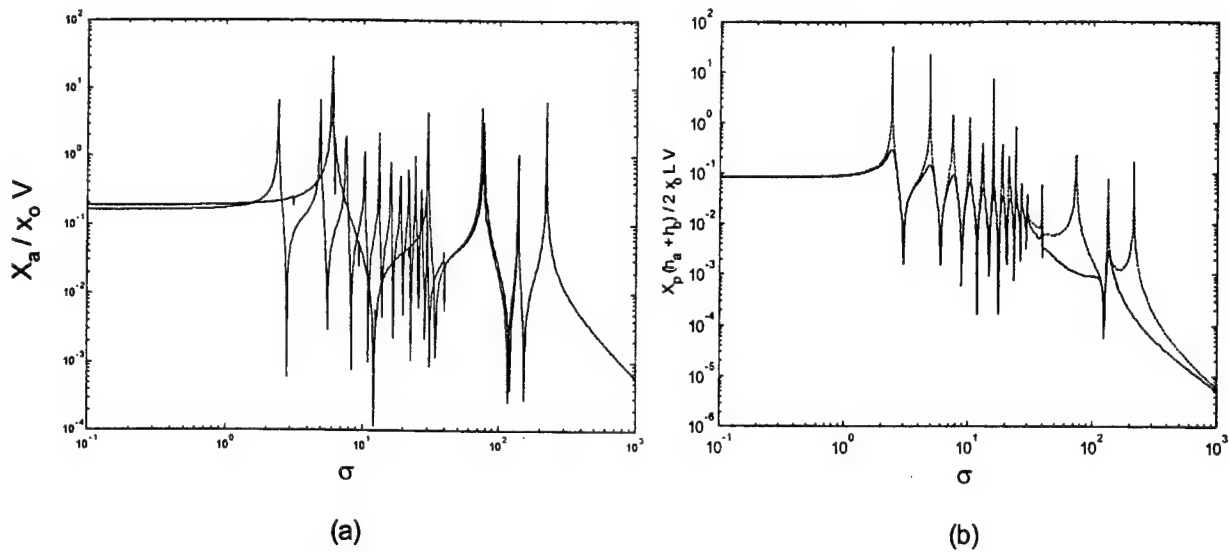


Figure 4: (a) Magnitude of $\frac{X_a(\sigma)}{x_o V(\sigma)}$ for two values of κ_t : 1/100 (dashed), 1 (solid) .

negligible coupling between the acoustic field and the actuator motion. Increasing κ_t to unity introduces a number of resonances into the frequency response. These resonances correspond to the coupled structural-acoustic modes of the enclosed cavity. Figure 4a demonstrates the basic feasibility of coupling the piezoceramic transducer to an enclosed cavity modeled as a finite tube. The coupling between the acoustic field and the transducer response manifests itself in the form of an interlacing pole-zero pattern of structural-acoustic resonances. A beneficial aspect of this frequency response is that the actuator and sensor are collocated with one another. Sensor-actuator collocation enables a simple and robust method of energy dissipation in the resonances through feedback control.

Feedback Control Simulations

A simple method of estimating the effectiveness of feedback control is to simulate active damping as a means of energy dissipation. The results of the previous section illustrated that structural-acoustic coupling is possible through judicious choice of transducer design parameters. Namely, minimizing the mass ratio and making the stiffness ratios approximately equal to unity resulted in coupling between the collocated sensor-actuator response of the piezoceramic transducer. These results will be the basis for a preliminary analysis of active damping of the coupled modes.

Feedback control simulations are performed by substituting

$$V(\sigma) = V_d(\sigma) - j\sigma \frac{k_v}{x_o \kappa_a} X_a(\sigma) \quad (25)$$

into equation (22), where $V_d(\sigma)$ is a disturbance voltage and k_v is a scalar feedback gain. Combining equations (14) and (22) yields an expression for the closed-loop matrix

$$H_{cl}(\sigma) = K_b + \kappa_a B_a B_a^T + \kappa_t k_t(\sigma) B_p B_p^T + j\sigma k_v B_a B_a^T - \sigma^2 (M_b + \mu M_p), \quad (26)$$

which can be directly substituted into the transfer functions in equation (24) to simulate the closed-loop response.

Figure 4b illustrates the effect of velocity feedback on the coupled structural-acoustic modes. The design parameters chosen for the simulation are $\mu = 1/10$, $\kappa_a = \kappa_t = 1$. The simulation of the closed-loop response demonstrates the broadband damping that is achieved with velocity feedback of the piezoceramic sensor output. The first eight structural-acoustic modes have approximately the same level of damping.

Acknowledgements

The authors would like to thank the Air Force Office of Scientific Research for supporting this work through the Summer Extension Research Program, contract number F49620-93-0063, subcontract number 99-0835. The program manager for this research is Dr. Steven Griffin of the Air Force Research Lab.

Summary and Future Work

The critical parameters associated with utilizing piezoceramic sensor-actuators for acoustic control were derived in this paper. The model consisted of an acoustic source driving a cylindrical cavity. Four nondimensional parameters were identified: the mass ratio between the acoustic piston and the beam flexure, the actuator-to-flexure stiffness ratio, the acoustic-to-flexure stiffness ratio, and the frequency response of the acoustic load. Numerical analysis demonstrated that minimizing the mass ratio and making the stiffness ratios approximately unity produced a transducer that was coupled to the acoustic field. Feedback control simulations illustrated the ability of the transducer to introduce broadband damping into the coupled structural-acoustic modes.

Future work will concentrate on quantifying the control authority of the transducer and experimentally-verifying transducer performance. A quantitative measure of the control authority will be studied by developing a state-space model of the transducer coupled to the enclosed cavity. This will allow us to use measures such as controllability and observability

grammians to quantify the coupling of the transducer to select modes. It will also allow us to perform a more detailed search of the entire parameter space and introduce optimization procedures for maximizing the structural-acoustic coupling. Once these studies have been performed we will produce a prototype transducer and experimentally verify the control performance.

References

- [1] P.A. Nelson and S.J. Elliot. *Active Control of Sound*. Academic Press, London, 1992.
- [2] Chris R. Fuller, S.J. Elliot, and P.A. Nelson. *Active Control of Vibration*. Academic Press, London, 1996.
- [3] Steven A. Lane and Robert L. Clark. Active control of a reverberant enclosure using an approximate constant volume velocity source. In *Proceedings of the American Control Conference*, pages 2606–2610, 1998.
- [4] Donald J. Leo and Douglas Limpert. Self-sensing technique for active acoustic attenuation. To appear in *Journal of Sound and Vibration*, 1999.

**INVESTIGATION INTO THE POWER LOSSES
FROM AMTEC COMPONENTS**

**M. A. K. Lodhi
Professor
Department of Physics**

**Texas Tech University
Lubbock, Texas 79409-1051**

**Final Report for:
Summer Faculty Research Program
Air Force Research Laboratory**

**Sponsored by:
Air Force Office of Scientific Research
Bolling Air Force Base, DC**

and

**Air Force Research Laboratory
Kirkland AFB**

November 1999

INVESTIGATION INTO THE POWER LOSSES FROM AMTEC COMPONENTS

M. A. K. Lodhi
Professor
Department of Physics
Texas Tech University
Lubbock, Texas 79409

Abstract

In the recent past a number of programs have focused on developing AMTEC technology associated with its fabrication and design. The performance level, however, achieved to-date is below the theoretical potential of this device. For improving performance characteristics we examined the sources of power loss and proposed some solution which are demonstrated with computer calculations. Two kind of losses that reduce efficiency are thermal (as a result of thermal conduction and radiation of materials) and electrical (related to the ohmic resistance of material). Each of the losses can, in principle, be reduced separately by varying current in the load. To reduce the thermal losses, the current must be increased; to reduce the electrical losses, the current in the load must be decreased. In such inversely competitive situation an optimum value must be sought which has been achieved by applying the optimization theory. Heat losses due to radiation are reduced by increasing the current density and by reducing the emissivity of electrodes and other surfaces. Changing of some of the materials used in the cell has proved to be helpful in improving the cell performance. As a result of this overall effort we have been able to demonstrate the improvement in the efficiency of AMTEC cell by 77%.

Keywords

Thermal-to-Electrical Conversion, Power Loss, Optimization, Efficiency

INVESTIGATION INTO THE POWER LOSSES FROM AMTEC COMPONENTS

M. A. K. Lodhi

Introduction

A power system considered for a number of potential space missions requires long life, high specific power (power/mass), that is low mass, high areal power density (power/ area), high efficiency, low cost and static in operation. To a great extent a system called Alkali Metal Thermal to Electric Converter (AMTEC) does possess latent qualities that would qualify it to be a possible candidate for space power. It can provide efficiency close to the theoretical Carnot efficiency at relatively low temperatures. AMTEC has conversion efficiency much higher than other direct thermoelectric devices. An optimized AMTEC can potentially provide a theoretical efficiency when operated between 1,000 K to 1,300 K on the hot side and between 400 K to 700 K on the condenser side. It is fuel source insensitive. It can utilize heat as input fuel from most of any source like fossil fuel, the Sun, radioisotopes, or the nuclear reactor. AMTEC, with solar energy as a heat source, is capable of being an alternative to photovoltaic-based power system for use of low earth orbit (LEO) for future NASA and Air Force missions. It is intended to be used for future NASA missions like Pluto Express (PX) and Europa early in the millennium 2000 with radioisotope decay as its heat input.

Since middle sixties a number of programs in developing the operating principle, design and technology of AMTEC has been evolving rapidly. Kummer and Weber demonstrated the conversion of heat, through the sodium cycle, into electricity by the use of beta"-alumina solid electrolyte (BASE) in a patent assigned to Ford Motor Company in 1968 [1]. Several years later Weber described the operating principle of AMTEC with a liquid anode in a historical paper in 1974 [2]. It took some time for the community to recognize the potential qualities of AMTEC with regard to its uses and application for terrestrial and space power. Accordingly, there was not much activity in modeling, design and technology development of AMTEC until almost the beginning of 1990s. During that AMTEC dormant period there were few landmark papers primarily on its principle and working efficiency [3-7]. A review article on the progress of thermionic technology during a ten-year period of 1983-92 covers the slow moving development in AMTEC technology during that period [8]. The use of nuclear power, from the radioisotopes or nuclear reactors, for the space pointing out the potential use of AMTEC perhaps provided another motivation in looking for its application [9-11]. A flurry of AMTEC activities began with a great vigor around the world at the beginning of 1990s. NASA Lewis Research Center (LeRC) has an interest in developing thermal energy storage (TES) for the solar dynamic ground test demonstration (SDGTD) program. The research and development effort at Jet Propulsion Lab (JPL) included studies, which address both overall device construction and investigation into

the AMTEC components [12-25]. Advanced Modular Power Systems (AMPS) have been focusing on designing and manufacturing AMTEC cells for Pluto Express mission [26-27]. Air Force Research Lab (AFRL) has an interest in developing an electrical power system for the payload in low earth orbit (LEO) for a duration of five years and in testing the performance of AMTEC for PLUTO express [28-30]. Orbital Science Corporation has been conducting a series of studies of radioisotopes power system based on general-purpose heat source (GPHS) for potential deep space missions [9,31-33]. AMTEC has been found compatible with direct conversion from the projected SP-10 nuclear space power reactor [10-11]. Recently University of New Mexico has been engaged in modeling and analysis of AMTEC performance and evaluation [34]. In Japan the interest in AMTEC analysis has evolved at Kyushu University in collaboration with Electrotechnical Laboratory [35-36]. Creare Inc. has primarily concentrated on evaporator component of AMTEC to enable it operate efficiently [37-39].

While these programs resolved a number of key technological issues associated with the design and fabrication of AMTEC successfully, the performance level achieved hitherto is still below the theoretical potential of this device. In tracking down the source of power loss during the test cell performance of various AMTEC designs the major losses are found to be radiative and conductive. Since the cell is tested in vacuum there is no convective loss. Most of the heat escapes through the cell wall. There are radiative losses due to condenser and along the artery as well. In order to minimize these losses we propose to use some different materials which should be compatible with the operating conditions of the cell and capable of reducing these losses. We select a test AMTEC cell designated by PX-3A, which has been in operation at US Air Force Research Laboratory since July 9, 1997 and compare its theoretical performance as a function of the variation in the material parameters.

Principle and Working of AMTEC Cell

A typical AMTEC cell is shown in Fig. 1 schematically. An AMTEC cell is a static device for the conversion of heat to electricity performing two distinct cycles: 1) conversion of heat to mechanical energy via a sodium-based (or any suitable alkali metal) heat engine and 2) conversion of mechanical energy to electrical energy by utilizing the special properties of the beta" aluminum solid electrolyte (BASE) material. It has the potential for reliable long life operation and high conversion efficiency. The general principles governing the operation of an AMTEC cell have been given quite elaborately in the early stages of its development [1-5]. The essential thermodynamic aspects of the sodium-based engine have been described in those references. Accordingly a brief outline will be presented here for the self-consistency of this work.

AMTEC, a relatively new type of device, is based on the principle of a sodium concentration cell, conceived in late sixties [1-4]. A closed vessel is divided into a high temperature, high-pressure region in contact with a heat source and a low temperature, low pressure region in contact with a heat sink. A barrier of a BASE sheet whose ionic conductivity is much larger than its electronic conductivity separates these regions. The BASE is coated with a porous metal electrode (cathode) which covers the low-pressure surface of the BASE. A closed container is partially filled with a small quantity (typically <10 g) of liquid sodium as the working fluid. Sodium ions disperse through the BASE in response to the pressure differential (gradient of Gibbs free energy). Electrical leads are connected with the porous cathode and with the high temperature liquid (vapor) sodium, which acts as the anode. When the circuit is closed electrons flow to the porous anode surface through the load, producing electrical work. A return line and electromagnetic pump or a wick circulates the sodium from the cold zone (condenser) to the hot zone (heater) of AMTEC. It is limited to 1350 K because of sodium interaction with the BASE. The lower temperature region is limited to a minimum of 500 K by the need of maintaining the sodium in the liquid state (but it would be operating around 623 K for high efficiency). As the condenser temperature increases above 700 K the efficiency decreases [3].

The main component of an AMTEC cell is the BASE tube which essentially conducts sodium ions much more rapidly than what it does for neutral sodium atoms or negative particles like electrons. A sodium pressure difference across a thin BASE tube drives sodium ions from the high-pressure side to the low-pressure side. Thus positively charged sodium ions concentrate on the low-pressure side while negatively charged particles, electrons remain concentrated on the high-pressure side (inside the BASE tube), resulting an electrical field gradient across the BASE tube. This gradient balances the sodium pressure differential thus preventing the further flow of sodium ions. This electrical potential difference is utilized to drive an electric current through a load by applying some appropriate electrodes at the two ends of the tube. The unusual properties of the BASE provide a method of converting the mechanical energy, represented by the pressure differential, into electrical energy. Or in other words the BASE converts a chemical potential difference into an electrical potential difference. As the electrons, after going through the load, reunite with sodium ions they form neutral sodium atoms in the vapor state on the low-pressure side. The sodium vapor travels to the condenser where it condenses into liquid state. The sodium liquid is pressurized through a wick or electromagnetic pump and is returned to the high-pressure side of the BASE. In that way the thermal-to-mechanical-to-electrical conversion process is completed. The efficiency of this final conversion is governed by variety of irreversible kinetic and transport processes occurring at the electrode interfaces, within the BASE material, internal impedance, and thermal conduction and radiation losses [12-14]. A number of efforts are underway to develop practical and high efficiency cells [18, 40-45]. AMPS, in collaboration with AFRL, has been manufacturing and testing for improving efficiency of PX series of AMTEC cells [26-30]. The latest multi-tube AMTEC cells have been in operation for some time. The longest in operation among them is PX-3A whose parameters are given in Table 1. We have modified it

theoretically for improving efficiency by varying parameters governing its material properties for optimum conditions in a computer model of the cell to predict its performance.

AMTEC Theory and Analysis

The transport of sodium through an AMTEC cell is a complex phenomenological process. Its exact detailed analysis is very difficult and is further complicated as it requires the simultaneous solution of thermal, fluid flow, and electrical equations. Those equations are interdependent, with each of the three analyses requiring the results of the other two. This interdependence is between a number of axially varying distribution functions. (Had it been between single-valued variables ; it could have been solved by a set of simultaneous algebraic equations.) Specifically , solving for the cell's temperature distribution requires the knowledge of the axial variation of the sodium flux through the BASE tube and of the electrical output power density profile over the tube length. Solution of the axial pressure variation of the low-pressure sodium requires knowledge of the cell's temperature distribution and the BASE tubes' current density variation. Similarly, solving for the axial variation of the current density and of the inter-electrode voltage requires prior solution of the axial variation of the BASE tube temperature and internal-to-external pressure ratio. Those interdependent distribution functions require solutions of coupled differential and integral equations by a more sophisticated procedure. Schock *et al* [32] generated a thermal analysis model for multi-tube AMTEC cell by appropriately modifying the ITAS and SINDA codes [46,47].

Energy conversion devices have few equilibria and are typically open systems unlike the classical thermodynamics which is restricted to reversible and closed systems. Onsager's treatment of irreversible processes, such as diffusion, can be applied to AMTEC operation to deal with its irreversibility of the process and openness of the system. One can write, in principle, the effective emf, V as a function of cell voltage in open-circuit, V_{OC} and electrode polarization over potential, $V_{Op} = (\xi^a - \xi^c)$ [2] from Nernst equation [5]. The open-circuit voltage and charge-exchange current density are related with the cell temperature and pressure [19]. We can thus write for the net power output as:

$$P_{out} = VI, \quad (1)$$

where

$$V = V_{OC} - JR_{int} - V_{Op}, \quad (2)$$

$$V_{OC} = RT_B/F \ln P_a/P_c, \quad (3)$$

R is the gas constant = 8.314 J/mol.K. T_B is the temperature of the BASE tube, P_a and P_c are the pressures at the anode and cathode sides respectively. I is the net current in the circuit and R_{int} is the total internal

resistance of the cell including the contact resistance of the electrodes R_{contact} , sheet resistance in the plane of electrodes R_{sheet} , resistance of the current collectors $R_{\text{collector}}$, resistance of the bus wires and conductor leads to the load R_{bus} , the resistance for charge exchange polarization losses at the BASE-electrodes interfaces R_{op} , and the BASE ionic resistance, R_B given by:

$$R_B = \rho_B t_B \quad (4)$$

where ρ_B and t_B are electrical resistivity, the expression for which has been developed by Steinbruck [49], and the thickness of BASE tube respectively. R_{int} will be written here as the sum of the terms in the same order as stated above:

$$R_{\text{int}} = R_{\text{contact}} + R_{\text{sheet}} + R_{\text{collector}} + R_{\text{bus}} + R_{\text{op}} + R_B \quad (5)$$

Heat Losses

For a multitube AMTEC cell, the heat losses are shown in Figure 1. The most of the heat passes the cooling fluid (air) through the condenser. The heat passes the cooling fluid, Q_{air} , is result of heat conduction, heat radiation and condensation of vapor sodium as:

$$Q_{\text{air}} = Q_{\text{wall}} + Q_{\text{artery}} + Q_{\text{rcond}} + Q_{\text{cond}} - Q_{\text{cold}} \quad (6)$$

where Q_{wall} is the conducted heat to condenser through the cell wall, Q_{artery} is conducted heat through the artery, Q_{rcond} is net radiated energy between the condenser and other surfaces, Q_{cond} is latent heat of condensation of sodium, and Q_{cold} is heat conduction loss at edge of cold plate. These heat losses can be expressed in the following expressions:

$$Q_{\text{wall}} = k_{\text{wall}} A_{\text{wall}} (dT/dx)_{x=\text{at condenser}} \quad (7)$$

$$Q_{\text{artery}} = k_{\text{artery}} A_{\text{artery}} (dT/dx)_{x=\text{at condenser}} \quad (8)$$

$$Q_{\text{cond}} = h_{fg} \dot{m} \quad (9)$$

where k is thermal conductivity, A is area, h_{fg} is latent heat of condensation of sodium per unit mass and \dot{m} is sodium flow rate. For wall and artery dT/dx is the temperature gradient at the condenser. As an enclosure, every surface in the cell effects heat radiation. Net radiated energy between the condenser and other surfaces depends on view factors F_{ij} , emissivities ϵ_i , and temperatures T_i for every surfaces, so it can be expressed as

$$Q_{\text{rcond}} = f(\epsilon_1, \epsilon_2, \epsilon_3, \dots, T_1, T_2, T_3, \dots, F_{11}, F_{12}, F_{13}, \dots) \quad (10)$$

Some heat goes to ambient through cell wall and insulation; and it can be given as

$$Q_{\text{insul}} = \int_{x=0}^{x=\text{cell length}} K(x)P[T_{\text{wall}}(x) - T_{\text{insul}}(x)]dx \quad (11)$$

where $K(x)$ is some constant which includes conduction and radiation effects, and P is the perimeter of cell wall. T_{wall} and T_{insul} are cell wall temperature and insulation temperature which change along the cell length. Heat conduction loss at edge of cold plate, Q_{cold} , can be calculated similar to Q_{insul} taking temperature T_{cond} instead of T_{wall} , but Q_{cold} is small. The total of heat losses become

$$Q_{\text{loss}} = Q_{\text{air}} + Q_{\text{insul}} + Q_{\text{cold}} \quad (12)$$

The overall conversion efficiency of AMTEC cell is given by [5,50]:

$$\eta = P_{\text{out}}/Q_{\text{input}} \cong VI / [VI + Q_{\text{loss}}] \quad (13)$$

In order to get the maximum efficiency the total heat losses, Q_{loss} , must be minimum. This implies that:

- The choice of working fluid be such that its latent heat of condensation must be low
- The emissivities of materials used for BASE tube, outer condenser surface, outer artery surface, inner cell wall and radiation shields must be low for minimizing radiation losses
- For conductive losses through the wall, artery and insulation, low thermal conductive materials must be used, but for hot plate high thermal conductivity material must be used.
- The output power maximizes when the load resistance is equal to the internal resistance of the cell. This implies that the load resistance should match the internal resistance for the best results.

We then proceeded with these constraints as input data for the computer program in order to get the resulting output power and efficiency

Results

I consider the parametric properties of materials in our optimization analysis. The effects of material on electrical power generated by the PX-3A cell, the amount of the heat supplied to the cell, the efficiency of the cell, and the losses from the cell are given in figures 2-9. The temperature maintained at the hot plate is 1173 K, and at the condenser side is 623 K for all these cases. In these figures the dotted line shows the values for original PX-3A cell. The maximum power generated by the cell is given in Table 2. Some other relevant parameters for the maximum power are given in the same table. Also heat losses are given as the percentage of the Q_{input} . The following material changes are made for the cell to compare the results:

Case A: material for hot plate, stud and evaporator is changed from SS to Ni

Case B: in addition to case A, the material for condenser, artery, shield and cell wall is changed from SS to Inconel

Case C: in addition to case B, the emissivity of sodium film is changed from 0.05 to 0.025; because the emissivity of liquid sodium is given as 0.02 in [51]

Case D: in addition to case C, cell wall and artery coated with Rh ($\epsilon=0.06$)

Case E: in addition to case D, material for cell wall above the BASE tube is changed from SS to ceramic, ZrO_2

Case F: in addition to case E, perfect insulator is assumed as a insulation material instead of Molded Mink-K.

In Fig. 2, it can be seen that the electrical power generated by the cell increases appreciably for case A. In this case the maximum power reaches from 4.49 W to 5.97 W. For cases B, C, D, E and F, the electrical power increases slowly. The maximum power in case F is obtained as 6.26 W. Heat input to the cell versus current is given in Fig. 3. The maximum heat goes into the cell in case A because Ni has higher thermal conductivity than SS. For case B, the amount of heat supplied to the cell, Q_{input} , decreases because of the Inconel's lower thermal conductivity which impedes the loss of heat through walls and condenser. Depending on heat losses, Q_{input} goes down for cases C, D, E and F; and it takes the minimum values in case F.

The cell conversion efficiency versus current is given in Fig. 4. The maximum efficiency is 12.98% for original cell, the maximum efficiencies for cases A through F are substantially increased around the current 2-2.5 A. They are given in Table 3. Heat losses through cell wall and insulation, Q_{insul} , through artery, Q_{artery} , and through cell wall, Q_{wall} , are given in Figures 5-7. They show higher values from original cell in cases A, B and C, but smaller values in cases D, E and F. Heat loss in case F is minimum for Q_{insul} , but in case of Q_{artery} and Q_{wall} the minimum is for case E. In case F, the perfect insulator is assumed for insulation material. It means there is no heat losses through cell wall and insulation. That time temperatures of the cell elements (wall, evaporator, BASE tube, artery,.....) become higher (Table 3). Therefore Q_{artery} and Q_{wall} will increase when Q_{insul} become zero. As the conducted heat losses through artery for cases D and E are almost the same, the conducted heat losses through the cell wall for cases D and E show big difference. Because the ceramic material ZrO_2 is considered only for cell wall not for artery, in case E. The ZrO_2 has lower thermal conductivity than SS has (for ZrO_2 2.5 W/mK and for SS 25 W/mK at 1000 K). The net heat radiation to condenser increases for cases A and B, but it decreases for other cases comparing to original cell. Depends on the low sodium film emissivity ($\epsilon=0.025$), it takes the smallest values in case C.

Although the sodium film emissivity is the same for cases D, E and F, Q_{rcond} increases because of higher temperatures of cell elements (Fig. 8). The condensation heat losses, Q_{cond} are almost same values in all cases as should be expected, see Fig. 9.

Conclusion

We have been able to reduce the losses almost on all counts thereby increasing the output power and thus the efficiency of AMTEC. The efficiency has improved considerably when we incorporate the variation in the material used in the cell. Besides we make the following recommendations:

- The interior cell wall could be coated with some appropriate material with high reflective coefficient and low emissivity
- The cell wall could be made of double layers with air in between
- The artery's outer surface should be coated with the same material used for the cell wall coating
- Condenser may be coated with sodium also
- The power output maximizes at a certain value of the current in the circuit, and when the load resistance matches the internal resistance of cell. For best results the cell must be operated under those conditions.
- For conductive losses through the wall, artery and insulation, low thermal conductive materials must be used, but for hot plate high thermal conductivity material is recommended.
- A PX-3A AMTEC cell has been in operation at US Air Force Research Lab, Albuquerque NM since July 9, 1997 [52]. It had about 16% degradation in performance in less than first 500 hours of operation. This degradation is attributed to the maturing of electrodes. The cell degradation continues after the electrode maturing period, though at a slower pace, see Fig. 10. The cell performance can, in principle, be enhanced by decreasing the parasitic heat losses.

Acknowledgment

I am indebted to Clay Mayberry and John Meril for Providing the AMTEC data before publication and Dr. Jean-Michel Tournier for many useful discussions. This work is based in parts supported by AFOSR Sub-contract 99-0832 CFDA #12.800

References

1. J.T.Kummer and N. Weber, U.S. Patent 3,458,356, Assigned to Ford Motor Co, (1968).
2. N. Weber, *Energy Conversion*, **14**, 1 (1974).
3. T. K. Hunt, N. Weber and T. Cole, in *Proceeding of the 13th Intersociety Energy Conversion Engineering Conference*, SAE, p. 2001, Warrandale, PA (1978).
4. Hunt, T. K., N. Weber, and T. Cole, in *Solid State Ionics*, J. B. Bates and G. C. Ferrington, Editors, p. 263, North Holland Pub. Co., Amsterdam (1981).
5. T. Cole, *Science*, **221**, 915 (1983).
6. R. Ewell and J. Mondt, in *Space Nuclear Power Systems 1984*, M. S. El-Genk and M. D. Hoover, Editors, p. 385, Orbit Book Co., Malabar, FL (1985).
7. C. P. Bankston, T. Cole, S. K. Khanna, and A. P. Thakoor, in *Space Nuclear Power Systems*, M. S. El-Genk and M.D. Hoover, Editors, p. 393, Orbit Book Co., Malabar, FL (1985).
8. Dahlberg, R. C., *et al*, "Review of Thermionic Technology 1983 to 1992," "A Critical Rev of Space Nuclear Power and Propulsion 1984 -1992", Ed. M. S. El-Genk (AIP Press, NY 1994) pp 121-161
9. A. Shock, in *Proc. 15th Intersociety Energy Conversion Engineering Conference*, Vol. 2, p. 1032, AIAA, NY (1980).
10. D. Birden and F. A. Angelo, in *Proc. 18th Intersociety Energy Conversion Engineering Conference*, p. 61, AICHE, N.Y. (1983).
11. E. J. Brat and G. O. Fitzpatrick, *Direct Conversion Nuclear Reactor Space Power Sy.*, Report No. AFWALTR-82-2073, Vol 1
12. R. M. Williams, B. Jeffries-Nakamura, M. Underwood, B. Wheeler, M. Loveland, S. Kikkert, J. Lamb, T. Cole, J. Kummer, and C. P. Bankston, *J. Electrochem. Soc.*, **136**, 893 (1989).
13. R. M. Williams, M. E. Loveland, B. Jeffries-Nakamura, M. L. Underwood, C. P. Bankton, H. Leduc and J. T. Kummer, *J. Electrochem. Soc.* **137**, 1709 (1990).
14. R. M. Williams, B. Jeffries-Nakamura, M. L. Underwood, C. P. Bankton and J. T. Kummer, *J. Electrochem. Soc.* **137**, 1716 (1990).
15. M. A. Ryan, B. Jeffries-Nakamura, R. M. Williams, M. L. Underwood, D. O'Connor, and S. Kikkert, in *Proc. 26th Intersociety Energy Conversion Engineering Conference*, American Nuclear Society, **5**, 463 (1991).
16. M. A. Ryan, R. M. Williams, B. Jeffries-Nakamura, M. L. Underwood, and D. O'Connor, *JPL New Technology Report* , 18620-8166 (1991).
17. M. A. Ryan, B. Jeffries-Nakamura, D. O'Connor, M. L. Underwood, and R. M. Williams, in *Proc. Symposium on High Temperature Electrode Materials and Characterization*, D. D. Macdonald and A. C. Khanker, Editors, *Electrochem. Soc.* **91-6**, 115 (1991).

18. C. B. Vinning, R. M. Williams, M. L. Underwood, M.A. Ryan, and J.W. Suiter, in *Proc. 27th Intersociety Energy Conversion Engineering Conf.*, Society of Automobile Engineers, **3** , 123, (1992).
19. M. L. Underwood, R. M. Williams, M. A. Ryan, B. Jeffries-Nakamura, and D. O'Connor, in *Proc. 9th Symp. On Space Nuclear Power Systems*, M. S. El-Ghenk and M. D. Hoover, Editors, American Inst. Phys. **3**, 1331 (1992).
20. M. L. Underwood, D. O'Connor, R. M. Williams, B. Jeffries-Nakamura and M. A. Ryan, in *Proc. 27th IECEC*, **3**, 197 (1992).
21. M. L. Underwood, B. Jeffries-Nakamura, D. O'Connor, M. A. Ryan, J. W. Suiter, and R. M. Williams, in *Proc. 28th IECEC*, **1**, 855 (1993).
22. M. A. Ryan, R. M. Williams, B. Jeffries-Nakamura, M. L. Underwood, and D. O'Connor, *NASA Tech. Briefs*, p. 80, (1993).
23. M. A. Ryan, R. M. Williams, C. Spaipetch, A. Kisor, D. O'Connor, M. L. Underwood, and B. Jeffries-Nakamura, CONF940101, AIP Press, NY, p. 1495 (1994).
24. M. A. Ryan, A. Kisor, R. M. Williams, B. Jeffries-Nakamura, and D.O'Connor, in *Proc. 29th IECEC*, **2**, 877 (1994).
25. M. A. Ryan, R. M. Williams, M. L. Phillips, L. Lora, and J. Miller, in *Proc. Space Technology and Applications International Forum-1998*, M. S. El-Ghenk, Editor, p.1607 (AIP Press, NY), (1998).
26. R. K Sievers, T. K. Hunt, J. F. Ivanenok, J. Pantolin, and D. A. Butkiewicz, in *Proc. 10th Space Nuclear Power and Propulsion*, CONF-930103, M. S. El-Genk and M. D. Hoover, Editors, p. 319 (AIP Press, NY) (1993).
27. R. K. Sievers, J. R. Rasmussen, C. A. Barkowski, T. J. Hendricks, and J. E. Pantolin, in *Proc. STAIF-98*, CONF-980103, p.1479 (AIP Press, NY), (1998).
28. M. J. Schuller, P. Haugen, E. Reiners, J. Merrill, R. K. Sievers, R. Svedberg, J. F. Ivanenok, III, C. J. Crowley, and M. G. Izenon, in *Proc. 31st IECEC*, IEEE, paper no. 96184, **2**, 877 (1996).
29. J. Merrill, M. J. Schuller, R. K. Sievers, C. A. Borkowski, L. Huang, and M. S. El-Genk, in *Proc. 32nd IECEC*, IEEE, paper no. 97379, **2**, 1184 (1997).
30. J. M. Merrill, M. Schuller, and L. Huang, in *Proc. STAIF*, M. S. El-Genk, Editor, CONF-980103, (AIP Press NY) 1613, (1998).
31. A. Schock, in *Proc. 15th Intersoc. Energy Conversion Engineering Conf.*, 1032 (1980).
32. A. Schock, H. Norivan, C. Or, and V.Kumar, in *Proc. 48th Intl. Astronomical Congress*, **1** (1997)

33. A. Schock, H. Norivan, C. Or, and V.Kumar, Preprint for presentation in 33rd Intesoc. Energy Conversion Engineering Conf. (1998)
34. J. M. Tournier and M. S. El-Ghenk, in *Proc. 15th STAIF*, (AIP Press NY) 1576 (1998).
35. A. Kato, Nakata, and K. Tsuchida, in *Proc. 27th IECEC*, American Chemical Soc., Paper No. 929006, p. 1, (1992).
36. A. Kato, Nakata, and K. Tsuchida, in *Proc. 28th IECEC*, American Chemical Soc., Paper No. 93027, p. 809, (1993).
37. C. J. Crowley and M. G. Izenzon, in *Proc. 10th Symp. On Space Nuclear Power and Propulsion*, CONF-930103, M. S. El-Genk, Editor, (AIP Press, NY), 897 (1993).
38. M. G. Izenzon and C. J. Crowley, in *Proc. 28th Intersociety Energy Conversion Engineering Conference*, Paper no. 93221, American Chemical Society, 1: p. 829, (1993).
39. M. G. Izenzon and C. J. Crowley, in *Proc. 31st Intersociety Energy Conversion Engineering Conference*, Paper no. 96262, IEEE, 4, p. 2226 (1996).
40. M. Sayer, M. F. Bell, and B. A. Judd, *J. Applied Physics*, **67**, 832 (1990)
41. M. L. Underwood, D. O'Connor, R. M. Williams, M. A. Ryan, and C. P. Bankston, *J. Propulsion and Power*, **8**, 878 (1993).
42. M. L. Underwood, R. M. Williams, M. A. Ryan, and B. Jeffries-Nakamura, in *Proc. Space Nuclear Power and Propulsion*, CONF- 930103, M. S. El-Genk and M. D. Hoover, Editors, p. 885, AIP, (1993).
43. A. Schock, H. Noravian, V. Kumar, and C. Or, in *Proc. 32nd Interdisciplinary Energy Conversion Conf.*, #97529 ,2,1136 (1997).
44. M. A. K. Lodhi, Michael Schuller, and Paul Housgen, in *Proc. Space Techology and Applications International Forum*, M. S. El-Genk, Editor, p. 1285, (AIP Press, NY), (1996).
45. M. S. El-Ghenk, and J-M. Tournier, in *Proc. 5th ESPC-98*, 416 , p. 257, (1998).
46. H. Noravian, in *Proc. 26th International Conference on Environmental Systems*, No. 961376, (1996).
47. J. Gaski, *SINDA (System Improved Numerical Differencing Analyzer)*, vers. 1.315 from Network Analysis Associate, Fountain Valley, CA, (1987).
48. A. M. Straus, and S. W. Peterson, in *Proc. STAIF*, p.1571, (1998).
49. M. Steinbruck, V. Heinzl, F. Huber, and W. Pepler, in *Proc. 28th IECEC I.1*, 799, (1993).
50. C. J. Crowly, M.G. Izenzon, P. N. Wallis, R. K. Sievers, and J. F. Ivanenok III, in *Proc. 29th IECEC*, Vol.1, p. 882, AIAA, (1994).
51. J. M. Tournier, M. S. El-Ghenk, M. Schuller, and P. Hausgen, in *Proc. 14th STAIF-97*, 397, (1997).
52. J. M. Merrill, M. Schuller, and L. Huang, *15th STAIF*, (AIP Press NY) 1613 (1998).

LIST OF SYMBOLS

A_{artery}	cross-section area of artery (m^2)
A_{wall}	cross-section area of wall (m^2)
F	Faraday's constant (96,485 C/mole)
F_{ij}	view factor between surfaces i and j
h_{fg}	latent heat of condensation of sodium per unit mass (J/kg)
I	cell current (A)
J	current density (A/m^2)
k	thermal conductivity (W/mK)
K	coefficient includes conduction and radiation effects (W/mK)
\dot{m}	sodium flow rate (kg/s)
P	perimeter of cell wall (m)
P_a	pressure at anode side (Pa)
P_c	pressure at cathode side (Pa)
P_{out}	electrical energy generated by the cell (W)
Q_{air}	heat passes the air as cooling fluid (W)
Q_{artery}	conducted heat to condenser through artery (W)
Q_{cold}	heat loss at the edge of cold plate (W)
Q_{cond}	latent heat of condensation of sodium (W)
Q_{insul}	heat losses to ambient through cell wall and insulation (W)
Q_{loss}	total heat losses (W)
Q_{rcond}	net radiated energy to condenser (W)
Q_{wall}	conducted heat to condenser through cell wall (W)
R	perfect gas constant (8.314 J/mol.K)
R_{bus}	electrical resistance of bus wire ($\Omega \text{ m}^2$)
R_B	ionic electrical resistance ($\Omega \text{ m}^2$)
$R_{\text{collector}}$	electrical resistance of current collector ($\Omega \text{ m}^2$)
R_{contact}	contact resistance of the electrodes ($\Omega \text{ m}^2$)
R_{int}	total internal resistance ($\Omega \text{ m}^2$)
R_{op}	charge exchange polarization loss ($\Omega \text{ m}^2$)
R_{sheet}	sheet resistance in the plane of electrode ($\Omega \text{ m}^2$)
t_B	thickness of BASE tube (m)
T	temperature (K)
V	Cell voltage (V)

V_{oc}	cell voltage in open-circuit
V_{op}	electrode polarization over potential (V)
x	distance from condenser (m)

Greek

ϵ	emissivity
η	cell conversion efficiency
ρ_B	electrical resistivity (Ω m)
ξ^a	electrode polarization over potential at anode (V)
ξ^c	electrode polarization over potential at cathode (V)

LIST OF TABLES

Table 1. Design Parameters of PX-3A cell.

Table 2. Comparison of heat losses at the maximum power generated by the AMTEC cell.

Table 3. Comparison of maximum conversion efficiency of the AMTEC.

Table 1. Design Parameters of PX-3A cell

Cell diameter (mm)	31.75
Cell height (mm)	101.6
Evaporator type	Deep Cone
Evaporator elevation (mm)	5.18
Evaporator standoff thickness	0.71
Evaporator standoff material	SS
Standoff rings (mm)	1.1
Rings material	Ni
Stud area (mm ²)	38
Stud material	SS
Number of BASE tubes	5
Tube length	32
Electrode/tube (mm ²)	600
Tube braze material	TiNi
Current collector	60-mesh Mo
Feedthrough braze	TiCuNi
Radiation shield type	Circular
Shield material	SS
Condenser type	Creare
Hot side	SS
Cell wall	SS
Initial test date	7/9/97
Operation (hrs)	12,000

Table 2. Comparison of heat losses at the maximum power generated by the AMTEC cell

	Original	Case A	Case B	Case C	Case D	Case E	Case F
P _{out.max} (W)	4.490	5.971	5.995	6.012	6.109	6.135	6.253
I (A)	2.447	3.155	3.161	3.166	3.191	3.198	3.228
η (%)	12.642	13.917	14.278	14.484	15.866	17.067	20.789
Q _{inout} (W)	35.514	42.901	41.987	41.511	38.507	35.944	30.078
Q _{insull} (W)	7.079	7.492	7.487	7.518	7.099	7.118	0.0
Q _{arterv} (W)	3.257	3.550	3.207	3.281	2.299	2.291	2.395
Q _{wall} (W)	5.415	6.423	5.674	5.848	3.746	1.115	1.833
Q _{rcond} (W)	1.300	1.536	1.659	0.860	1.117	1.110	1.246
Q _{cond} (W)	13.495	17.238	17.273	17.298	17.438	17.474	17.643
Q _{insul} (%)	19.932	17.465	17.831	18.112	18.436	19.804	0.0
Q _{arterv} (%)	9.170	8.275	7.639	7.904	5.970	6.374	7.962
Q _{wall} (%)	15.247	14.973	13.951	14.088	9.729	3.103	6.095
Q _{rcon} (%)	3.662	3.581	3.951	2.072	2.900	3.088	4.143
Q _{cond} (%)	38.000	40.180	41.139	41.671	45.286	48.615	58.656

Table 3. Comparison of maximum conversion efficiency of the AMTEC

	Original	Case A	Case B	Case C	Case D	Case E	Case F
I (A)	1.98	2.52	2.52	2.44	2.39	2.32	1.93
η_{\max} (%)	12.98	14.38	14.79	15.02	16.64	18.09	22.99
Improvement in efficiency (%)	-	10.79	13.94	15.72	28.20	39.37	77.12
Minimum BASE temperature (K)	1062	1088	1091	1093	1108	1110	1126
Maximum BASE temperature (K)	1141	1153	1153	1154	1156	1157	1161
Minimum shield temperature (K)	898	928	945	954	1010	1012	1062
Maximum shield temperature (K)	1003	1045	1050	1054	1076	1050	1103
Wall temperature at certain point (K)	1049	1106	1110	1111	1122	1138	1153

FIGURE CAPTIONS

- Figure 1. A schematic diagram of vapor-anode AMTEC cell.
- Figure 2. The electrical power generated by the AMTEC cell.
- Figure 3. The heat supplied to the AMTEC cell.
- Figure 4. The cell conversion efficiency.
- Figure 5. Heat losses to ambient through cell wall and insulation.
- Figure 6. Conducted heat to condenser through artery.
- Figure 7. Conducted heat to condenser through cell wall.
- Figure 8. Radiation heat losses from condenser.
- Figure 9. Latent heat of condensation of sodium.
- Figure 10. Degradation for PX-3A AMTEC cell at different temperatures.

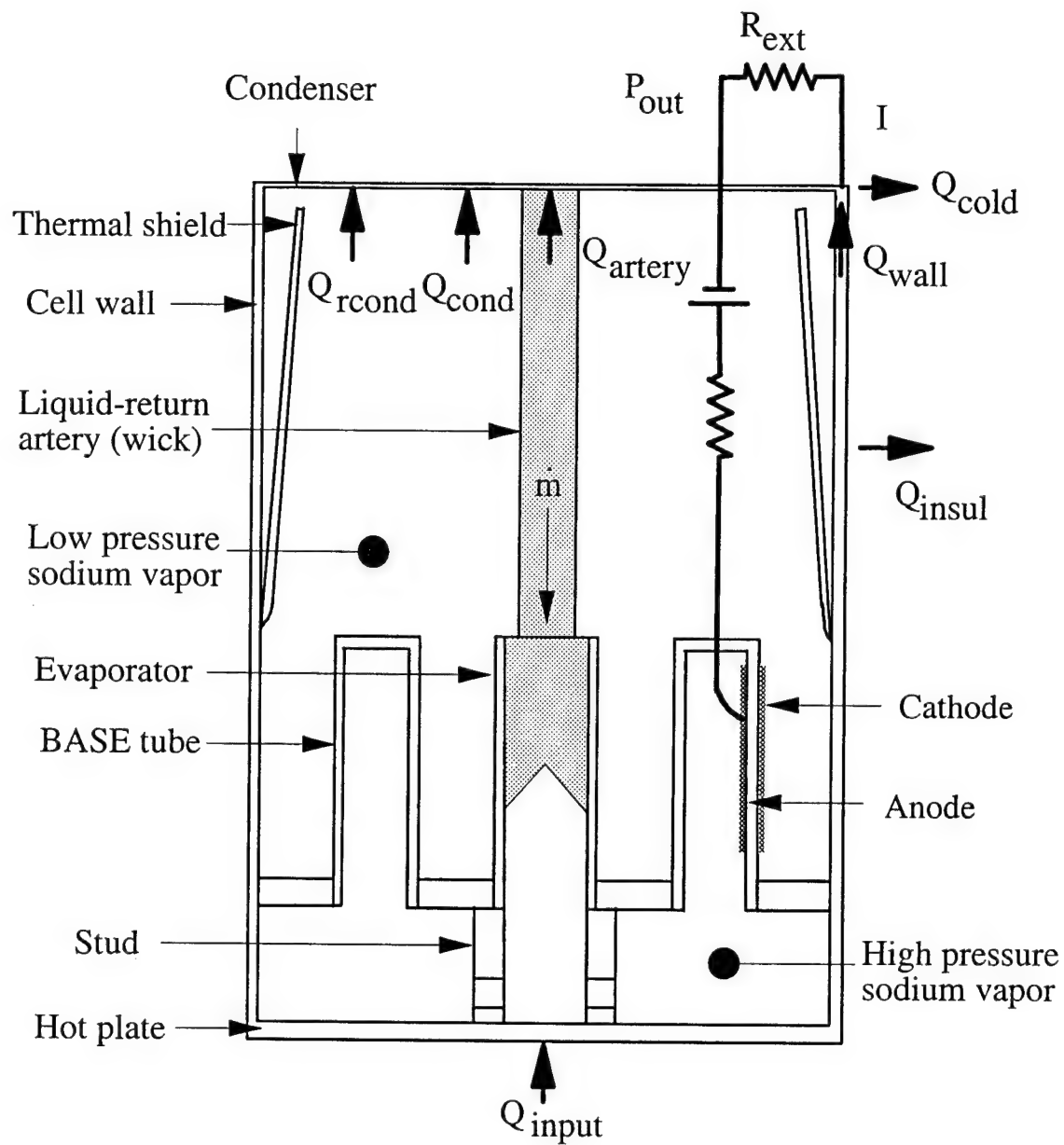


Figure 1. A schematic diagram of vapor-anode AMTEC cell.

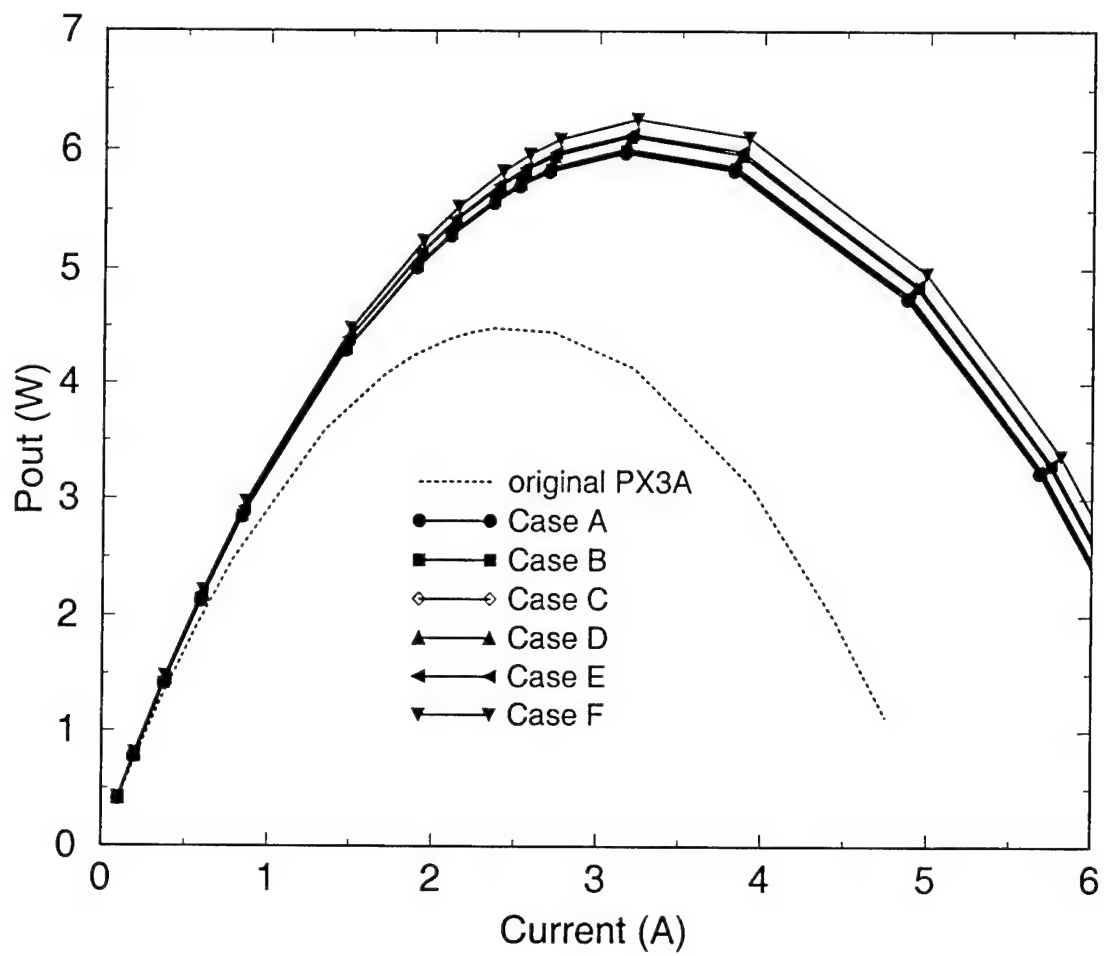


Figure 2. The electrical power generated by the AMTEC cell.

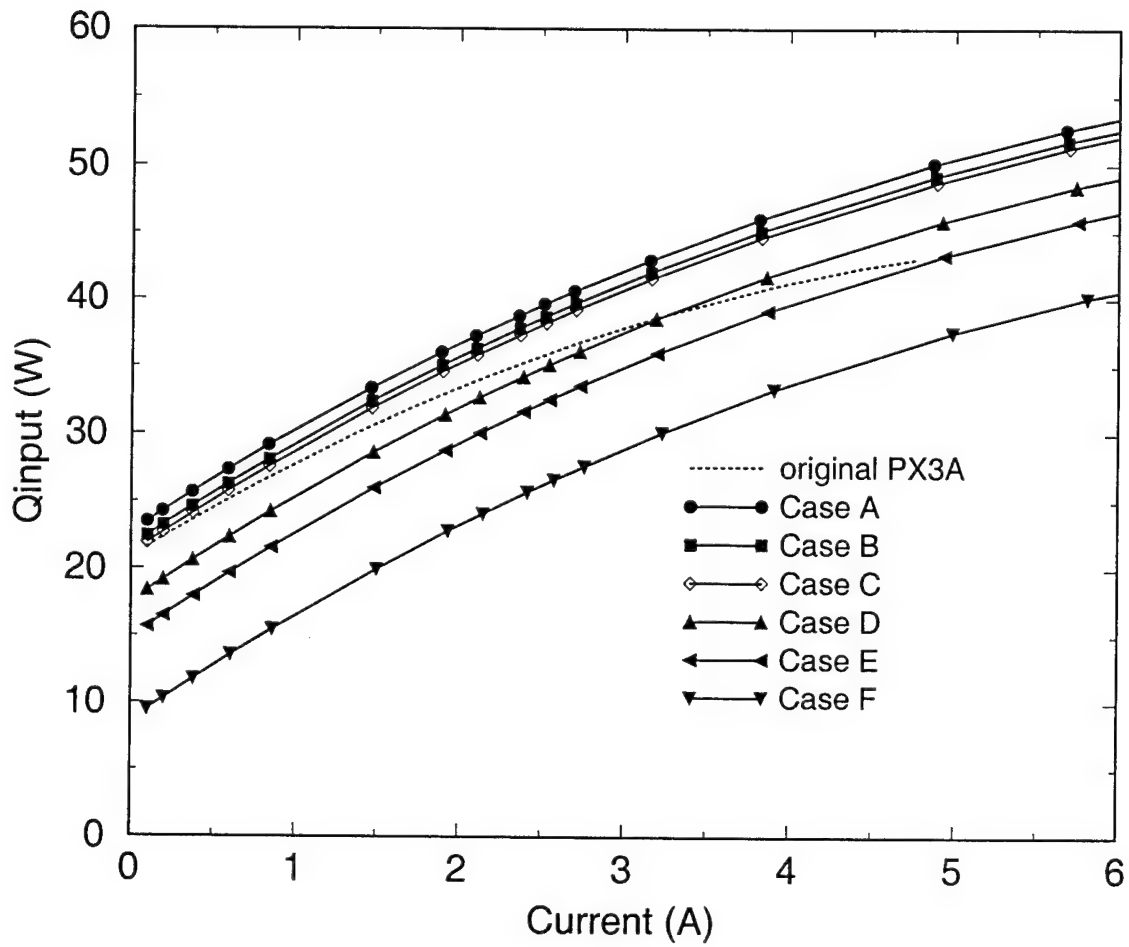


Figure 3. The heat supplied to the AMTEC cell.

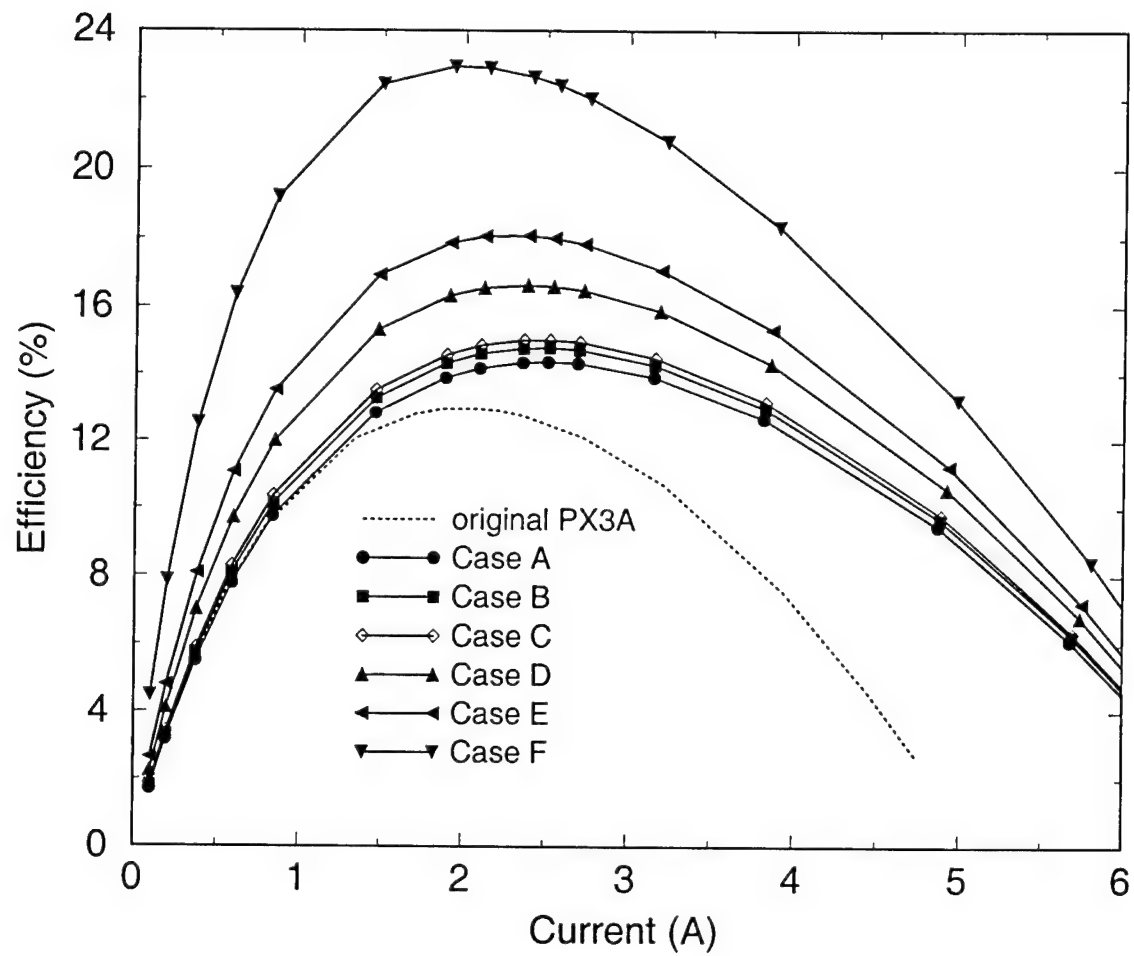


Figure 4. The cell conversion efficiency.

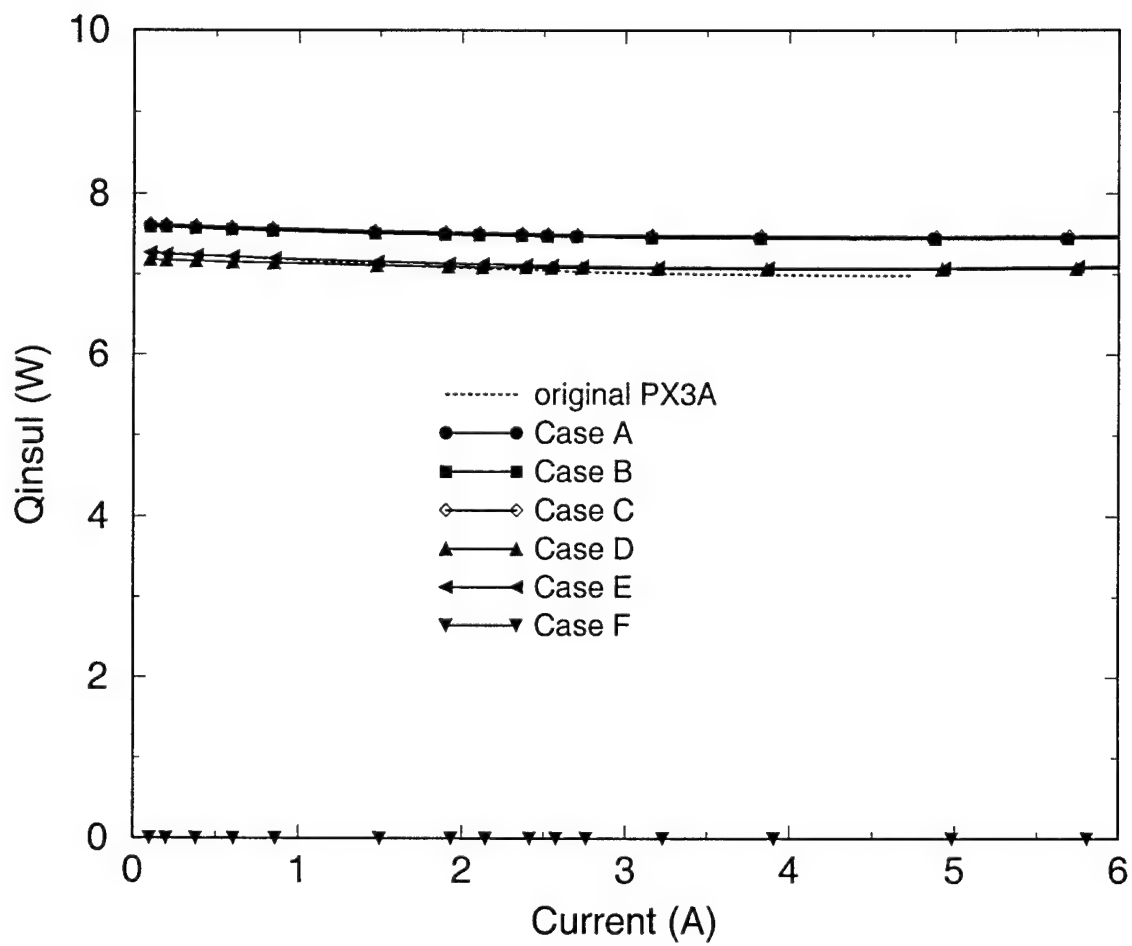


Figure 5. Heat losses to ambient through cell wall and insulation.

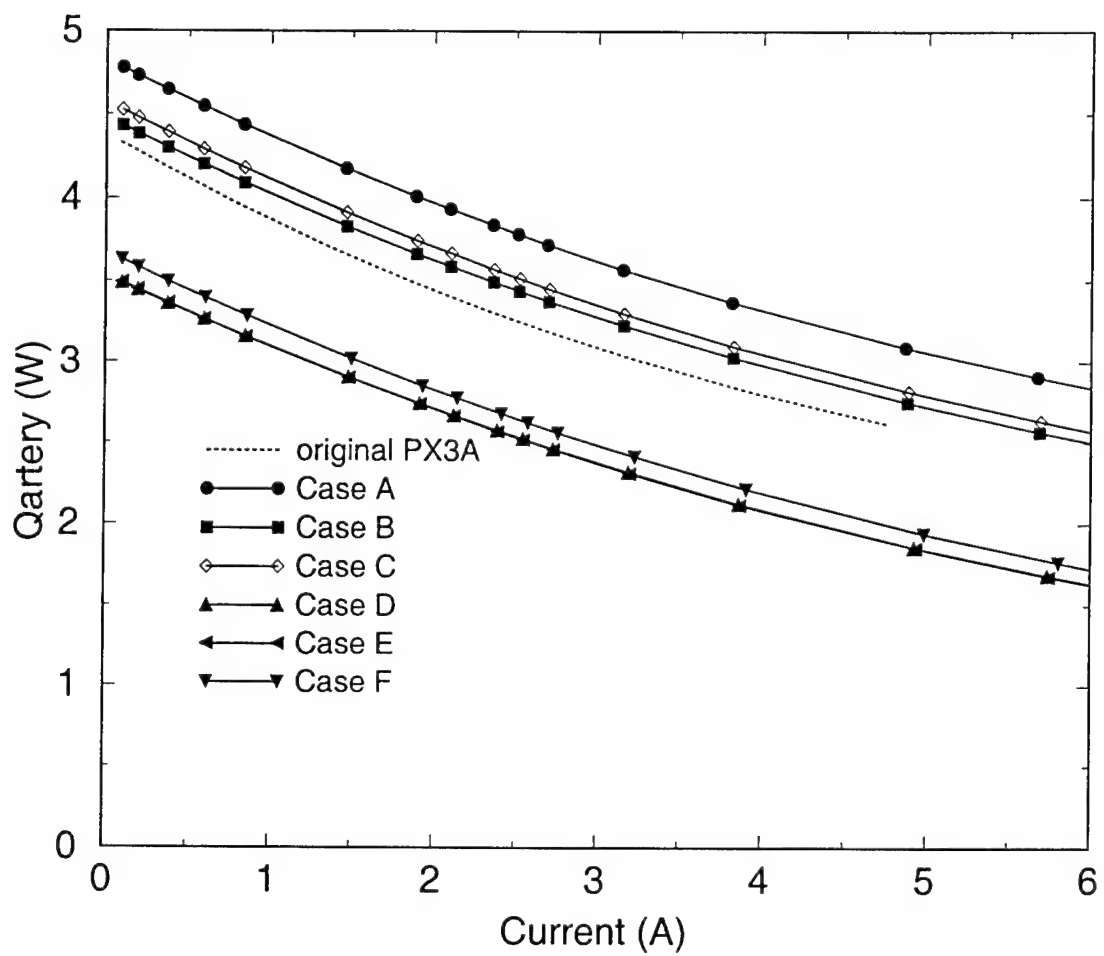


Figure 6. Conducted heat to condenser through artery.

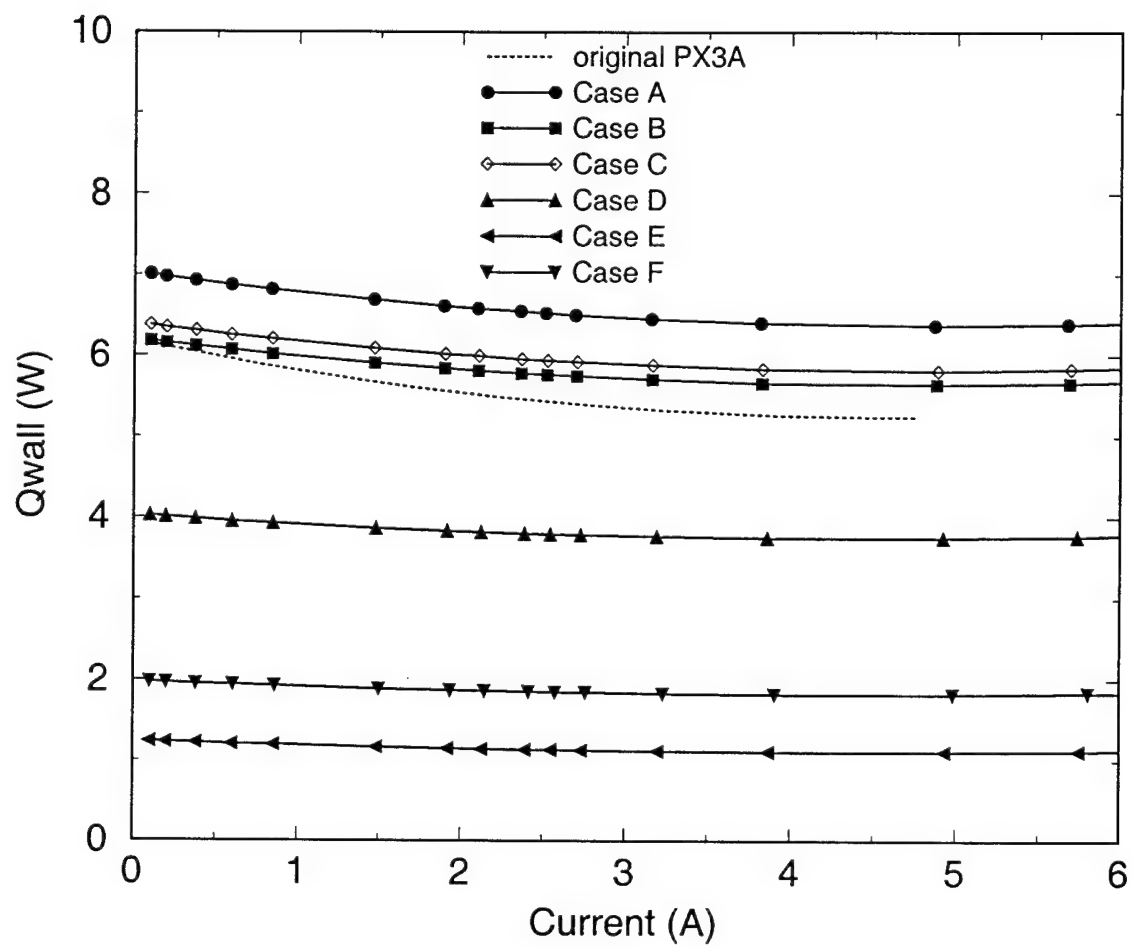


Figure 7. Conducted heat to condenser through cell wall.

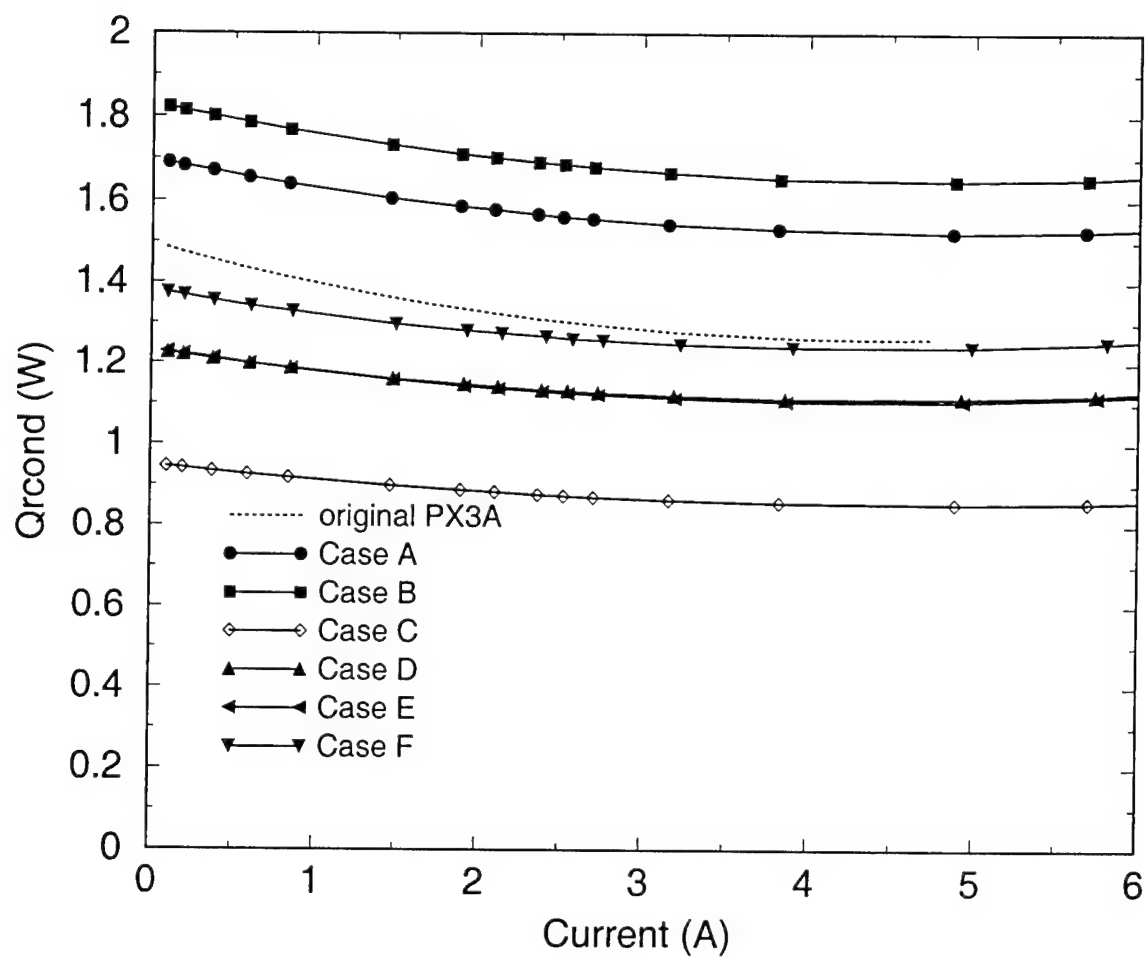


Figure 8. Radiation heat losses from condenser.

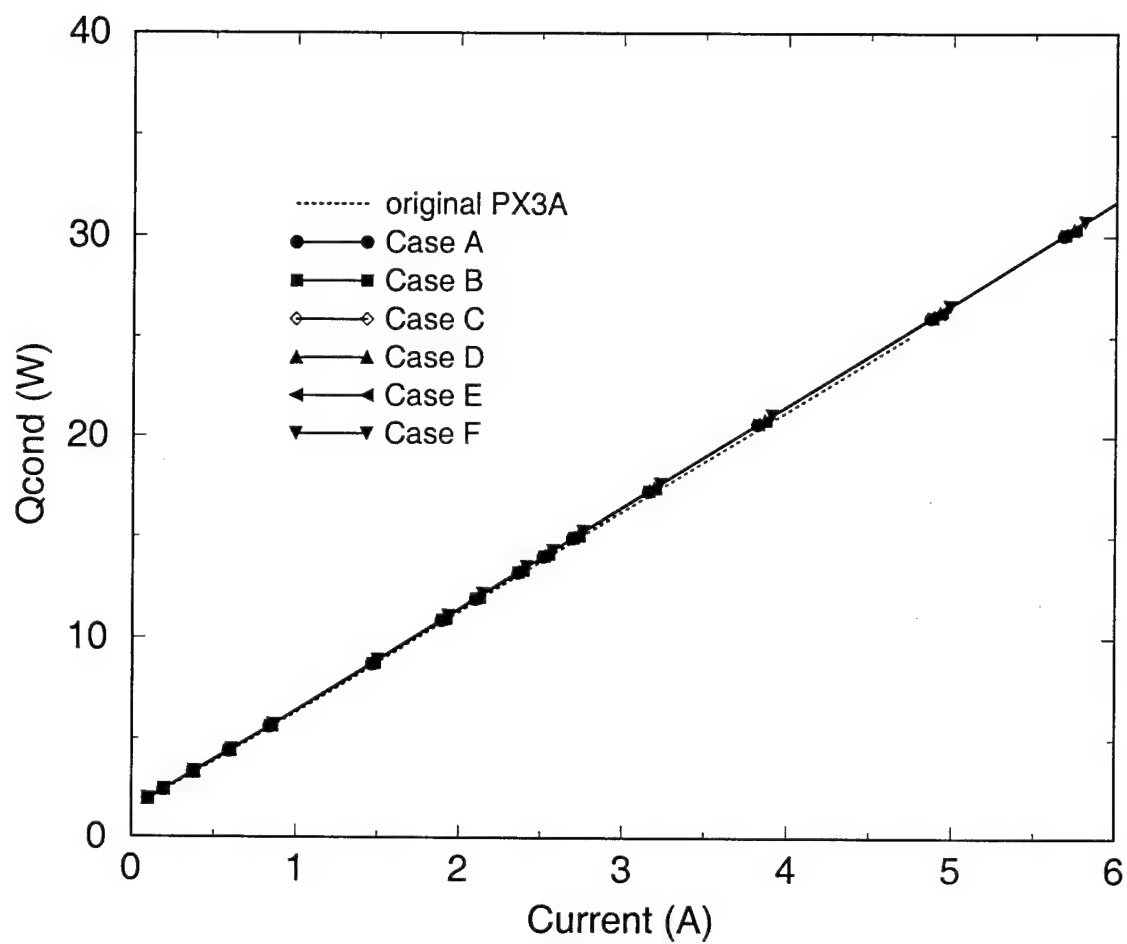


Figure 9. Latent heat of condensation of sodium.

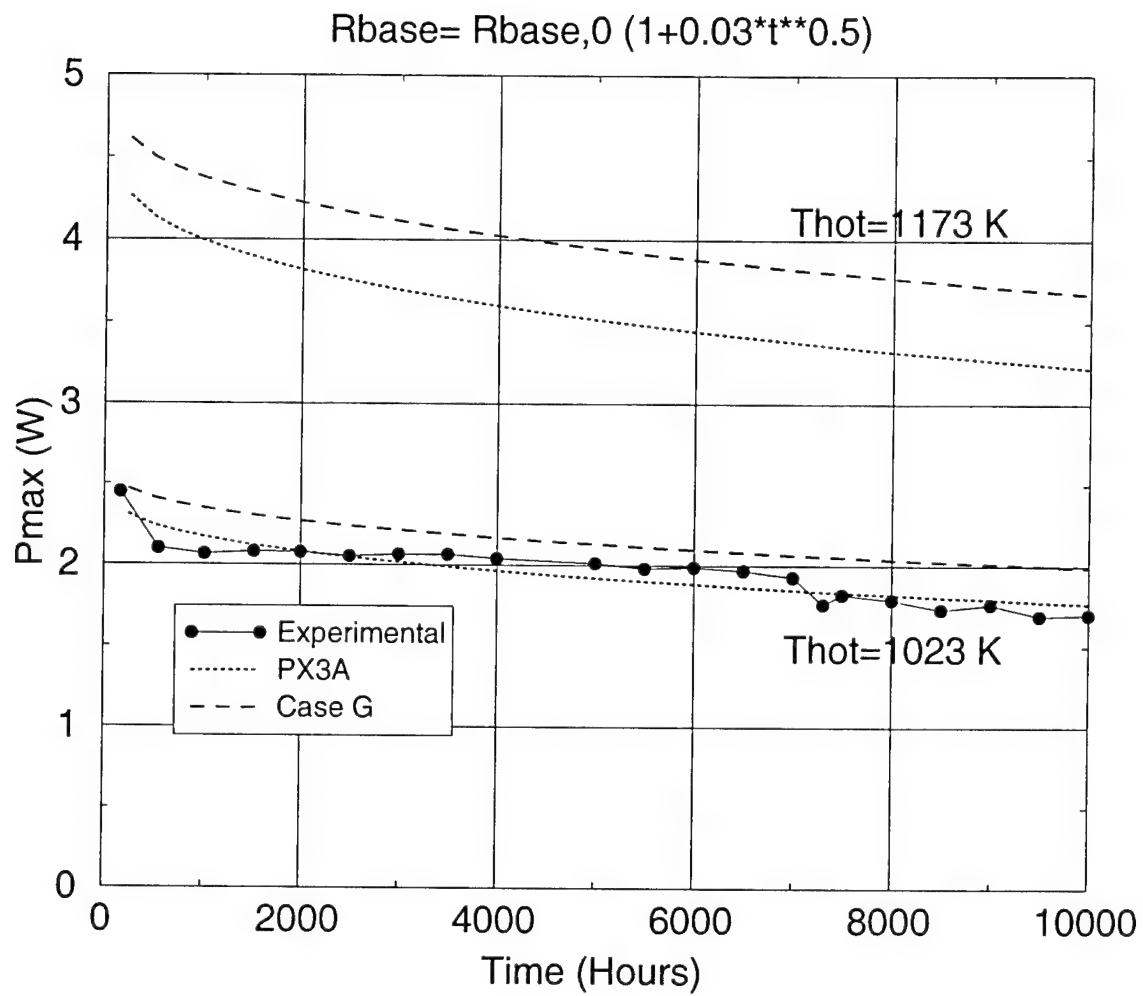


Figure 10. Degradation for PX-3A AMTEC cell at different temperatures.

Dr. John McHugh's report was not available at the time of publication.

**SOLUTIONS OF THE TRANSMISSION LINE EQUATIONS USING
PRODUCT INTEGRALS OF VARIABLE MATRICES**

**Stanly Steinberg
Professor of Mathematics
Department of Mathematics and Statistics**

**University of New Mexico
Albuquerque NM 87131-1141 USA
stanly@math.unm.edu
<http://math.unm.edu/~stanly/>**

**Final Report for:
Summer Research Extension Program
Air Force Research Laboratory**

**Sponsored by:
Air Force Office of Scientific Research
Bolling Air Force Base, DC**

and

Air Force Research Laboratory

February 2000

SOLUTIONS OF THE TRANSMISSION LINE EQUATIONS USING
PRODUCT INTEGRALS OF VARIABLE MATRICES

Stanly Steinberg
Professor of Mathematics
Department of Mathematics and Statistics
University of New Mexico

Abstract

Product integrals and Lie algebraic ideas are used to find useful representations of solutions of variable coefficient differential equations that have applications to transmission-line problems.

SOLUTIONS OF THE TRANSMISSION LINE EQUATIONS USING PRODUCT INTEGRALS OF VARIABLE MATRICES

Stanly Steinberg

1 Introduction

The general transmission-line equations describe the currents and voltages on a tube of transmission lines:

$$\begin{aligned}\frac{dV(t)}{dt} &= -Z(t) I(t) \\ \frac{dI(t)}{dt} &= -Y(t) V(t)\end{aligned}\tag{1.1}$$

where

- t is the position along the tube
- $I(t)$ is the complex current vector with N components
- $V(t)$ is the complex voltage vector with N components
- $Y(t)$ is the N by N complex admittance matrix
- $Z(t)$ is the N by N complex impedance matrix

For more details, see the notes [1] by Baum, Liu, and Tesche. In the applications to transmission lines, the vectors and matrices also depend on s , the complex variable conjugate to time under the Laplace transform. Also, if we find a complete set of analytic solutions then we can easily solve problems with inhomogeneous terms and either initial or boundary conditions, so we do not include these terms in the statement of the problem.

These transmission-line equations (1.1) can be easily written as a single second-order equation for either the currents or the voltages:

$$\frac{d^2 I}{dt^2} - Y' Y^{-1} \frac{dI}{dt} - Y Z I = 0 \quad \text{or} \quad \frac{d^2 V}{dt^2} - Z' Z^{-1} \frac{dV}{dt} - Z Y V = 0,\tag{1.2}$$

where $Y' = dY/dt$ and $Z' = dZ/dt$. It is also useful to write these equations as a system of $2N$ by $2N$ equations:

$$\frac{d}{dt} \begin{bmatrix} V \\ I \end{bmatrix} = - \begin{bmatrix} 0 & Z \\ Y & 0 \end{bmatrix} \begin{bmatrix} V \\ I \end{bmatrix}.\tag{1.3}$$

In fact, the matrices Y and Z cannot be arbitrary. The reciprocity condition requires that

$$Y^T = Y, \quad Z^T = Z. \quad (1.4)$$

To be clear, if the complex conjugate is given by an over-bar, then the adjoint A^* of a matrix A is given by $A^* = \bar{A}^T$ so we do not necessarily have $Y^* = Y$ or $Z^* = Z$. So in the general case we do not assume the matrices are Hermitian (self-adjoint). The condition that there are no infinite physical parameters requires that the Y and Z matrices be invertible, that is,

$$Y^{-1} \quad \text{and} \quad Z^{-1} \quad \text{exist.} \quad (1.5)$$

As noted above, the matrices Y and Z are functions of a parameter s . For appropriate ranges of s , in particular for s purely imaginary, these matrices have positive real part, so we just look at that case and assume that for all vectors V and I

$$\Re(V^T Y V) > 0 \quad \text{and} \quad \Re(I^T Z I) > 0. \quad (1.6)$$

To summarize, we will always assume that the matrices in the (1.1) are symmetric and have strictly positive real part.

There are other special cases of interest. When the materials in the cables are uniform, then the matrices are constant in t ,

$$Y(t) = Y \quad \text{and} \quad Z(t) = Z. \quad (1.7)$$

In the lossless cables case, the vectors and matrices are real for real s and the solutions for all s can be found from $s = \imath$ by rescaling, so we can take

$$Y(t) = \imath L(t) \quad \text{and} \quad Z(t) = \imath C(t). \quad (1.8)$$

where L is the inductance matrix and C is the capacitance matrix and both L and C are symmetric and thus Hermitian (self-adjoint) and are positive. The most specific case of interest is when there is uniform permeability μ and uniform permittivity ϵ in which case

$$L = \mu F \quad \text{and} \quad C = \epsilon F^{-1} \quad (1.9)$$

where F only depends on the geometry of the cables and is real symmetric, so Hermitian and positive definite.

1.1 Uniform Cables

In the case of uniform cables, we can write the solution of the transmission-line equations (1.1) using either hyperbolic or trigonometric functions. The solution of (1.1) is given by an exponential of the coefficient matrix found in (1.3):

$$\begin{bmatrix} V(t) \\ I(t) \end{bmatrix} = e^{-t \begin{bmatrix} 0 & Z \\ Y & 0 \end{bmatrix}} \begin{bmatrix} V(0) \\ I(0) \end{bmatrix}. \quad (1.10)$$

Now if we write the exponential as a power series and collect every other term into two groups, we obtain

$$e^{-t \begin{bmatrix} 0 & Z \\ Y & 0 \end{bmatrix}} = \begin{bmatrix} \cosh(t\sqrt{ZY}) & -Y^{-1}\sqrt{ZY} \sinh(t\sqrt{ZY}) \\ -Z^{-1}\sqrt{ZY} \sinh(t\sqrt{ZY}) & \cosh(t\sqrt{ZY}) \end{bmatrix}. \quad (1.11)$$

If we write $Y = \imath L$ and $Z = \imath C$, where L is the inductance matrix and C is the capacitance matrix, and both L and C are symmetric and thus Hermitian (self-adjoint), then

$$e^{-\imath t \begin{bmatrix} 0 & C \\ L & 0 \end{bmatrix}} = \begin{bmatrix} \cos(t\sqrt{CL}) & -\imath L^{-1}\sqrt{CL} \sin(t\sqrt{CL}) \\ -\imath C^{-1}\sqrt{CL} \sin(t\sqrt{CL}) & \cos(t\sqrt{CL}) \end{bmatrix}. \quad (1.12)$$

So, in this case, the solution is given by simple waves traveling down the line.

2 Symmetrization of the Transmission Line Equations

In some cases, the Equations (1.3) can be symmetrized by a change of dependent variables. To simplify, assume the material properties are constant and then consider

$$\frac{d}{dt} \begin{bmatrix} AV \\ BI \end{bmatrix} = - \begin{bmatrix} 0 & AZB^{-1} \\ BYA^{-1} & 0 \end{bmatrix} \begin{bmatrix} AV \\ BI \end{bmatrix}. \quad (2.13)$$

where the matrices A and B are to be chosen so that the matrix in the previous equation is symmetric, that is, so that

$$AZB^{-1} = BYA^{-1}, \quad (2.14)$$

or

$$Y = B^{-1}AZB^{-1}A. \quad (2.15)$$

Setting $M = B^{-1}A$, given Y and Z we must find M so that

$$Y = MZM. \quad (2.16)$$

This is a system of N^2 quadratic equations in N^2 unknowns, so it is not clear if there even exist complex solutions or not. However, if Y and Z commute then there is a solution:

$$[Y, Z] = YZ - ZY = 0 \Rightarrow M = \sqrt{Y} \sqrt{Z}^{-1} = \sqrt{Z}^{-1} \sqrt{Y}. \quad (2.17)$$

So in the case of commuting matrices, the simple choice of

$$A = \sqrt{Y}, \quad B = \sqrt{Z} \quad (2.18)$$

will make the system symmetric.

2.1 Variable Coefficients and Symmetry

We now assume that for each z , the matrices in the transmission line equations (1.1) commute:

$$[Y(t), Z(t)] = Y(t)Z(t) - Z(t)Y(t) = 0. \quad (2.19)$$

If we introduce the new variables

$$\tilde{V}(t) = A(t)V(t), \quad \tilde{I}(t) = B(t)I(t), \quad (2.20)$$

then a simple computation gives

$$\begin{aligned} \frac{d\tilde{V}(t)}{dt} &= \frac{dA(t)}{dt} A^{-1}(t) \tilde{V} - A(t) Z(t) B^{-1}(t) \tilde{I}(t) \\ \frac{d\tilde{I}(t)}{dt} &= \frac{dB(t)}{dt} B^{-1}(t) \tilde{I} - B(t) Y(t) A^{-1}(t) \tilde{V}(t) \end{aligned} \quad (2.21)$$

These equations can be written as a system

$$\frac{d}{dt} \begin{bmatrix} \tilde{V} \\ \tilde{I} \end{bmatrix} = \begin{bmatrix} A'(t) A^{-1}(t) & A(t) Z(t) B^{-1}(t) \\ B(t) Y(t) A^{-1}(t) & B'(t) B^{-1}(t) \end{bmatrix} \begin{bmatrix} \tilde{V} \\ \tilde{I} \end{bmatrix}. \quad (2.22)$$

The choice of

$$A(t) = \sqrt{Y(t)}, \quad B(t) = \sqrt{Z(t)} \quad (2.23)$$

makes the off-diagonal part of the system symmetric, and the diagonal parts are logarithmic derivatives.

2.2 Problems With Non-Commuting Matrices

Here we indicate why the dealing with matrix functions of t that do not commute is difficult. So, if a matrix function $M(t)$ has the property that the matrices for different values of t commute, that is,

$$[M(t_1), M(t_2)] = 0 \quad (2.24)$$

for all t_1 and t_2 , and $f(x)$ is any differentiable function, then

$$\frac{d}{dt}f(M(t)) = \frac{df}{dx}(M(t)) \frac{dM}{dt}(t), \quad (2.25)$$

that is, the chain rule works. Without the commuting condition, the chain rule does not work in general, as elementary examples will show.

There is one important exception for the function $1/x$. If we differentiate $M(t) M^{-1}(t) = \text{Identity}$, then we get

$$\frac{d}{dt}M^{-1}(t) = -M^{-1}(t) \left(\frac{d}{dt}M(t) \right) M^{-1}(t). \quad (2.26)$$

One important problem is that the derivative of a square root of a matrix cannot be found in closed form, but we can find a simple equation for the square root. To see this, we follow the calculus derivation of the derivative. We have that

$$M(t) = \sqrt{Y(t)} \Rightarrow M^2(t) = Y(t). \quad (2.27)$$

and then differentiation gives

$$M(t) \frac{dM(t)}{dt} + \frac{dM(t)}{dt} M(t) = Y'(t). \quad (2.28)$$

This doesn't lead to a simple formula for the derivative of the square root. It does give a $N \times N$ system of nonlinear equations to find the derivative of the square root, but again it is difficult to know when this system is solvable.

We would also like to have a simple form for the "logarithmic" derivatives

$$\frac{dA(t)}{dt} A^{-1}, \quad \frac{dB(t)}{dt} B^{-1} \quad (2.29)$$

that appear in the transformed equations. However, these are not the derivatives of $\ln(A(t))$ and $\ln(B(t))$ unless the commuting condition (2.24) holds. If we set

$$M(t) = \ln(A(t)), \quad (2.30)$$

then

$$e^{M(t)} = A(t). \quad (2.31)$$

This last expression can be differentiated using Formula 6.196 in [4], but this produces a formula difficult to solve for dM/dt .

2.3 Product Integrals and Logarithmic Derivatives

The theory of product integrals and logarithmic derivatives was invented to deal with just the situation described in the previous section. Using the definition of the product integral (see Section 5 of Baum and Steinberg [4] for definitions and basic properties) applied to the exponential of $M(t)$, we define

$$G(t) = \prod_0^t e^{ds M(s)}, \quad (2.32)$$

and then we get (see [4], Equation (5.155))

$$\frac{dG}{dt}(t) = M(t) G(t). \quad (2.33)$$

Also (see [4], Equation (5.158)) the logarithmic derivative is defined as

$$D_t G(t) = G'(t) G^{-1}(t), \quad (2.34)$$

so that

$$D_t G(t) = G'(t) G^{-1}(t) = M(t). \quad (2.35)$$

We also have that (see [4], Equation (5.160))

$$G(t) = \prod_0^t e^{D_s G(s) ds}. \quad (2.36)$$

One of the more interesting formulas for product integrals is the analog of the formula $\exp(a+b) = \exp(a)\exp(b)$ ((see [4], Equation (5.163)): if

$$G(t) = \prod_0^t e^{A(s) ds}, \quad (2.37)$$

then

$$\prod_0^t e^{(A(s)+B(s)) ds} = G(t) \prod_0^t e^{G^{-1}(s) B(s) G(s) ds}. \quad (2.38)$$

We will use this formula in the next section.

2.4 Product Integral Reduction of the Transmission Line Equations

Here we show that the sum rule (2.38) can be used to check that we have correctly transformed the transmission line equations or, conversely, that the sum rule is correct. We rewrite Equation (2.22) as

$$\frac{d}{dt} \begin{bmatrix} \tilde{V} \\ \tilde{I} \end{bmatrix} = \left(\begin{bmatrix} A' A^{-1} & 0 \\ 0 & B' B^{-1} \end{bmatrix} + \begin{bmatrix} 0 & A Z B^{-1} \\ B Y A^{-1} & 0 \end{bmatrix} \right) \begin{bmatrix} \tilde{V} \\ \tilde{I} \end{bmatrix}, \quad (2.39)$$

so and then apply the sum rule (2.38) with

$$\begin{aligned} A &\rightarrow \begin{bmatrix} A' A^{-1} & 0 \\ 0 & B' B^{-1} \end{bmatrix}, \\ B &\rightarrow \begin{bmatrix} 0 & A Z B^{-1} \\ B Y A^{-1} & 0 \end{bmatrix}, \end{aligned} \quad (2.40)$$

so that

$$\begin{aligned} G &\rightarrow \begin{bmatrix} A & 0 \\ 0 & B \end{bmatrix}, \\ G^{-1} B G &\rightarrow \begin{bmatrix} 0 & Z \\ Y & 0 \end{bmatrix}, \end{aligned} \quad (2.41)$$

and then

$$\prod_0^t e^{\begin{bmatrix} A'(s) A^{-1}(s) & A(s) Z(s) B^{-1}(s) \\ B(s) Y(s) A^{-1}(s) & B'(s) B^{-1}(s) \end{bmatrix} ds} = \begin{bmatrix} A(t) & 0 \\ 0 & B(t) \end{bmatrix} \prod_0^t e^{\begin{bmatrix} 0 & Z(s) \\ Y(s) & 0 \end{bmatrix} ds}, \quad (2.42)$$

which agrees with the definition (2.20) which we can write as

$$\begin{bmatrix} \tilde{V}(t) \\ \tilde{I}(t) \end{bmatrix} = \begin{bmatrix} A(t) & 0 \\ 0 & B(t) \end{bmatrix} \begin{bmatrix} V(t) \\ I(t) \end{bmatrix}. \quad (2.43)$$

3 Diagonalizing Symmetric Transmission Line Equations

In this section we assume the commuting property (2.19)

$$[Y(t), Z(t)] = Y(t) Z(t) - Z(t) Y(t) = 0. \quad (3.44)$$

and that one of the matrices $Y(t)$ or $Z(t)$ can be diagonalized. Then, because of the commuting property, both of the matrices can be diagonalized and have a complete common set of eigen-vectors $\phi_i(t)$ for all t . Define the S matrix to be the inverse of the matrix with columns the eigenvectors:

$$S(t) = [\phi_1(t), \dots, \phi_N(t)]^{-1}, \quad (3.45)$$

and then we have

$$\Lambda_Y(t) = S(t) Y(t) S^{-1}(t), \quad \Lambda_Z(t) = S(t) Z(t) S^{-1}(t), \quad (3.46)$$

where Λ_Y and Λ_Z are diagonal. If we now introduce the variables

$$\tilde{I}(t) = S(t)I(t), \quad \tilde{V}(t) = S(t)V(t), \quad (3.47)$$

then the transmission line equations can be written as in (2.22):

$$\frac{d}{dt} \begin{bmatrix} \tilde{V} \\ \tilde{I} \end{bmatrix} = \begin{bmatrix} S'(t)S^{-1}(t) & S(t)Z(t)S^{-1}(t) \\ S(t)Y(t)S^{-1}(t) & S'(t)S^{-1}(t) \end{bmatrix} \begin{bmatrix} \tilde{V} \\ \tilde{I} \end{bmatrix}. \quad (3.48)$$

The eigen-decomposition (3.46) then gives

$$\frac{d}{dt} \begin{bmatrix} \tilde{V} \\ \tilde{I} \end{bmatrix} = \begin{bmatrix} S'(t)S^{-1}(t) & \Lambda_Z(t) \\ \Lambda_Y(t) & S'(t)S^{-1}(t) \end{bmatrix} \begin{bmatrix} \tilde{V} \\ \tilde{I} \end{bmatrix}. \quad (3.49)$$

If the diagonal logarithmic derivative terms are zero, then the system is uncoupled:

$$\frac{d}{dt} \begin{bmatrix} \tilde{V} \\ \tilde{I} \end{bmatrix} = \begin{bmatrix} 0 & \Lambda_Z(t) \\ \Lambda_Y(t) & 0 \end{bmatrix} \begin{bmatrix} \tilde{V} \\ \tilde{I} \end{bmatrix}. \quad (3.50)$$

These terms will be zero if the eigenvectors are constant. If they are not zero, then the system doesn't uncouple and the standard solution techniques cannot be applied.

3.1 Circulant Matrices

Circulant matrices give an ideal situation in which to apply the diagonalization techniques because they have constant eigenvectors. Circulant matrices, which are constant along “diagonals”, are discussed in detail in Nitsch, Baum and Sturm [3] and Davis [2]. Here we adopt a definition in terms a basis which is convenient for Lie algebraic Computations. In particular, we will define circulant matrices in terms of the shift operation.

As shown in Figure 3.1, put N evenly distributed points labeled by $1, 2, \dots, N-1, N$ on the unit circle and then assigning the values $f = \{f_1, f_2, \dots, f_N\}$ to these points. The shift $S = S(N)$ in the clockwise direction moves the value at the point 1 to the point $N-1$, the value at the point 2 to the point 1 and so forth. So if $g = Sf$, then

$$\begin{aligned} g_1 &= (Sf)_1 = f_2, \\ g_2 &= (Sf)_2 = f_3, \\ &\vdots \\ g_N &= (Sf)_N = f_1. \end{aligned} \quad (3.51)$$

$$g_N = (Sf)_N = f_1. \quad (3.52)$$

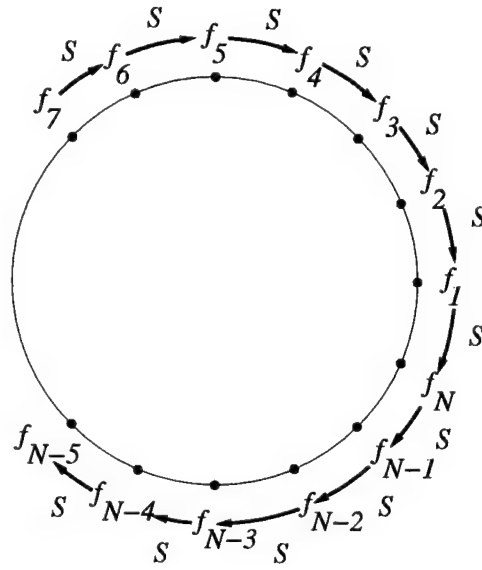


Figure 3.1: *Shift on a Circle*

This operation can be represented by a matrix:

$$\begin{bmatrix} g_1 \\ g_2 \\ \vdots \\ g_{N-1} \\ g_N \end{bmatrix} = \begin{bmatrix} 0 & 1 & 0 & 0 & \cdots & 0 & 0 \\ 0 & 0 & 1 & 0 & \cdots & 0 & 0 \\ & & & \vdots & & & \\ 0 & 0 & 0 & 0 & \cdots & 0 & 1 \\ 1 & 0 & 0 & 0 & \cdots & 0 & 0 \end{bmatrix} \begin{bmatrix} f_1 \\ f_2 \\ \vdots \\ f_{N-1} \\ f_N \end{bmatrix} \quad (3.53)$$

and so

$$S = S(N) = \begin{bmatrix} 0 & 1 & 0 & 0 & \cdots & 0 & 0 \\ 0 & 0 & 1 & 0 & \cdots & 0 & 0 \\ & & & \vdots & & & \\ 0 & 0 & 0 & 0 & \cdots & 0 & 1 \\ 1 & 0 & 0 & 0 & \cdots & 0 & 0 \end{bmatrix}. \quad (3.54)$$

This matrix plays a fundamental role in what follows.

By integer division we can represent any integer n as $n = qN + r$ where $0 \leq r < N$ and then the *mod* function is defined by $\text{mod}(n, N) = r$. So the matrix for the shift is given by

$$S_{i,j} = \begin{cases} 1 & \text{if } \text{mod}(i - j + 1, N) = 0 \\ 0 & \text{if } \text{mod}(i - j + 1, N) \neq 0 \end{cases} \quad (3.55)$$

In fact, we will define a family of shift operators $\text{Sh}(k) = \text{Sh}(k, N)$:

$$\text{Sh}(k)_{i,j} = \begin{cases} 1 & \text{if } \text{mod}(i - j + k, N) = 0 \\ 0 & \text{if } \text{mod}(i - j + k, N) \neq 0 \end{cases} \quad (3.56)$$

The geometric interpretation of $\text{Sh}(k)$ is that the values at the points on the unit circle are shifted clockwise k points if $k \geq 0$ and counter clockwise $-k$ points if $k \leq 0$. The matrices $\text{Sh}(k, N)$ are distinct for $0 \leq k < N$ and $\text{Sh}(k + mN, N) = \text{Sh}(k, N)$ for all m . Also $\text{Sh}(0, N)$ is the identity matrix and $\text{Sh}(1, N) = \text{Sh}(1) = S(N) = S$.

For $N = 5$ the distinct shift operators are:

$$\text{Sh}(0) = \begin{bmatrix} 1 & 0 & 0 & 0 & 0 \\ 0 & 1 & 0 & 0 & 0 \\ 0 & 0 & 1 & 0 & 0 \\ 0 & 0 & 0 & 1 & 0 \\ 0 & 0 & 0 & 0 & 1 \end{bmatrix}, \quad \text{Sh}(1) = \begin{bmatrix} 0 & 1 & 0 & 0 & 0 \\ 0 & 0 & 1 & 0 & 0 \\ 0 & 0 & 0 & 1 & 0 \\ 0 & 0 & 0 & 0 & 1 \\ 1 & 0 & 0 & 0 & 0 \end{bmatrix}, \quad (3.57)$$

$$\text{Sh}(2) = \begin{bmatrix} 0 & 0 & 1 & 0 & 0 \\ 0 & 0 & 0 & 1 & 0 \\ 0 & 0 & 0 & 0 & 1 \\ 1 & 0 & 0 & 0 & 0 \\ 0 & 1 & 0 & 0 & 0 \end{bmatrix}, \quad \text{Sh}(3) = \begin{bmatrix} 0 & 0 & 0 & 1 & 0 \\ 0 & 0 & 0 & 0 & 1 \\ 1 & 0 & 0 & 0 & 0 \\ 0 & 1 & 0 & 0 & 0 \\ 0 & 0 & 1 & 0 & 0 \end{bmatrix}, \quad (3.58)$$

$$\text{Sh}(4) = \begin{bmatrix} 0 & 0 & 0 & 0 & 1 \\ 1 & 0 & 0 & 0 & 0 \\ 0 & 1 & 0 & 0 & 0 \\ 0 & 0 & 1 & 0 & 0 \\ 0 & 0 & 0 & 1 & 0 \end{bmatrix}. \quad (3.59)$$

From the geometric interpretation of the shift operator, it is clear that

$$\text{Sh}(k_1, N) \text{Sh}(k_2, N) = \text{Sh}(k_1 + k_2, N). \quad (3.60)$$

An algebraic proof of this requires only a little work with the mod function. This immediately implies that

$$\text{Sh}(k, N) = S^k(N), \quad (3.61)$$

for all integers k .

A *circulant* matrix is a matrix that can be written as a linear combination of shift matrices:

$$\text{Ci}(c_0, c_1, \dots, c_{N-1}) = \sum_{k=0}^{N-1} c_k S^k. \quad (3.62)$$

Such matrices are constant on along the "diagonals". It is show in [2] that other common definitions of circulant are equivalent to this definition. In any case, all five dimensional circulant matrices are given by

$$\text{Ci}(c_0, c_1, c_2, c_3, c_4) = c_0 \text{Sh}(0) + c_1 \text{Sh}(1) + c_2 \text{Sh}(2) + c_3 \text{Sh}(3) + c_4 \text{Sh}(4) \quad (3.63)$$

$$= \begin{bmatrix} c_0 & c_1 & c_2 & c_3 & c_4 \\ c_4 & c_0 & c_1 & c_2 & c_3 \\ c_3 & c_4 & c_0 & c_1 & c_2 \\ c_2 & c_3 & c_4 & c_0 & c_1 \\ c_1 & c_2 & c_3 & c_4 & c_0 \end{bmatrix}. \quad (3.64)$$

3.2 Diagonalizing Circulant Matrices

Because circulant matrices can be written as a polynomial in the shift S (3.62), they all commute under multiplication and consequently can be diagonalized simultaneously. If fact, if we find a basis that diagonalizes S , then the same basis diagonalizes all powers of S , and consequently all circulant matrices. It is well known that the discrete Fourier transform diagonalizes all translation invariant operators, that is, all operators the commute with the translation S , so lets look at the discrete Fourier transform.

Let ω be a *primitive* N -th root of unity. Typically we take

$$\omega = e^{\pm \frac{2\pi i}{N}}, \quad (3.65)$$

but for many computations it is only important that $\omega \neq 1$. Then we have that

$$0 = \omega^N - 1 = (\omega - 1) \sum_{k=0}^{N-1} \omega^k, \quad (3.66)$$

which gives us the important identity

$$\sum_{k=0}^{N-1} \omega^k = 0. \quad (3.67)$$

In general, we need to know which factors of $\omega^N - 1$ the primitive N -th root satisfies. We take the Fourier, or more precisely the discrete Fourier transform matrix to be

$$F_{i,j} = F_{i,j}(N) = \frac{1}{\sqrt{N}} \omega^{-(i-1)(j-1)}, \quad 1 \leq i \leq N, 1 \leq j \leq N. \quad (3.68)$$

Note that the adjoint F^* of F is given by

$$F_{i,j}^* = F^*(N)_{i,j} = \frac{1}{\sqrt{N}} \omega^{+(i-1)(j-1)}. \quad (3.69)$$

There are many choices possible for the discrete Fourier transform matrix. Our choice gives

$$F^* S F = \text{diag}(1, w^{-1}, w^{-2}, w^{-3}, \dots, w^{1-N}), \quad (3.70)$$

that is, the k -th column of F is an eigenvector of S with eigenvalue ω^{1-k} . Additionally, F is a unitary matrix.

When we solve the transmission-line equations using Lie techniques, a critical ingredient is the exponential of each basis element. For circulant matrices, a basis is S^k , $0 \leq k \leq N$. We have diagonalized S , so

$$F^* S^k F = \text{diag}(1, w^{-k}, w^{-2k}, w^{-3k}, \dots, w^{(1-N)k}), \quad (3.71)$$

and then we see that

$$e^{t S^k} = F \text{diag}(1, e^{t w^{-k}}, e^{t w^{-2k}}, e^{t w^{-3k}}, \dots, e^{t w^{(1-N)k}}) F^*. \quad (3.72)$$

To apply this to the transmission-line equations (1.3),

$$\frac{d}{dt} \begin{bmatrix} V \\ I \end{bmatrix} = - \begin{bmatrix} 0 & Z \\ Y & 0 \end{bmatrix} \begin{bmatrix} V \\ I \end{bmatrix}, \quad (3.73)$$

we need to write Z and Y in terms of S :

$$Z(t) = \sum_{k=0}^{N-1} b_k(t) S^k, \quad Y(t) = \sum_{k=0}^{N-1} a_k(t) S^k. \quad (3.74)$$

In this case the system of equations can be rewritten as

$$\frac{d}{dt} \begin{bmatrix} V \\ I \end{bmatrix} = \sum_{i,j=0}^{N-1} -a_i(t) b_j(t) \begin{bmatrix} 0 & S^j \\ S^i & 0 \end{bmatrix} \begin{bmatrix} V \\ I \end{bmatrix}, \quad (3.75)$$

so we only need to know how to exponentiate the matrices

$$\begin{bmatrix} 0 & S^j \\ S^i & 0 \end{bmatrix}, \quad 0 \leq i, j \leq N-1. \quad (3.76)$$

However,

$$\begin{bmatrix} F^* & 0 \\ 0 & F^* \end{bmatrix} \begin{bmatrix} 0 & S^j \\ S^i & 0 \end{bmatrix} \begin{bmatrix} F & 0 \\ 0 & F \end{bmatrix} = \begin{bmatrix} 0 & (F^* S F)^j \\ (F^* S F)^i & 0 \end{bmatrix}, \quad (3.77)$$

which gives a “skew diagonalization” of the matrix involved in the exponential.

For the “skew-diagonal” types of matrices involved in the transmission-line equations, the xxx

Lemma:

4 Conclusions

References

- [1] by C.E. Baum, T.K. Liu, and F.M. Tesche, *On the analysis of General Multiconductor Transmission-Line Networks* Interaction Notes 350, 1978, Air Force Research Library.
- [2] P.J. Davis, *Circulant Matrices*, John Wiley and Sons, Inc., New York, 1979.
- [3] by J. Nitsch, C.E. Baum and R. Sturm, *The Treatment of Commuting Nonuniform Tubes in Multiconductor-Transmission-Line Theory* Interaction Notes 481, 1990, Air Force Research Library.
- [4] C.E. Baum and S. Steinberg, *Lie-Algebraic Representations of Product Integrals of Variable Matrices*, Mathematics Notes 92, DEHP, Air Force Laboratory, Kirtland Air Force Base, Albuquerque NM 87117.

APPROXIMATION OF THE SPACE-CHARGE LIMITED CURRENT OF RELATIVISTIC
ELECTRON BEAMS IN COAXIAL DRIFT TUBES

Kenny F. Stephens II
Doctoral Candidate
Department of Physics

University of North Texas
Denton, TX 76203

Final Report for:
Summer Research Extension Program
Phillips Laboratory

Sponsored by:
Air Force Office of Scientific Research
Bolling Air Force Base, Washington DC
and
University of North Texas
Denton, TX

December 1999

APPROXIMATION OF THE SPACE-CHARGE LIMITED CURRENT OF RELATIVISTIC ELECTRON BEAMS IN COAXIAL DRIFT TUBES

Kenny F. Stephens II
Doctoral Candidate
Department of Physics
University of North Texas

Abstract

A two-dimensional theory for predicting the space-charge limited current of relativistic electron beams in coaxial drift tubes is presented. Applicable to annular beams or arbitrary radius and thickness, the theory considers not only the effect of the inner conductor but also takes into account finite-length effects. Using Green's second identity, Poisson's equation for the space-charge limited problem is reduced to solving a Sturm-Liouville eigenvalue problem. For some limiting cases, closed-form analytical solutions are available.

APPROXIMATION OF THE SPACE-CHARGE LIMITED CURRENT OF RELATIVISTIC ELECTRON BEAMS IN COAXIAL DRIFT TUBES

Kenny F. Stephens II

I Introduction

One limitation to the production of high-power microwaves (HPM) is the ability of the HPM device to carry an electron beam of sufficient current. It is well known that the space-charge of the beam places an upper-limit on the amount of current than can be carried. As the beam current approaches this limit, the amount of current actually propagated through the device no longer increases. Eventually, only a fraction of the input current travels through the device regardless of the amount of input current. Because this phenomena depends on the space-charge of the beam, this limiting value is called the space-charge limited (SCL) current. Thus, the ability to predict the SCL current is important in a variety of intense electron beam applications, including HPM devices.

Precisely solving the SCL problem requires the solution of a highly nonlinear Poisson equation. To date, only one-dimensional solutions are available in closed, analytic form. Because of these limited solutions, the researcher cannot consider both radial and axial effects simultaneously without resorting to numerical solution or computer simulations. For this reason, attempts to estimate the SCL current are important. Perhaps the simplest approach is the "infinite-length" approximation. Under this approximation, the beam is considered to travel in a smooth-bore bore under the influence of an infinitely strong axial magnetic field that prevents radial and azimuthal motions. Furthermore, all physical quantities are considered independent of the axial coordinate so that only radial variations in the electric potential need be considered. This approach is adequate for situations where the beam length is several times the tube radius.

In Ref. [1], a two-dimensional theory is presented. Assuming the beam travels in a strong axial magnetic field so that radial and azimuthal motions need not be considered, the theory presents

a method to estimate an upper-bound on the SCL current. Applicable only to beams that completely fill a hollow drift tube, the theory was later extended to annular beams of arbitrary radius and thickness in Ref. [2]. Since the use of coaxial drift tubes has recently been shown to enhance the SCL current (see Ref. [3]), the present work extends the theory to consider the finite-length effects of relativistic electron beams in coaxial drift tubes.

II Theory Review

The problem geometry consists of two coaxial, cylindrical conductors of length L . The inner conductor has radius r_1 and the outer conductor radius r_2 . The annular electron beam, of inner radius r_i , outer radius r_o and current I_0 , is emitted from a foil at $z = 0$ with uniform density and passes to a completely absorbing collector plate at $z = L$. A strong, axial magnetic field is externally applied to prevent any radial or azimuthal motion. Letting the beam be injected with a kinetic energy $[\gamma_0 - 1]mc^2$, the kinetic energy at any location within the drift tube, $[\gamma(r, z) - 1]mc^2$, can be written in terms of the injected kinetic energy and the electrostatic potential, $\phi(r, z)$, through conservation of energy:

$$\gamma(r, z) = \gamma_0 + \frac{e}{mc^2} \phi(r, z). \quad (1)$$

Due to the external magnetic field, the relativistic mass factor is simply related to the axial velocity according to

$$\gamma(r, z) = \frac{1}{\sqrt{1 - \beta^2}}, \quad (2)$$

where $\beta c \approx v_z$ is the axial velocity. Since only axial motion is considered, the current density is simply $J = J_z = -en_0\beta c$, where n_0 is the beam density. Through conservation of charge, the charge density must be constant. Using Eqs. (1) and (2), Poisson equations, $\nabla^2\phi(r, z) = 4\pi en_0$, can be written

$$\nabla^2\Phi(r, z) = \frac{1}{r} \frac{\partial}{\partial r} r \frac{\partial\Phi(r, z)}{\partial r} + \frac{\partial^2\Phi(r, z)}{\partial z^2} = \begin{cases} \frac{K}{\beta(r, z)}, & r_i \leq r \leq r_o, 0 \leq z \leq L, \\ 0, & \text{otherwise,} \end{cases} \quad (3)$$

subject to the boundary conditions

$$\begin{aligned}\Phi(r, 0) = \Phi(r, L) &= 0, & r_1 \leq r \leq r_2 \\ \Phi(r_1, z) = \Phi(r_2, z) &= 0, & 0 \leq z \leq L.\end{aligned}\tag{4}$$

Here, $\Phi = e\phi/mc^2$ is the normalized potential energy and $K = 4i_0/(r_o^2 - r_i^2)$ with $i_0 = I_0/I_A$ the injected current normalized to the Alfvén current, $I_A = mc^3/e$. The velocity factor in Poisson's equation is written in terms of the potential according to

$$\beta(r, z) = \sqrt{1 - \gamma^{-2}(r, z)} = \frac{\sqrt{1 - [\gamma_0 + \Phi(r, z)]^2}}{\gamma_0 + \Phi(r, z)}.\tag{5}$$

Equation (3) is the nonlinear system whose solution is desired. Although an exact solution is unavailable, the next section reviews the method developed in Ref. [1] which will yield an upper-bound on the SCL current.

III Upper Bound for the SCL Current

To make progress toward an approximate solution of Eq. (3), Green's second identity is applied to the beam volume:

$$\underbrace{\int_V [\psi \nabla^2 \Phi - \Phi \nabla^2 \psi] dv}_\tau = \underbrace{\oint_S \left[\psi \frac{\partial \Phi}{\partial n} - \Phi \frac{\partial \psi}{\partial n} \right] ds}_\Sigma.\tag{6}$$

The underbraces indicate that τ represents the volume integral and Σ the surface integral. In Eq. (6), Φ is the electrostatic potential defined in Eqs. (3) and (4) while ψ is a solution to the eigenvalue problem defined by

$$\nabla^2 \psi(r, z) = \frac{1}{r} \frac{\partial}{\partial r} r \frac{\partial \psi(r, z)}{\partial r} + \frac{\partial^2 \psi(r, z)}{\partial z^2} = \Lambda \psi(r, z), \quad r_i \leq r \leq r_o, 0 \leq z \leq L,\tag{7}$$

$$\begin{aligned}\psi(r, 0) = \psi(r, L) &= 0, & r_i \leq r \leq r_o, \\ a_1 r_i \frac{\partial \psi(r, z)}{\partial r} \Big|_{r=r_i} - a_2 \psi(r_i, z) &= 0, & 0 \leq z \leq L, \\ b_1 r_o \frac{\partial \psi(r, z)}{\partial r} \Big|_{r=r_o} - b_2 \psi(r_o, z) &= 0, & 0 \leq z \leq L.\end{aligned}\tag{8}$$

The constants a and b are determined in Sect. IV such that 1) the surface integral Σ in Eq. (6) is zero, 2) Eq. (7) has an eigenfunction that is nonzero within the problem domain, and 3) the corresponding eigenvalue is negative. Assuming these conditions are satisfied, the volume integral in Eq. (6) must also be zero and can be written as

$$\tau = 2\pi \int_0^L \int_{r_i}^{r_o} \left[\frac{K}{\beta(r, z)} - \Lambda_0 \Phi(r, z) \right] \psi_0(r, z) r dr dz = 0, \quad (9)$$

where Λ_0 is the fundamental eigenvalue corresponding to the eigenfunction $\psi_0(r, z)$ that is zero only on the volume surface. Since ψ_0 does not change sign within the integration volume, the bracketed term in Eq. (9) must change sign. Let the point at which this occurs be (r', z') . Thus,

$$K = |\Lambda_0| \beta(r', z') \Phi(r', z'). \quad (10)$$

If the derivative of K with respect to $\gamma(r', z')$ is set equal to zero and solved for $\gamma(r', z')$, it is found that $\beta(r', z') \Phi(r', z')$ is maximal when $\gamma(r', z') = (\gamma_0^{2/3} - 1)^{3/2}$. Since $1 < \gamma(r', z') < \gamma_0$, this implies that K has the upper bound

$$K \leq |\Lambda_0| \left(\gamma_0^{2/3} - 1 \right)^{3/2}. \quad (11)$$

Therefore, Eqs. (10) and (11) define the upper bound for the SCL current as

$$i_0 \leq i_{ub} \equiv \frac{r_o^2 - r_i^2}{4} |\Lambda_0| \left(\gamma_0^{2/3} - 1 \right)^{3/2}. \quad (12)$$

Thus, the problem of determining an expression for the SCL current for a specified beam and drift tube geometries is reduced from solving a nonlinear partial differential equation to solving a two-dimensional Sturm-Liouville eigenvalue problem. The general solution of this problem is developed in the following section.

IV General Solution of the Eigenvalue Problem

An upper bound for the SCL current was obtained in Sect. III based on the assumption that the surface integral in Eq. (6) is zero. This section solves the eigenvalue problem defined by Eqs. (7) and (9) such that the surface integral is indeed zero. This is achieved by determining the

coefficients a_1 , a_2 , b_1 and b_2 . By separation of variables, the desired eigenfunction can be written as

$$\psi(r, z) = \rho(r) \sin(\kappa_1 z), \quad (13)$$

where $\kappa_n = n\pi/L$. This form automatically satisfies the axial boundary conditions. Substituting Eq. (13) into Σ yields

$$\Sigma = 2\pi\xi \int_0^L \left[\rho(\xi) \frac{\partial \phi(r, z)}{\partial r} \Big|_{r=\xi} - \phi(\xi, z) \frac{\partial \rho(r)}{\partial r} \Big|_{r=\xi} \right] \sin(\kappa_1 z) dz \Big|_{\xi=r_i}^{r_o}. \quad (14)$$

The solution to Eq. (3) in the charge-free regions as

$$\begin{aligned} \phi(r, z) &= \sum_{n=1}^{\infty} A_n g_n(r, r_1) \sin(\kappa_n z), \quad r_1 \leq r \leq r_i, \\ \phi(r, z) &= \sum_{n=1}^{\infty} B_n g_n(r, r_2) \sin(\kappa_n z), \quad r_o \leq r \leq r_2, \end{aligned} \quad (15)$$

where

$$g_n(r, r') = I_0(\kappa_n r) - \frac{I_0(\kappa_n r')}{K_0(\kappa_n r')} K_0(\kappa_n r). \quad (16)$$

I_0 and K_0 are the modified Bessel functions of the first and second kind, respectively. The form of the function $g_n(r, r')$ is chosen to satisfy the radial boundary conditions and to reduce to the proper form for hollow tubes, $r_1 = 0$.

If Eq. (15) is substituted into Eq. (14), it is found that the surface integral does vanish is ψ non-trivially solves the eigenvalue problem

$$\frac{d}{dr} \left[r \frac{d\rho(r)}{dr} \right] + \lambda r \rho(r) = 0, \quad r_i \leq r \leq r_o, \quad (17)$$

$$a_1 r_i \rho'(r_i) - a_2 \rho(r_i) = 0, \quad (18)$$

$$b_1 r_o \rho'(r_o) - b_2 \rho(r_o) = 0.$$

where the coefficients in the boundary conditions are given by

$$\begin{aligned} a_1 &= g_1(r_i, r_1) & b_1 &= g_1(r_o, r_2) \\ a_2 &= r_i \frac{dg_1(r, r_1)}{dr} \Big|_{r=r_i} & b_2 &= r_o \frac{dg_1(r, r_2)}{dr} \Big|_{r=r_o} \end{aligned} \quad (19)$$

Noting that the differential equation for $\rho(r)$ is Bessel's equation, the solution to Eq. (17) can be written

$$\rho(r) = J_0(kr) + CN_0(kr), \quad (20)$$

where $\lambda_0 = k^2$ and $J_0 (N_0)$ is the zeroth order Bessel functions of the first (second) kind. To determine the coefficient C and eigenvalue k , the following system of equations must be solved:

$$\begin{aligned} a_2 [J_0 (kr_i) + CN_0 (kr_i)] + a_1 kr_i [J_1 (kr_i) + CN_1 (kr_i)] &= 0, \\ b_2 [J_0 (kr_o) + CN_0 (kr_o)] + b_1 kr_o [J_1 (kr_o) + CN_1 (kr_o)] &= 0. \end{aligned} \quad (21)$$

In some cases it is not necessary to determine the value of C so that only the equation

$$\frac{a_2 J_0 (kr_i) + a_1 kr_i J_1 (kr_i)}{a_2 N_0 (kr_i) + a_1 kr_i N_1 (kr_i)} = \frac{b_2 J_0 (kr_o) + b_1 kr_o J_1 (kr_o)}{b_2 N_0 (kr_o) + b_1 kr_o N_1 (kr_o)}, \quad (22)$$

need be solved for k .

Having now solved the eigenvalue problem defined in Sect. III, the upper bound for the SCL current can be written directly in terms of the eigenvalue k as

$$i_{UB} = \frac{r_o^2 - r_i^2}{4} [k^2 + \kappa_1^2] (\gamma_0^{2/3} - 1)^{3/2}. \quad (23)$$

To estimate the SCL current for an annular electron beam travelling through a coaxial drift tube, the value of k must be determined from Eq. (22) and inserted into Eq. (23). The next section presents some closed-form analytical expressions for the upper bound under certain limiting cases.

V Coaxial drift tubes

Having developed an expression for the SCL current upper bound in terms of the eigenvalue problem discussed in Sect. IV, the determinantal equation for the eigenvalue is now solved for cases which yield closed analytic expressions. This section determines the SCL current for annular beams in coaxial tubes. For cases of hollow tubes, the reader is referred to Ref. [2].

V.1 Thin annular beam

The first case is a thin annular beam, i.e., a beam with zero thickness. Letting the beam thickness be $\delta = r_o - r_i$, the inner beam radius is replaced with $r_i \rightarrow (1 - \delta)r_o$ in the boundary condition

coefficients a_1 and a_2 . These coefficients are then replaced with their first-order Taylor series, i.e.,

$$\begin{aligned} a_1 &\approx g_1(r_o, r_1) - \kappa_1 r_o \delta g_1'(r_o, r_1), \\ a_2 &\approx \kappa_1 r_o [g_1'(r_o, r_1) - \kappa_1 r_o \delta g_1(r_o, r_1)], \end{aligned} \quad (24)$$

where

$$g_1'(r_o, r_1) = \left. \frac{\partial g_1(r, r_1)}{\partial r} \right|_{r=r_o}. \quad (25)$$

Next, the circular Bessel functions in Eq. (22) are replaced by the leading term of their respective asymptotic expansions, yielding

$$\cot(k\delta) = -\frac{a_2 b_2 + a_1 b_1 k^2 r_o^2 (1 - \delta)}{a_1 b_2 k (1 - \delta) r_o - a_2 b_1 k r_o}. \quad (26)$$

Considering only the right-hand side, replaced a_1 and a_2 Using Eq. (24, the right-hand side can be re-written as

$$\cot(k\delta) = -\frac{b_1 r_o [I_0(\kappa_1 r_o) - K_0(\kappa_1 r_o)]}{b_1 \kappa_1^2 r_o [I_1(\kappa_1 r_o) + K_1(\kappa_1 r_o)] b_2 [I_0(\kappa_1 r_o) + K_0(\kappa_1 r_o)]}, \quad (27)$$

where the limit $\delta \rightarrow 0$ was taken and only the leading term was retained. Expanding b_1 and b_2 , the modified Bessel function Wronskian

$$I_1(z) K_0(z) + I_0(z) K_1(z) = \frac{1}{z} \quad (28)$$

allows the determinantal equation to be written

$$\cot(k\delta) = \left[-\frac{r_o}{\delta} \frac{g_1(r_o, r_1) g_1(r_o, r_2)}{g_1(r_1, r_2)} K_0(\kappa_1 r_1) \right] (k\delta). \quad (29)$$

To simply further, note that the right-hand side is a linear function of $(k\delta)$ whose slope increases without bound as δ approaches zero. Thus, equality will hold only if $k\delta \ll 1$. Using the small argument expansion of the cotangent, $\cot(z) \sim 1/z$, gives

$$k^2 \delta r_o \sim \frac{g_1(r_1, r_2)}{g_1(r_o, r_1) g_1(r_o, r_2) K_0(\kappa_1 r_1)}. \quad (30)$$

Having obtained a closed expression for k^2 , the upper bound SCL current can now be determined. If the beam area is re-written as

$$\pi(r_o^2 - r_i^2) = \pi(r_o - r_i)(r_o + r_i) = 2\delta r_o, \quad (31)$$

the geometric factor is

$$\frac{g_1(r_1, r_2)}{g_1(r_o, r_1) g_1(r_o, r_2) K_0(\kappa_1 r_1)} \quad (32)$$

and the SCL current estimate is

$$i_{UB} = \frac{g_1(r_1, r_2)}{g_1(r_b, r_1) g_1(r_b, r_2) K_0(\kappa_1 r_1)} \left(\gamma_0^{2/3} - 1 \right)^{3/2}. \quad (33)$$

V.2 Thin annular beam, long drift tube

The result in Eq. (33) is now shown to agree with the infinite-length approximation. To this end, the beam is further assumed to be long. This implies that the beam length is larger than any radial dimension, i.e., $r_2 \ll L$. With the small argument expansion of the modified Bessel functions,

$$\begin{aligned} I_0(z) &\sim 1, \\ K_0(z) &\sim -\ln(z), \end{aligned} \quad (34)$$

the geometric factor, Eq. (32), becomes

$$\frac{\ln\left(\frac{r_1}{r_2}\right)}{2 \ln\left(\frac{r_2}{r_o}\right) \ln\left(\frac{r_o}{r_2}\right)}. \quad (35)$$

Therefore, the SCL current estimate for a thin annular beam in a long drift tube is

$$i_{UB} = \frac{\ln\left(\frac{r_1}{r_2}\right)}{2 \ln\left(\frac{r_2}{r_o}\right) \ln\left(\frac{r_o}{r_2}\right)} \left(\gamma_0^{2/3} - 1 \right)^{3/2}, \quad (36)$$

a result that perfectly agrees with the infinite-length approximation (see Ref. [3]). The finite-length effects are shown in Fig. 1 which compares Eqs. (32) and (35).

V.3 Full annular beam

The final limiting case is a full annular beam, i.e., a beam completely filling the drift tube. Under such circumstances, $r_i = r_1$ and $r_o = r_2$. Thus, the boundary condition coefficients a_1 and b_1 are zero. Equation (21) becomes

$$J_0(kr_1) N_0(kr_2) - J_0(kr_2) N_0(kr_1) = 0. \quad (37)$$

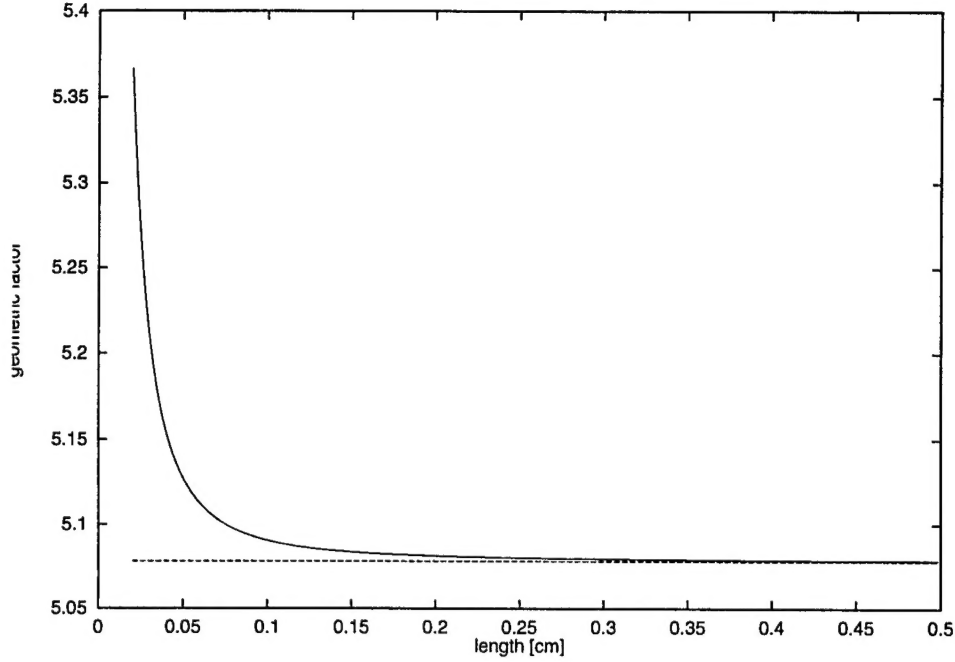


Figure 1: Comparison of the SCL current for a thin annular electron beam travelling in a coaxial drift tube with finite-length effects and without. The outer conductor radius is 0.01 cm.

This is a cross-product of circular Bessel functions and the solution k can be approximated (See Eqs. [9.5.27]-[9.5.29] of Ref. [4]) by

$$k \approx \frac{\pi}{r_2 - r_1} - \frac{r_2 - r_1}{8\pi r_1 r_2}. \quad (38)$$

Using this in Eq. (12), the SCL current upper bound for a full annular beam is

$$i_{UB} = \frac{r_2^2 - r_1^2}{4} \left\{ \left[\frac{\pi}{r_2 - r_1} - \frac{r_2 - r_1}{8\pi r_1 r_2} \right]^2 + \left[\frac{\pi}{L} \right]^2 \right\} (\gamma_0^{2/3} - 1)^{3/2}. \quad (39)$$

VI Concluding Remarks

A theory to estimate the SCL current, including finite-length effects, for uniform, relativistic electron beams propagating in circular drift tubes has been extended to include annular drift tubes and beams of arbitrary radius and thickness. For limiting beam and tube geometries, closed-form expressions for the SCL current are available. For other cases, a numerical solution must be used.

The theory assumes a strong external magnetic field to prevent radial and aximuthal motion of the beam particles. Using a beam of uniform density, the theory is not self-consistent. Furthermore, the method can be applied only to those cases where the drift tube walls are grounded. It has recently been shown that biasing the inner conductor can enhance the SCL current, see Ref. [3]. Methods to extend the present theory to such cases is underway.

References

- [1] V. S. Voronin, Yu. T. Zozulaya, and A. N. Lebedev, *Soviet Phys. Tech. Phys.*, **17**, p. 432 (1972).
- [2] T. C. Genoni and W. A. Proctor, *J. Plasma Phys.*, **23**, p. 129 (1980).
- [3] H. S. Uhm, *Phys. Plasmas*, **6**, p. 1360, (1999).
- [4] M. Abramowitz and I. A. Stegun, editors, *Handbook of Mathetmatical Functions*, National Bureau of Standards, Washington, D.C., p. 374 (1964).